

## Chapter 20

# Two-Phase Flow and Flow Boiling in Microchannels

**Summary:** An overview of the state-of-the-art of two-phase macro-to-microscale transition criteria, critical heat flux, two-phase flow patterns and maps, void fractions and bubble dynamics, flow boiling heat transfer and two-phase pressure drops in microchannels is described here. This chapter addresses both experimental studies and prediction methods for microchannels, together with some comparisons of these methods to experimental databases and to one another. For the benefit of the reader who has a special interest in two-phase microscale flows and heat transfer and because of the unique nature of microscale two-phase flow prediction methods compared to macroscale methods, the entire overview of microscale two-phase flow and boiling heat transfer is presented here in one chapter rather than disseminating each to its respective chapter elsewhere in this book. However, condensation in microchannels is *not* addressed here.

## 20.1 Introduction

Before beginning, it is worth noting that what happens in microchannels in two-phase flows can be quite different from single-phase flows in microchannels. While initial studies in the literature reported significant size effects on friction factors and heat transfer coefficients in very small channels in single-phase flows, more accurate recent tests and analysis done with very smooth internal channels have shown that macroscale methods for single-phase flows work well down to at least diameters of 5-10 microns and hence channels larger than this size can still be considered to be macroscale. This is *not* the case for macroscale two-phase flow methods, which usually do *not* work very well at all when compared to data for channels below about **3 mm diameter**. Thus, it is very risky to extrapolate macroscale two-phase flow pattern maps, flow boiling heat transfer methods and two-phase pressure drop models to microchannels, except for specific documented cases. Furthermore, many of the controlling phenomena and mechanisms change when passing from macrochannel two-phase flow and heat transfer to microchannels. For example, surface tension (capillary) forces become much stronger as the channel size diminishes while gravitational forces are weakened. Therefore, it is usually not sensible to empirically refit macroscale methods to microscale data since the underlying physics have substantially changed. This means that new dimensionless groups have come into play while the influence of others has disappeared.

### 20.1.1 Objectives of this chapter

A concise summary of research on two-phase flow and flow boiling in microchannels is presented here. It is not the objective here to describe *all* the work that has been published on this topic, but instead to present a compact treatment of some typical results, prediction methods and an assessment of where we stand today on the most important topics. The present chapter addresses microscale topics in the following order: (i) the dilemma of the macro-to-microscale transition in two-phase flow and heat transfer, and how this issue has been addressed so far, (ii) critical heat flux and hot spot analysis, (iii) two-phase flow observations, regime-transition theories and flow pattern maps, (iv) void fraction and bubble dynamics, (v) flow boiling heat transfer mechanisms and results, flow boiling prediction methods and some comparisons and (vi) two-phase pressure drop results, prediction methods and their comparisons.

For those interested, other general reviews covering microchannel heat transfer for single-phase and two-phase flows are available by Mehendale and Jacobi (2000), Kandlikar (2001), Huo et al. (2001), Kandlikar and Grande (2003), Bergles et al. (2003), Thome, Groll and Mertz (2003), Cheng and Mewes (2006), and Cheng, Ribatski and Thome (2008), just to name a few. Cheng and Wu (2006) presented a

detailed chapter on microscale heat transfer and its use in heat pipes in *Advances in Heat Transfer*. To further indicate the rapidly growing interest in microscale heat transfer, there is now an entire book dedicated specifically to microscale flow and heat transfer by Kandlikar and Garimella (2005). There are numerous conferences covering specifically this topic: so far three ECI Microscale conferences by Celata (see Celata (2004) for example), and the ASME International Conference on Microchannels and Minichannels organized annually by Kandlikar. Keynote lectures by the present author have been given at the 5<sup>th</sup> International Boiling Conference [Thome (2003)], the 13<sup>th</sup> International Heat Transfer Conference in Sydney [Thome (2006)] and at the ASME IMECE conference in Seattle [Thome et al. (2007)]. Furthermore, a popular one-week international shortcourse is now available on single- and two-phase flows and heat transfer in microchannels, updated and organized annually in Lausanne by Thome each June.

Notably, *condensation in microchannels* is *not* addressed in this chapter; the reader is referred to the chapter of Garimella in Kandlikar and Garimella (2005) for an extensive review of macroscale and microscale condensation and other reviews and papers, such those by Cavallini et al. (2006) and Wang and Rose (2005). Furthermore, *single-phase heat transfer in microchannels* is also *not* treated in this chapter and the interested reader is referred again to the Kandlikar and Garimella (2005) book and other reviews and studies on this topic, such as those of Morini (2004), Hetsroni et al. (2005) and Celata et al. (2006).

### 20.1.2 Applications of microscale flow boiling

Numerous applications for microscale flow boiling are emerging: high heat flux cooling of computer microprocessor chips and power electronics, precise cooling of micro-reactors, rapid and uniform cooling of LED displays, development of automotive evaporators with multi-port aluminum tubes, etc. All of these applications require thermal design methods that are accurate, reliable and robust (that is, methods that follow the trends of the data well and work for a multitude of fluids, channel sizes and shapes, pressures, flow rates, heat fluxes, etc.). Presently, the state-of-the-art is only partially able to fulfill such requirements.

For the design and fabrication of micro-evaporators using microscale flow boiling for transferring heat, Wolverine Tube Inc. has developed a new patented technique called **Micro Deformation Technology** (MDT). Figure 20.1 shows an example of such fin geometries. The process can produce fin densities up to as high as about 1000 fins per inch (fpi) or 39 fins per mm or more, interfin spacing for channels as small as about 0.0004 in. (0.010 mm) with fins up to as high as about 0.03 in. (0.76 mm), depending on the material (copper, copper alloys, aluminum, low carbon and stainless steels, titanium, plastic, PTFE, etc.). Wetted surface area ratios relative to the base area can be as high as 14 times! The fins can be made into closed multi-microchannel cooling elements by top flattening. It is possible to make these finned surfaces into ultra-compact evaporators, condensers, single-phase heat exchangers, etc.

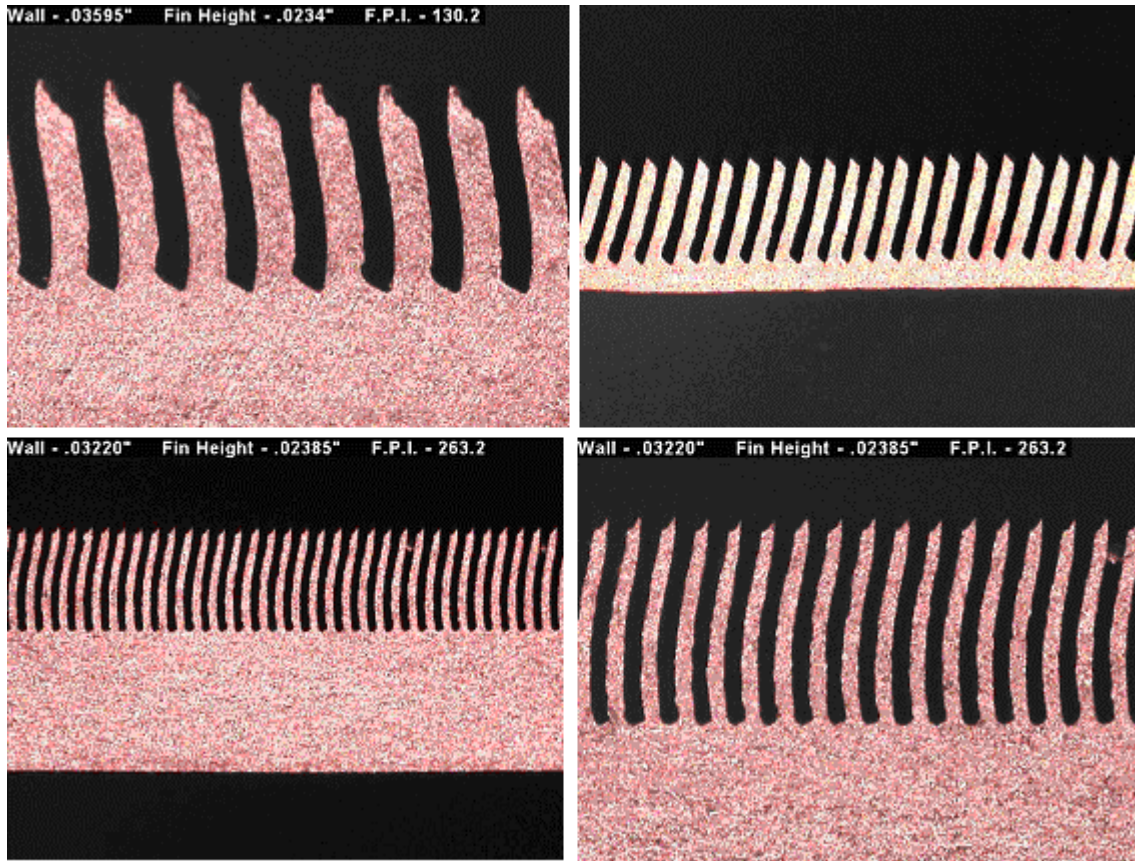


**Figure 20.1.** Photographs of ultra high density finned surfaces manufactured with Wolverine Tube Inc. Micro Deformation Technology (MDF). Upper left: 130 fpi (5.1 fin/mm) surface; upper right: 185 fpi (7.3 fins/mm) surface with fin height of 0.022 in. (0.56 mm) and fin thickness one-half of fin pitch; lower left and right: 263.2 fpi (10.4 fins/mm) surface. For more information on these surfaces and their applications, click [here](#).

## 20.2 Macro-to-Microscale Transition in Two-Phase Flow and Heat Transfer

In general, two-phase flow pattern maps and flow boiling heat transfer prediction methods developed for macroscale applications (typically based on databases with channel sizes ranging from about 3 mm up to about 20 mm) are not very accurate or reliable when extrapolated down to channel sizes below 1 to 2 mm. Hence, this points specifically to the need to develop macro-to-micro transition criteria to predict the lower boundary of the macroscale and the upper boundary of the microscale, with a transition region in between (that could be called the *mesoscale* or *miniscale* in order to give it a name). In principle, this means that in the domain of two-phase flow and heat transfer, a well-proven criterion is required for predicting the limiting diameter *above* which macroscale methods and theory are applicable and a second well-proven criterion for predicting the limiting diameter *below* which microscale methods and theory are reliably applicable, with both criteria based on local flow variables and physical properties of the fluid (and perhaps also a function of the flow pattern), and backed not only by numerous flow observations but also by extensive databases for boiling heat transfer, critical heat flux (CHF), condensation, two-phase pressure drops and void fraction measurements. Furthermore, methods are also required for predicting thermal performance in channel sizes falling in between, in the so-called *mesoscale*. While largely yet

unexplored, one can expect that a further *nanoscale* two-phase flow and heat transfer domain may emerge as well for even smaller sizes of channels where yet other two-phase mechanisms control the process.

As of today, there appears to be no exact definition or proven criterion available (it is the topic of contemporary research) for definitively distinguishing the transition between *macroscale* and *microscale* for two-phase flows and heat transfer. Notably, this is a completely separate issue from that of single-phase gas and liquid flows in small channels. Hence, without such a well agreed upon set of criteria to segregate data and methods, in this chapter the microscale is defined quite loosely based on current knowledge and perceptions of the present author and/or by how the particular authors of publications auto-classified their results. In fact, the International Conference on Microchannels and Minichannels uses directly microchannels and minichannels in its title, where macrochannels were loosely defined as those larger than 3 mm in diameter, minichannels from 0.6 to 3.0 mm, and microchannels below 0.6 mm along the suggestion of Kandlikar (2001).

From a phenomenological viewpoint, some macroscale thermal and fluid phenomena may be suppressed or relegated to secondary importance by the decrease in channel size while others may be enhanced or newly created. On the other hand, there does not appear to be a wholesale rupture between these two scales, but instead a gradual change over a range of diameters. Furthermore, most of the basic premises of two-phase flow and heat transfer are valid in both scales, although the prediction methods often do not work very well when extrapolated into the other scale. From a practical point of view, it is necessary to be able to identify the lower limit of application of macroscale methods for flow boiling and the upper threshold for microscale methods. Apparently, among the first to recognize this problem were Mehendale and Jacobi (2000), who subdivided the macro-to-microscale transition into four size classes (for convenience of discussion): microscale (from 1  $\mu\text{m}$  to 100  $\mu\text{m}$ ), mesoscale (from 100  $\mu\text{m}$  to 1 mm), compact (from 1 mm to 6 mm) and macroscale (greater than 6 mm). Kandlikar and Grande (2003) more recently recommended the following four classifications based on channel size of typical heat exchanger applications: nanochannels ( $< 10 \mu\text{m}$ ), microchannels (10  $\mu\text{m}$  to 200  $\mu\text{m}$ ), minichannels (200  $\mu\text{m}$  to 3 mm) and conventional channels (greater than 3 mm). These dimensional criteria were proposed primarily to try to differentiate the emerging research work on small diameter channels from that done for larger channels, for which the experimental trends were observed to be noticeably different. Such fixed dimensional values do not however reflect the influence of the physical mechanisms or the physical properties of the two-phases on the transitions, and hence are not reliable as application guidelines for thermal design methods. For example, at high pressures bubbles tend to be very small in size, so a 1 mm channel may be much larger than bubbles generated by nucleate boiling. Hence, this process might function in the macroscale while the opposite is true at subatmospheric pressures. For the present, the above channel size indicators can be considered to be *rules-of-thumb* classifications.

### 20.2.1 Evidence of the macro-to-microscale transition

Some evidence to support the existence of the macro-to-microscale transitions is first presented below and then methods proposed so far that attempt to identify these thresholds are described.

**Flow pattern evidence for the transition.** Examining high definition videos of flow patterns of R-134a at 25°C (see Figure 20.2), it is seen that these annular and slug (elongated bubble) flows are already quite uniform in film thickness at the top and bottom in a 0.509 mm horizontal channel, which is not true when looking at 8-14 mm channels as can be seen in the videos in [Chapter 1](#). Figure 20.3 depicts the buoyancy effect on an elongated bubble in 2.0, 0.790 and 0.509 mm horizontal channels. In the 2.0 mm channel, no stratified flow was observed while the difference in film thickness at the top compared to that at the bottom is still quite noticeable. Similarly, the film thickness in the 0.790 mm channel is still not uniform above and below the bubble. In contrast, in the 0.509 mm channel, the film is quite uniform. Interpreting



these images and many others available in the literature, one ascertains that stratified-wavy and fully stratified flows disappear (more or less completely) in small horizontal channels. This transition is thus perhaps an indication of the lower boundary of macroscale two-phase flow, in this case occurring for a diameter somewhat greater than 2.0 mm. The upper boundary of microscale two-phase flow may be interpreted as the point in which the effect of gravity becomes insignificant, e.g. the bubble in the 0.509 mm channel is thus a microscale flow, with the transition occurring at about this diameter at the present test conditions.

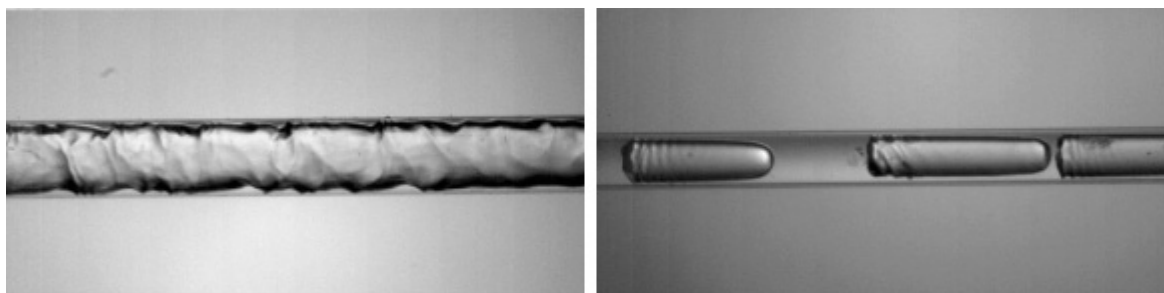


**Figure 20.2. Video images of annular flow and elongated bubble flow in a 0.509 mm horizontal channel with R-134a at 25°C at the exit of a micro-evaporator channel of the same diameter (images of R. Revellin of LTCM).**

Chen, Tian and Karayiannis (2006) did an extensive experimental study on the effect of tube diameter (1.01, 2.01, 2.88 and 4.26 mm) on two-phase flow regimes in vertical tubes using R-134a at saturation pressures from 6 to 14 bar. They concluded that none of the existing macroscale flow pattern maps were able to predict their observations. They also depicted an interesting presentation of flow pattern images for all the tube sizes. They found that confined bubble flow first appeared in their 1.10 mm tube, and tentatively deduced that the threshold distinguishing large tube from small tube characteristics was about 2 mm.

**Heat transfer evidence for the transition.** Several experimental studies have tested more than one channel diameter during flow boiling tests in small diameter channels, but so far these in themselves do not permit one to deduce any clear trend. For example, Yan and Lin (1998) concluded that boiling is more effective in a smaller diameter than in larger ones, based on tests in a test section with twenty-eight 2 mm channels with R134a at three saturation temperatures. But what happens when the diameter is decreased *within* the microscale range? Also, for flow boiling of R-134a in multi-channels with diameters of 0.77 and 2.01 mm tubes at a mass velocity of 285 kg/m<sup>2</sup>s, the data of Agostini (2002) showed higher heat transfer coefficients for their smaller channel but only for vapor qualities less than 0.25. For R-142b, Palm (2003) observed a moderate increase of the heat transfer coefficient when the channel diameter was decreased from 3.5, 2.5, 1.5 and 1.0 mm, tests done with glass test sections in a vertical orientation. Using the bubble confinement criterion of Kew and Cornwell (1997) described in the next section, the threshold diameter for macro-to-microscale transition equals 2.14 mm for R-142b at 15°C. Thus, these results seem to suggest an increase of the heat transfer coefficient in the passage from the macro-to-microscale.

For R-134a, Owhaib and Palm (2003) at 6.45 bar found that the average heat transfer coefficient increased when the diameter decreased from 1.7 mm to 0.8 mm. In this case, the Kew and Cornwell threshold diameter is 1.68 mm and their results confirm the above trends. For R-123, Baird et al. (2000) tested diameters of 0.92 and 1.95 mm and affirmed that the diameter had no significant effect on the heat transfer coefficient. The threshold diameter for this last fluid is 1.78 mm, so once again their results apparently fall in or near the macro-to-microscale transition zone. Khodabandeh (2003) studied boiling in a thermosyphon with isobutene as the working fluid with tube diameters ranging from 1.1 to 6 mm. He

concluded that the influence of diameter was slight and no clear trend was reported; on the other hand, it is difficult to obtain similar flow conditions when operating a thermosyphon.

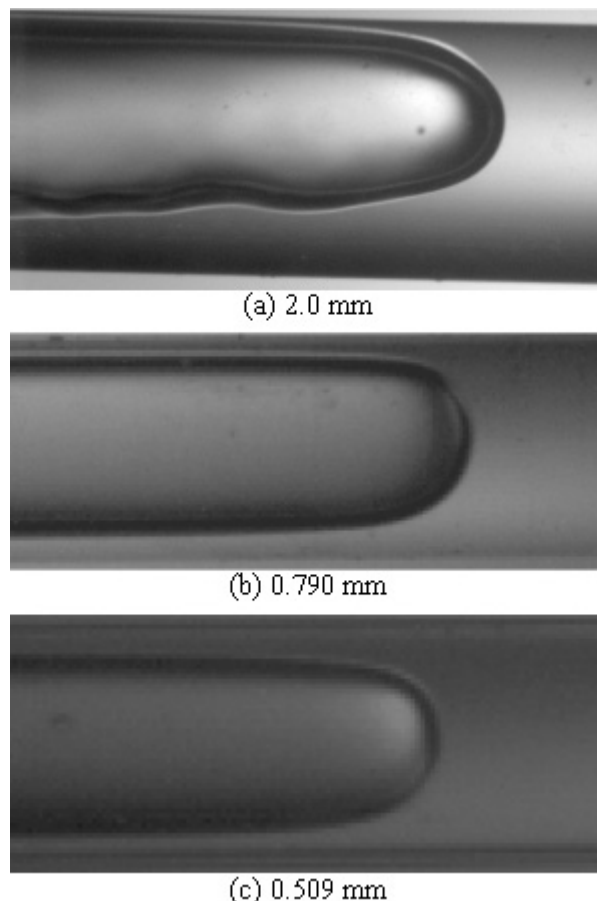


**Figure 20.3. Video images of slug (elongated bubble) flow in 2.0, 0.790 and 0.509 mm horizontal channels with R-134a at 30°C at the exit of a micro-evaporator channel of the same diameter (images of R. Revellin of LTCM).**

**CHF evidence for the transition.** Qu and Mudawar (2004) compared 414 CHF data points they obtained for water in small channels of 1.0 to 3.0 mm diameter and for R-113 in a 3.15 mm diameter channel to the widely quoted macroscale correlation of Katto and Ohno (1984), the latter correlation which is described in Chapter 18 in this book. The Katto-Ohno correlation was developed primarily for channel diameters of 3 mm and larger (only one set of data smaller than 3.0 mm was included in their database: liquid helium in a 1.0 mm channel). Qu and Mudawar (2004) found that this correlation was only partially successful for predicting their saturated CHF in single circular mini-channels, yielding a mean absolute error of 17.3% but with most of the data points falling within an error band of  $\pm 40\%$ . Thus, they proposed a new correlation to better describe their data. More recently, Wojtan, Revellin and Thome (2007) obtained saturated CHF data for R-134a and R-245fa in 0.509 and 0.790 mm circular channels over a wide range of mass velocities, and found a mean absolute error of 32.8% with only 41.2% of data falling within a  $\pm 15.0\%$  error band when compared to the Katto-Ohno correlation. Thus, these studies seem to indicate that there exists a macro-to-microscale two-phase flow transition in saturated CHF data.

**Void fraction evidence for transition.** Chung and Kawaji (2004) found that void fractions in 0.530, 0.250, 0.100 and 0.050 mm channels progressively deviated from the homogeneous void fraction law more and more sharply as the channel size was decreased, using water-nitrogen for tests in glass channels. Kawahara et al. (2005) found similar trends in their extended tests with nitrogen gas with water, ethanol and ethanol-water mixtures in channels ranging in diameter from 0.251 to 0.050 mm, for otherwise similar test conditions. Thus, these results can be interpreted as evidence of a macro-to-microscale two-phase flow transition or perhaps even a new smaller scale transition.

**Pressure drop evidence for transition.** Analysis of a large, multi-laboratory database of two-phase frictional pressure drops in channels ranging from about 0.1 to 3.0 mm in diameter extracted from the literature by Ribatski, Wojtan and Thome (2006) found that several widely quoted macroscale methods worked just as well as some of the new microscale methods. The homogeneous model worked surprisingly well for flows that would fall in the slug and annular flow regimes, in fact much better than it usually does in comparison to similar macroscale pressure drop data. These results and methods will be discussed later in this chapter, but it seems that pressure drop data at the moment do *not* sustain the existence of a macro-to-microscale transition in two-phase flow and thus requires a more detailed analysis than is feasible here to better understand this counter-intuitive trend compared to those above.

## 20.2.2 Macro-to-microscale transition criteria

Below, macro-to-microscale transition criteria for two-phase flows and heat transfer proposed in the literature are described. For now, it is recommended to use these criteria as tentative demarcations, as none of these methods has been widely tested.

**Confinement number approach.** In the microscale, the influence of gravity is surpassed by that of surface tension, i.e. no stratified flow exists if the tube diameter is sufficiently small. The Bond number  $Bd$  (also called the Eötvös number in the literature) gives the ratio of these forces for a tube of diameter  $d_i$ :

$$Bd = \frac{g(\rho_L - \rho_G)d_i^2}{\sigma} \quad [20.2.1a]$$

Based on a series of experimental studies, Kew and Cornwell (1997) empirically proposed the macro-to-microscale threshold diameter  $d_{th}$  to occur at  $Bd = 4$ , with values below 4 being in the microscale. According to them, for diameters lower than  $d_{th}$ , macroscale methods are not suitable for predicting flow boiling heat transfer coefficients or flow patterns, where rearranging  $d_{th}$  gives:

$$d_{th} = 2 \left( \frac{\sigma}{g(\rho_L - \rho_G)} \right)^{1/2} \quad [20.2.1b]$$

This is apparently the first criterion proposed for the threshold to confined bubble flow (where bubble diameters are rapidly limited by the channel diameter) and perhaps is thus the first macro-to-microscale two-phase flow transition criterion to be proposed and documented with some data, although it ignores the possibility of a transition regime between macroscale and microscale. Notably, this criterion also does not contain any flow forces, i.e. no superficial velocities nor shear effects on the bubbles or annular films. Kew and Cornwell in fact proposed their criterion in terms of a confinement number  $Co$  defined as follows:

$$Co = \left( \frac{\sigma}{g(\rho_L - \rho_G)d_i^2} \right)^{1/2} \quad [20.2.2]$$

This expression in reality utilizes the more commonly known Bond number as can be seen by comparison to that number's definition above. They reported that heat transfer and flow characteristics were significantly different than observed in macrochannels for  $Co > 0.5$ . As an example, for refrigerant R-134a at  $T_{sat} = 0^\circ\text{C}$ , the threshold diameter is given by this criterion to be 1.92 mm and becomes smaller as the saturation pressure increases.

Kawaji and Chung (2003) reviewed the characteristics of two-phase flow and the available data and came up with the following recommendation as a threshold criterion for defining microchannel two-phase flows based on a set of six dimensionless numbers (Bond number, superficial liquid and vapor Weber numbers, superficial liquid and vapor Reynolds numbers, and Capillary number) and the superficial vapor and liquid velocities:

$$Bd = \frac{g(\rho_L - \rho_G)d_i^2}{\sigma} \ll 4 \quad [20.2.3a]$$

$$We_{SL} = \frac{\rho_L U_L^2 d_i}{\sigma} \ll 1 \quad [20.2.3b]$$

$$We_{SG} = \frac{\rho_G U_G^2 d_i}{\sigma} \ll 1 \quad [20.2.3c]$$

$$Re_{SL} = \frac{\rho_L U_L d_i}{\mu_L} < 2000 \quad [20.2.3d]$$

$$Re_{SG} = \frac{\rho_G U_G d_i}{\mu_G} < 2000 \quad [20.2.3e]$$

$$Ca_L = \frac{\mu_L U_L}{\sigma} \ll 1 \quad [20.2.3f]$$

$$U_G = \frac{\dot{Q}_G}{A} \quad [20.2.3g]$$

$$U_L = \frac{\dot{Q}_L}{A} \quad [20.2.3h]$$

Hence, after applying first the Kew and Cornwell criterion, the other five criteria are then applied to further refine the microscale threshold analysis.

Continuing the earlier work of Brauner and Moalem-Maron (1992) on identification of the range of “small diameter” channels, Ullmann and Brauner (2006) suggested the macro-to-microchannel threshold to occur at an Eötvös number of about 0.2 (for air-water this corresponds to a diameter of about 0.35 mm), which in terms of the Confinement number mentioned above, gives the transition at somewhat lower diameters. The Eötvös number is defined as:

$$Eo = \frac{g(\rho_L - \rho_G)d_i^2}{8\sigma} \quad [20.2.4]$$



By inspection, one sees that  $Eo = Bd/8$ . Their recommendation came from analysis of the microscale flow pattern data of Triplett et al. (1999) for air-water in a 1.1 mm channel ( $Eo = 0.021$ ). Ullmann and Brauner (2006) concluded that the Eötvös number played a major role in flow pattern transitions and in determining the characteristic length in dispersed two-phase flows and in wall wetting effects in separated flows. Furthermore, it was found to be an important parameter in the disappearance of stratified flows and in determining when macroscale flow transition methods need to be substituted with microscale flow pattern transition methods. Hence, the Eötvös number appears to be a good candidate to be used as a criterion (or as part of a criterion) for defining the two-phase macro-to-microchannel transition. However, perhaps the earliest such macro-to-microscale transition criterion might be that of Bretherton (1961), who suggested a transition at  $Eo < 0.84$  as the threshold at which a Taylor bubble would no longer rise under only the influence of gravity in a vertical, water filled capillary tube.

**Bubble departure diameter approach.** Various studies have taken this approach. For example, based on the idea that no stratification exists at the microscale, Jacobi and Thome (2002) chose the bubble departure diameter as their determining criterion, that is the macro-micro transition was assumed to be reached when the diameter of a growing bubble reaches the internal diameter of the tube before detachment and then only grows in length as it flows downstream. Surveying the literature finds various studies on bubble departure for flow in channels that are large with respect to the bubble size, but no such results or prediction methods are apparently available when the bubble nearly blocks the channel during its growth while still attached to the wall. Using instead bubble departure diameter methods for nucleate pool boiling, that is without an imposed cross flow or confinement of the bubble, these readily applicable methods can give an approximate idea of bubble departure diameters that can be expected under actual channel conditions.

Jensen and Memmel (1986) reviewed the most widely quoted methods available to predict bubble departure diameters in nucleate pool boiling and compared them to a diversified database. For instance, the Fritz (1935) correlation gives the detachment diameter  $d_{bub}$  as:

$$d_{bub} = 0.0208\beta \left( \frac{\sigma}{g(\rho_L - \rho_G)} \right)^{1/2} \quad [20.2.5]$$

The contact angle  $\beta$  in this expression is in degrees ( $^\circ$ ). Nishikawa et al. (1976) gave the following expression:

$$d_{bub} = \left[ 0.12 + 0.08 \left( \frac{c_{pL} T_{sat}}{h_{LG}} \right)^{2/3} \right] \left( \frac{\sigma}{g(\rho_L - \rho_G)} \right)^{1/2} \quad [20.2.6]$$

This expression is described in the paper by Nakayama and Kano (1983). As can be seen, their expression includes the saturation temperature of the fluid, the specific heat of the liquid and the latent heat, but not the contact angle. Kutateladze and Gogonin (1979a) proposed the following expression:

$$d_{bub} = \left[ 0.25(1 + 10^5 K_1)^{1/2} \right] \left( \frac{\sigma}{g(\rho_L - \rho_G)} \right)^{1/2} \quad [20.2.7]$$

Their dimensionless parameter  $K_1$  is:

$$K_1 = \left( \frac{\rho_L c_{pL} (T_w - T_{sat})}{\rho_G h_{LG} Pr_L} \right)^2 \left[ \frac{\mu_L^2 [g(\rho_L - \rho_G)]^{1/2}}{\rho_L \sigma^{3/2}} \right] \quad [20.2.8]$$

Thus, their expression adds the influences of the wall superheat, liquid Prandtl number and liquid dynamic viscosity to the bubble departure criterion but again not the contact angle (whose value is difficult to come by). To obtain better accuracy for predicting their compiled database, Jensen and Memmel (1986) proposed the following variation to the above method where the definition of  $K_1$  remains the same:

$$d_{bub} = \left[ 0.19 (1.8 + 10^5 K_1)^{1/2} \right] \left( \frac{\sigma}{g(\rho_L - \rho_G)} \right)^{1/2} \quad [20.2.9]$$

It is interesting to notice the role played by the Bond number in all these relations, which are only strictly valid for pool boiling, while the flow in a microchannel will tend to promote the detachment of the bubble before it completely spans the channel. Thus, a macro-to-microscale criterion set equal to the passive bubble detachment diameter will probably overestimate the value of the channel diameter of the macro-to-microscale threshold.

**Young-Laplace equation approach.** Li and Wang (2003) carried out an analysis to study the gravitational effect on the transition from symmetric flow (where gravity can be ignored) to asymmetric flow (where gravity cannot be ignored) during *condensation* in small horizontal tubes. Based on the Young-Laplace equation, they proposed the following critical and threshold values of the tube diameter  $d_{crit}$  and  $d_{th}$  in terms of the capillary length  $L_{cap}$  as:

$$d_{crit} = 0.224 L_{cap} \quad [20.2.10]$$

$$d_{th} = 1.75 L_{cap} \quad [20.2.11]$$

The capillary length is given as:

$$L_{cap} = \left( \frac{\sigma}{g(\rho_L - \rho_G)} \right)^{1/2} \quad [20.2.12]$$

Their critical diameter is similar to the bubble departure diameter in the Fritz equation above if the contact angle is set to  $10^\circ$ . Furthermore, their threshold diameter differs from that of Kew and Cornwell (1997) only by the value of the multiplier, i.e. 1.75 rather than 2.0. Based on these definitions, Li and Wang proposed to subdivide condensation flow regimes as follows relative to the channel diameter  $d_i$ :

- When  $d_i \leq d_{crit}$ , the effect of gravity is insignificant and the annular, elongated bubble and bubble flow regimes should be symmetric;
- When  $d_{crit} \leq d_i \leq d_{th}$ , the effect of gravity is visible but the surface tension effect is dominant, which creates some non-symmetric effects on the annular, elongated bubble and bubble flow regimes;
- When  $d_i \geq d_{th}$ , the effect of surface tension will be small with respect to gravity and the condensation flow regimes will be similar to those in macrochannels.

Hence, this is apparently the first proposition for macro-to-mesoscale and meso-to-microscale threshold criteria in the literature, which could also be applicable to adiabatic flows and flow boiling. As an example, for R-134a at 30°C, the values of  $d_{crit}$  and  $d_{th}$  are 0.183 mm and 1.429 mm, respectively, while for water at 27°C they are much larger, 0.600 mm and 4.680 mm, primarily due to this fluid's large surface tension.

Figure 20.4 depicts a comparison of selected macro-to-microscale threshold criteria evaluated for R-134a as a function of reduced pressure. Only two of the three Mehendale and Jacobi (2000) divisions are shown in the diagram, which subdivides the channel diameters into four size classes: microscale, mesoscale, compact and macroscale (the 1  $\mu$ m threshold is not shown as it is too small on the present axis). Two of the three Kandlikar and Grande (2003) divisions are shown that separate the channel diameters into nano-, micro-, mini- and macro-sizes (the 10  $\mu$ m line is not shown as it is too small on the present axis). It is seen that the Kew and Cornwell (1997) Confinement number, the Ullmann and Brauner (2006) Eötvös number and the Li and Wang (2003) threshold diameter give approximately similar values and trends with respect to the reduced pressure. Interestingly, the critical diameter of Li and Wang (2003) is similar to the bubble departure diameter prediction of Jensen and Memmel (1986) assuming a contact angle of 35°. The effect of fluid properties is important and hence the fixed diameter thresholds are seen not to be realistic but only act as rough guidelines.

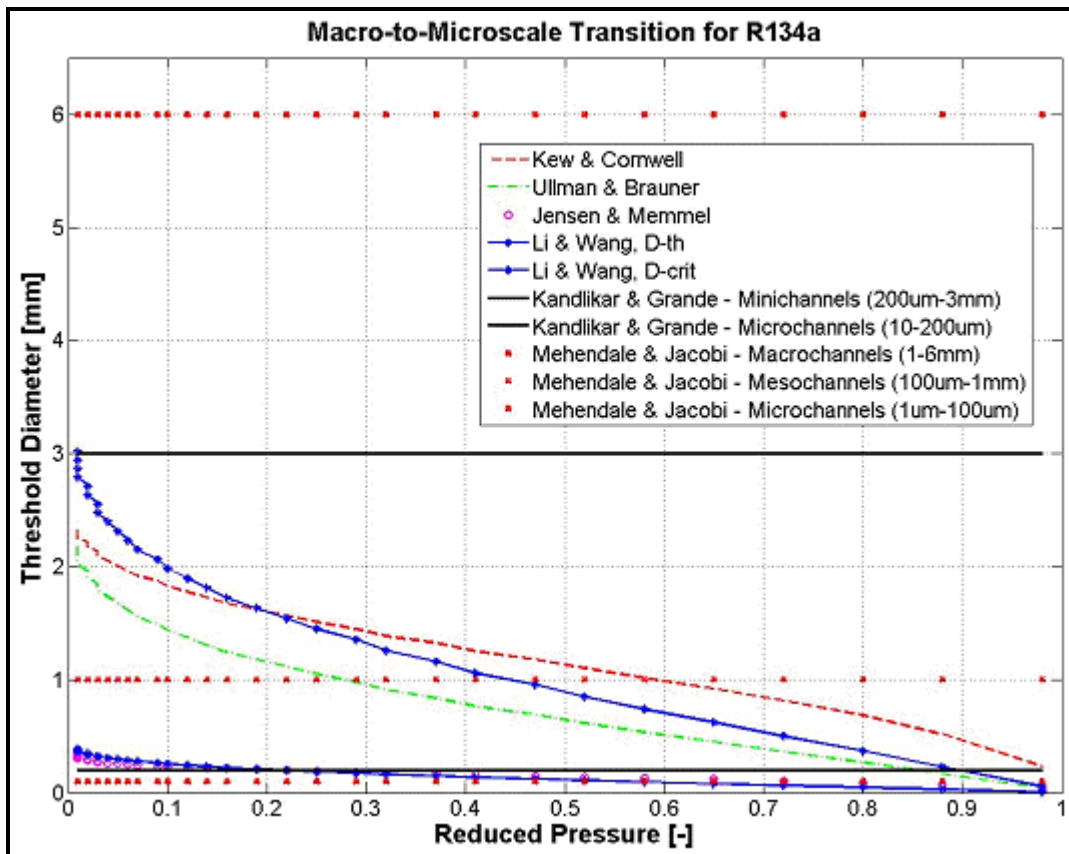


**Figure 20.4. Comparison of selected macro-to-microscale transition criteria for R-134a as a function of reduced pressure (the points are simulations, not data points).**

**Numerical approaches.** Onbasioglu (2004) applied the Volume of Fluid (VOF) and Eulerian methods in a commercial numerical fluid dynamics software to simulate two-phase flows inside small channels. After validation of the computation procedures versus some macroscale flow pattern observations, he played

with the channel size to try to discern the transition point where the “conventional” governing equations failed. Based on his simulations, he proposed a qualitative two-phase macro-to-microscale transition for air-water to be about 1.0 mm in diameter, a value that fits within the ranges above.

More recently, Zun (2007) presented detailed numerical simulations of elongated bubble flows in horizontal channels. He compared the liquid film thickness at the top of the bubble to that at the bottom of the bubble for R-134a at a saturation pressure of 7.74 bar ( $T_{\text{sat}} = 30^\circ\text{C}$ ) as a function of channel diameter and in terms of the bubble Reynolds number  $Re$ , the Eötvös number  $Eo$ , the Archimedes  $Ar$ , the Weber  $We$ , the Froude number  $Fr$ , and the Capillary number  $Ca$ . The dimensionless numbers refer to the bubble “nose diameter” denoted by  $d_{\text{bub}}$  while  $u_G$  stands for the bubble velocity. These numbers were defined in his study as follows:

$$Re = \frac{\rho_L u_G d_{\text{bub}}}{\mu_L} \quad [20.2.13]$$

$$Ar = \frac{g \rho_L (\rho_L - \rho_G) d_{\text{bub}}^3}{\mu_L^2} \quad [20.2.14]$$

$$We = \frac{\rho_L u_G^2 d_{\text{bub}}}{\sigma} \quad [20.2.15]$$

$$Fr = \frac{u_G^2}{g d_{\text{bub}}} \quad [20.2.16]$$

$$Ca = \frac{\mu_L u_G}{\sigma} \quad [20.2.17]$$

$$Eo = \frac{g(\rho_L - \rho_G) d_{\text{bub}}^2}{\sigma} \quad [20.2.18]$$

The basic idea in the top to bottom liquid film thickness ratio was to account for the different forces acting on the shape of the moving bubble and the resulting relative thickness of the liquid films. The results of the calculations are shown in Figure 20.5, where the ratio of the liquid film thickness at the top of the bubble to the thickness at the bottom is plotted. Using the commercial numerical fluid dynamics code, Rek and Zun of the Laboratory of Fluid Dynamics and Thermodynamics, University of Ljubljana, Slovenia found that the film only became uniform in thickness at the top and bottom of the bubble when the channel size reached about 0.1 mm while for a 0.5 mm diameter channel the film at the top was about 25% thinner than at the bottom. Hence, for this flow regime, from a two-phase flow point of view, one criterion for the upper boundary of the microscale region could be taken as the point of uniformity of the liquid film around an elongated bubble, giving values comparable to those of Li and Wang (2003) above.

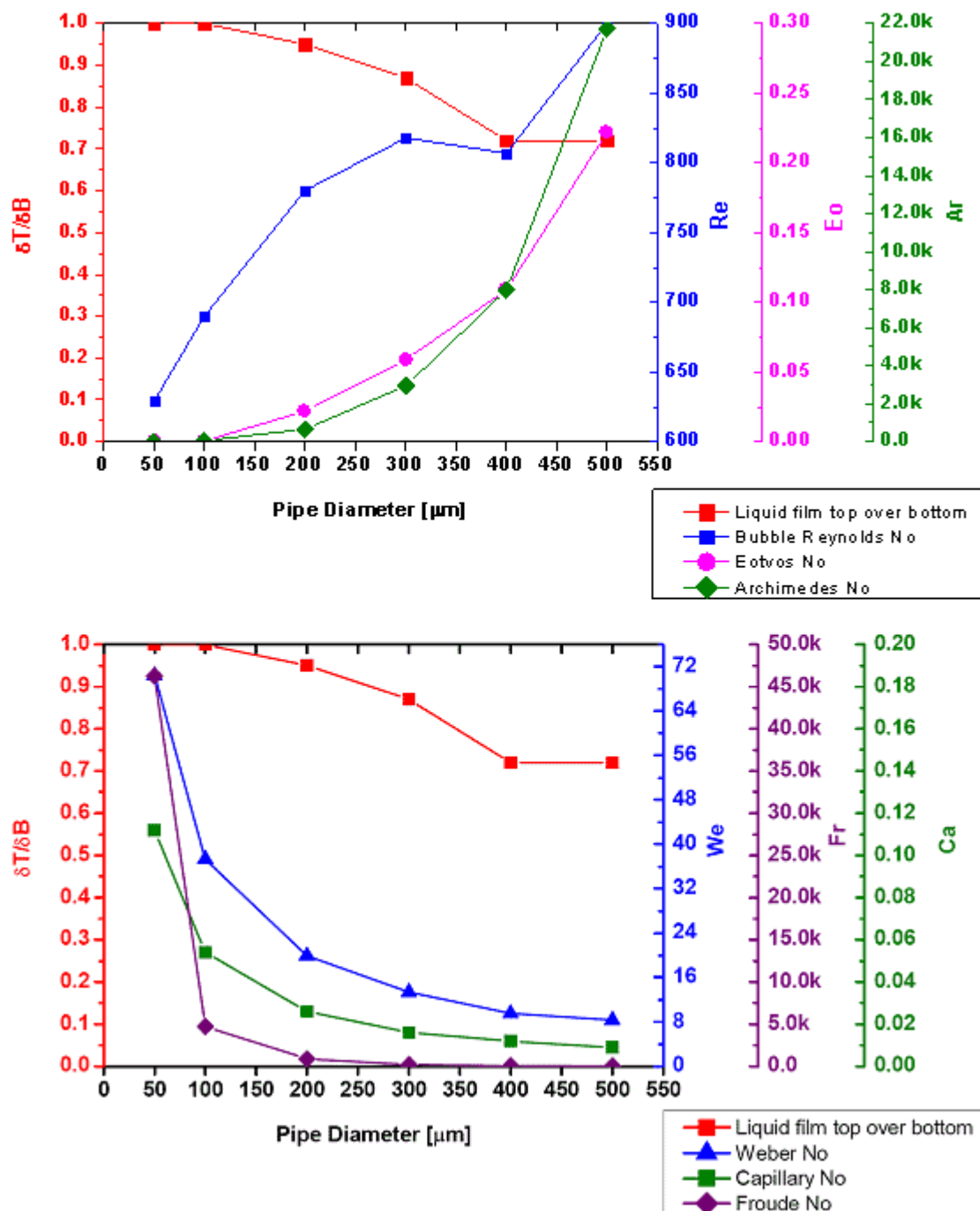
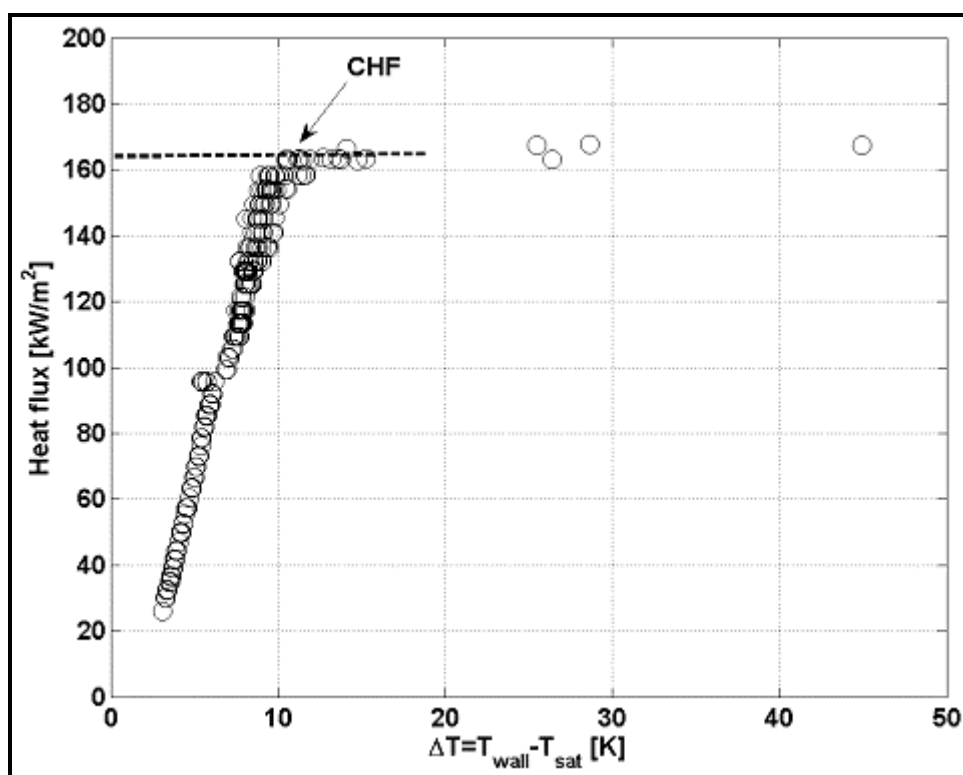


Figure 20.5. Numerical simulation of slug flow of elongated bubbles in small, horizontal channels presented by Zun (2007) for R-134a at 7.74 bar, showing the ratio of the liquid film thickness at the top of the bubble ( $\delta T$ ) to that at the bottom of the bubble ( $\delta B$ ), plotted versus the six relevant dimensionless numbers.



## 20.3 Critical Heat Flux in Microchannels

For high heat flux cooling applications using flow boiling in multi-microchannels, the critical heat flux (CHF) in saturated flow boiling conditions is a very important operational limit. It signifies the maximum heat flux that can be dissipated at the particular operating conditions. Surpassing CHF means that the heated wall becomes completely and irrevocably dry, and is associated with a very rapid and sharp increase in the wall temperature as the flow passes into the mist flow (or post-dryout) heat transfer regime. For example, Figure 20.6 illustrates the onset of CHF in single microchannel tests of Wojtan, Revellin and Thome (2007) showing the temperature excursion that occurs during small steps of increasing heat flux. For most applications, this temperature excursion will result in irreparable damage to the device being cooled, such as a computer's CPU or a power electronics board. Thus, critical heat flux is particularly important design parameter in microchannel boiling applications. Physically speaking, CHF in an annular flow is reached by dryout or entrainment of the liquid film, which leaves the wall dry.



**Figure 20.6.** Heat flux versus wall superheat measurements during a critical heat flux experiment by Wojtan, Revellin and Thome (2007). The test was done with R-134a at a saturation temperature of 30°C, at a mass velocity of 1000 kg/m<sup>2</sup>s, in a channel diameter of 0.509 mm and for a heated length of 70 mm.

Below, first the theoretical upper limit of CHF is discussed, then experimental results together with their associated empirical CHF prediction methods are presented, and then the first theoretical microchannel CHF model is described. The topic of modeling of local CHF under hot spots for computer chip cooling is then addressed.

### 20.3.1 Upper Limit of CHF

With very high heat flux cooling applications in mind, various researchers have tried to respond to the question: “*What is the upper limit of the critical heat flux?*” Independent studies done by Schrage (1953) and Tien and Lienhard (1976, 1979) have been summarized by Gambill and Lienhard (1989). They noted that, if one could contrive to collect every vapor molecule that leaves a liquid-vapor interface without permitting any vapor molecule to return to the liquid, then the maximum heat flux  $q_{\max}$  is:

$$q_{\max} = \rho_G h_{LG} \left( \frac{RT_{\text{sat}}}{2\pi M} \right)^{1/2} \quad [20.3.1]$$

where  $q_{\max}$  is the highest heat flux that can conceivably be achieved in a phase transition process,  $R$  is the ideal gas constant and  $M$  is the molecular weight. This equation is based on kinetic theory and the average speed of a Maxwellian gas. Perhaps surprisingly, surface tension does *not* appear in this expression.

Figure 20.7 shows the variation of the upper limit of the maximum heat flux as a function of reduced pressure for refrigerants R-245fa and R-134a. As can be seen, the maximum heat flux increases for both refrigerants with increasing reduced pressure, reaches a peak at  $p_r = 0.85$ , and then decreases to zero. The potential maximum heat flux is extremely large, surpassing 1000 MW/m<sup>2</sup>! This theory shows that astonishingly high values of heat fluxes might seem to be attainable but there are several reasons that this upper limit cannot be attainable in practice. The most serious restriction is that many vapor molecules will inevitably return to the vapor-liquid interface. Another problem lies in the premise that all the heat ultimately passes through a liquid-vapor interface, according to Gambill and Lienhard (1989).

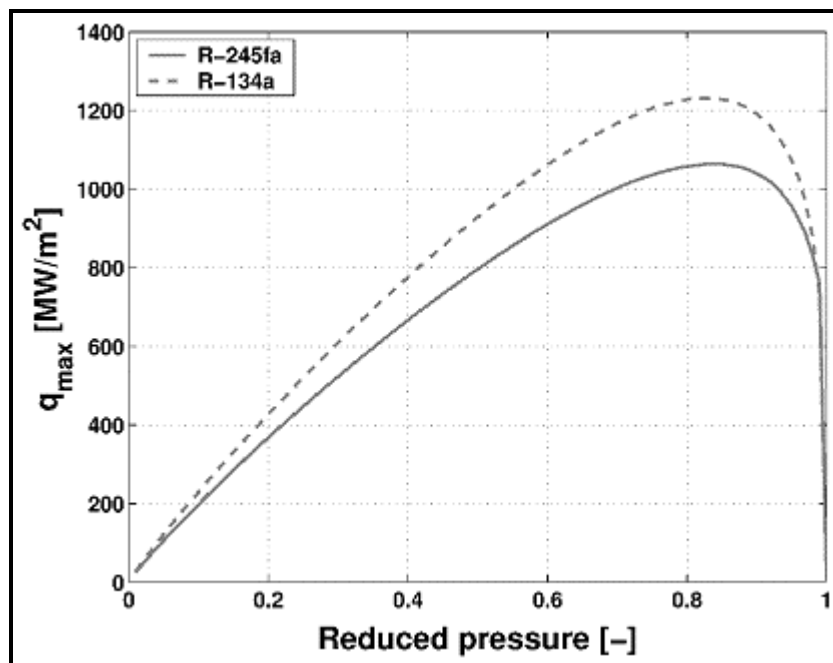


**Figure 20.7. Dependence of  $q_{\max}$  on reduced pressure for R-245fa and R-134a.**

The highest heat flux values obtained experimentally are on the order of about one-tenth of the values predicted by [20.3.1] for water in Ornatski and Vinyarsk (1965) and the order of one-hundredth for refrigerants R-113 and R-12 in Katto and Shimizu (1979). In those tests, the CHF for water was measured

in a 0.5 mm internal diameter channel and for the refrigerants was measured by Katto and Shimizu (1979) using impinging liquid jets under a wide range of elevated pressures. From the practical point of view, the achievable target level of realizable CHF appears to be about  $0.1q_{\max}$ . If burnout consistently reaches one tenth of the limit, then burnout is occurring because molecular diffusion fails to provide sufficient cooling. Molecular diffusion is an unobserved until now burnout mechanism according to Gambill and Lienhard (1989).

### 20.3.2 Experimental Studies and Correlations for CHF in Microchannels

Bergles and Kandlikar (2005) reviewed the existing studies on critical heat flux in microchannels and the reader is referred to their article for full details. They concluded by saying that single-tube CHF data were not available for microchannels at the time of their review. For the case of parallel multi-microchannels, they noted that all the available CHF data were taken under unstable conditions, where the critical condition was reached as the result of a compressible volume instability upstream or the parallel channel Ledinegg instability. As a result, the unstable CHF values reported in the literature were expected to be lower than they would be if the channel flow were kept stable by an inlet restriction. Regarding macroscale CHF, the Katto and Ohno (1984) method described in Chapter 18 in this book is usually considered the most accurate and reliable one.

Pribyl, Bar-Cohen and Bergles (2003) have studied the effect of flow pattern on CHF, based on water data obtained in three independent test facilities with a total number of experimental points of 4109. The tube diameters ranged from 1.0 to 37.0 mm, heated lengths from 31 to 3000 mm and mass velocities from 10 to 18580 kg/m<sup>2</sup>s. The database was sorted by regime using Taitel and Dukler (1976) flow pattern map (described in the flow pattern chapter in this book) to identify annular, intermittent and bubble flows. They found that CHF varied linearly with quality in distinct segments, with a relatively sharp discontinuity and change in slope at low vapor qualities, where the Taitel-Dukler map predicts a regime transition. The most apparent difference in slope was observed between bubble and annular flows. They concluded that a change in flow regime might affect the mechanism of CHF and that within each flow regime a similar but distinct CHF mechanism could be expected to apply.

Some of the earliest CHF data for saturated CHF in small diameter tubes were obtained by Lazarek and Black (1982). They obtained a limited number of measurements for R-113 in a single 3.15 mm bore, stainless steel tube with a heated length of 126 mm. For parallel multi-microchannels, Bowers and Mudawar (1994) obtained perhaps the first such CHF data for R-113 in two test sections, one with 0.510 mm channels and the other with 2.54 mm channels, both circular, with a heated length of 10 mm made of copper and nickel.

Shah (1987) proposed a correlation for CHF in uniformly heated vertical channels created from a database covering 23 fluids (water, cryogenics, organics and liquid metals) for tube diameters varying from 0.315 mm to 37.5 mm and heated length to diameter ratios from 1.2 to 940, taking data from 62 independent sources. His correlation is given as follows:

$$\frac{q_{\text{crit}}}{\dot{m} h_{\text{LG}}} = 0.124 \left( \frac{L_h}{d_i} \right)^{-0.89} \left( \frac{10^4}{Y_{\text{Shah}}} \right)^n (1 - x_{\text{inlet}}) \quad [20.3.2]$$

In this expression,  $x_{\text{inlet}}$  is the inlet vapor quality, which can be negative when considering a subcooled inlet condition, i.e. the inlet subcooling enthalpy relative to the latent heat. As CHF normally occurs at the outlet, the heated length  $L_h$  is taken as the channel length. The new parameter  $Y_{\text{Shah}}$  is:

$$Y_{\text{Shah}} = \dot{m}^{1.8} d_i^{0.6} \left( \frac{c_{pL}}{k_L \rho_L^{0.8} g^{0.4}} \right) \left( \frac{\mu_L}{\mu_G} \right)^{0.6} \quad [20.3.3]$$

When  $Y_{\text{Shah}} \leq 10^4$ , then  $n = 0$ . When  $Y_{\text{Shah}} \geq 10^4$ , then  $n$  is calculated as follows:

$$Y_{\text{Shah}} \leq 10^6, n = \left( \frac{d_i}{L_h} \right)^{0.54} \quad [20.3.4a]$$

$$Y_{\text{Shah}} > 10^6, n = \frac{0.12}{(1 - x_{\text{inlet}})^{0.5}} \quad [20.3.4b]$$

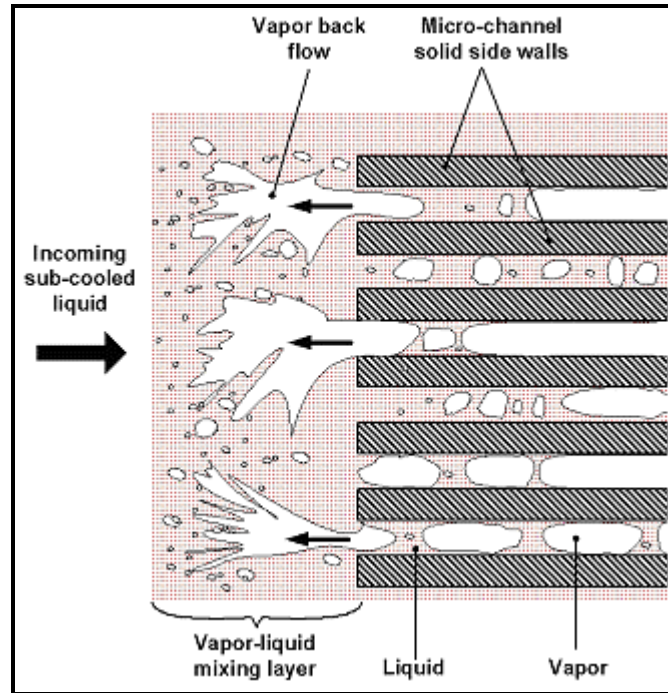


**Figure 20.8. Qu and Mudawar (2004) sketch of flow instabilities near CHF point they observed in their multi-microchannel heat sink.**

Qu and Mudawar (2004) obtained CHF data for water in a multi-microchannel heat sink with 21 parallel rectangular channels of 0.215 mm width by 0.821 mm height. They found that as CHF was approached, flow instabilities induced vapor backflow into the heat sink's upstream plenum as shown in Figure 20.8, resulting in mixing vapor with the incoming subcooled liquid. The backflow negated any advantage of inlet subcooling, resulting in a CHF virtually independent of inlet subcooling. Using these data together with the previously mentioned CHF data of Bowers and Mudawar (1994), their new Katto-Ohno style empirical correlation with CHF occurring in saturated flow was developed as follows:

$$\frac{q_{\text{crit}}}{\dot{m} h_{\text{LG}}} = 33.43 \left( \frac{\rho_G}{\rho_L} \right)^{1.11} \text{We}_L^{-0.21} \left( \frac{L_h}{d_i} \right)^{-0.36} \quad [20.3.5]$$

The liquid Weber number, based on the uniformly heated length  $L_h$ , is defined as:

$$We_L = \frac{\dot{m}^2 L_h}{\rho_L \sigma} \quad [20.3.6]$$

This correlation predicts their experimental database for water and R-113 with a very small mean absolute error of 4%.

Zhang et al. (2006) analyzed the existing CHF correlations available for water versus experimental data for small diameter channels ( $0.33 \text{ mm} \leq d_i \leq 6.22 \text{ mm}$ ) and proposed the following correlation for CHF of saturated water in small channels:

$$\frac{q_{crit}}{\dot{m} h_{LG}} = 0.0352 \left[ We_{d_i} + 0.0119 \left( \frac{L_h}{d_i} \right)^{2.31} \left( \frac{\rho_G}{\rho_L} \right)^{0.361} \right]^{-0.295} \left( \frac{L_h}{d_i} \right)^{-0.311} \cdot \left[ 2.05 \left( \frac{\rho_G}{\rho_L} \right)^{0.170} - x_{inlet} \right] \quad [20.3.7]$$

The liquid Weber number, based on the channel diameter is defined as:

$$We_{d_i} = \frac{\dot{m}^2 d_i}{\rho_L \sigma} \quad [20.3.8]$$

Qi et al. (2007a, 2007b) have measured cryogenic CHF data for saturated liquid nitrogen for 0.531, 0.834, 1.042 and 1.931 mm circular microchannels. The tests were done for mass velocities from about 400 to 2800 kg/m<sup>2</sup>s at saturation pressures of about 6.8 bars. They found that the correlation of Katto and Ohno (1984), presented elsewhere in this book, and that of Zhang et al. (2006), presented above for water, tended to severely under predict their nitrogen data by 65-80%. Therefore, they proposed a new correlation based on the Weber number and the Confinement number as follows for CHF of liquid nitrogen:

$$\frac{q_{crit}}{\dot{m} h_{LG}} = (0.214 + 0.140 Co) \left( \frac{\rho_G}{\rho_L} \right)^{0.133} We_{d_i}^{-0.333} \left( \frac{1}{1 + (0.03 L_h / d_i)} \right) \quad [20.3.9]$$

This method fits their nitrogen data with a mean average error of about 7.4%.

Wojtan, Revellin and Thome (2007) ran CHF tests in 0.509 mm and 0.790 mm internal diameter stainless steel microchannel tubes as a function of refrigerant mass velocity, heated length, saturation temperature and inlet liquid subcooling for R-134a and R-245fa. The heated lengths of microchannels were varied from 20 to 70 mm. The results showed a strong dependence of CHF on mass velocity, heated length and microchannel diameter but no measurable influence of liquid subcooling (2 to 15 K) was observed. An example of their results is shown in Figure 20.9. To put these values in perspective, the departure from nucleate boiling using the expression of Lienhard and Dhir (1973) yields a value of  $q_{DNB} = 384 \text{ kW/m}^2$ , which is similar to the maximum value in the graph. All their CHF results corresponded to annular flow conditions at the exit of the microchannel based on flow pattern results obtained separately in the same test sections. Their experimental results were compared to the CHF single-channel correlation of Katto and Ohno (1984) and the multi-channel CHF correlation of Qu and Mudawar (2004). The correlation of



Katto-Ohno predicted their microchannel data better with a mean absolute error of 32.8% but with only 41.2% of the data falling within a  $\pm 15\%$  error band. The correlation of Qu and Mudawar (2004) exhibited the same trends as their CHF data but significantly over predicted their data. Based on their own experimental data, a new microscale version of the Katto-Ohno correlation for the prediction of CHF during saturated boiling in microchannels was proposed by Wojtan, Revellin and Thome (2007) as:

$$\frac{q_{\text{crit}}}{\dot{m} h_{\text{LG}}} = 0.437 \left( \frac{\rho_G}{\rho_L} \right)^{0.073} \text{We}_L^{-0.24} \left( \frac{L_h}{d_i} \right)^{-0.72} \quad [20.3.10]$$

$\text{We}_L$  is determined using the expression [20.3.6] above. The experimental points are predicted with the mean absolute error of 7.6% with 82.4% of data falling within a  $\pm 15.0\%$  error band. The database behind this correlation covers: two fluids (R-134a and R-245fa), two diameters (0.509 and 0.790 mm), numerous mass velocities (400 to 1600  $\text{kg/m}^2\text{s}$ ), four heated lengths (20 to 70 mm), two saturation temperatures (30 and 35°C) and small subcoolings (2 to 15 K). Regarding the dimensionless ratios, they ranged as follows: 293-21044 for  $\text{We}_L$ , 0.009-0.041 for  $\rho_G/\rho_L$ , and 25-141 for  $L_h/d_i$ .

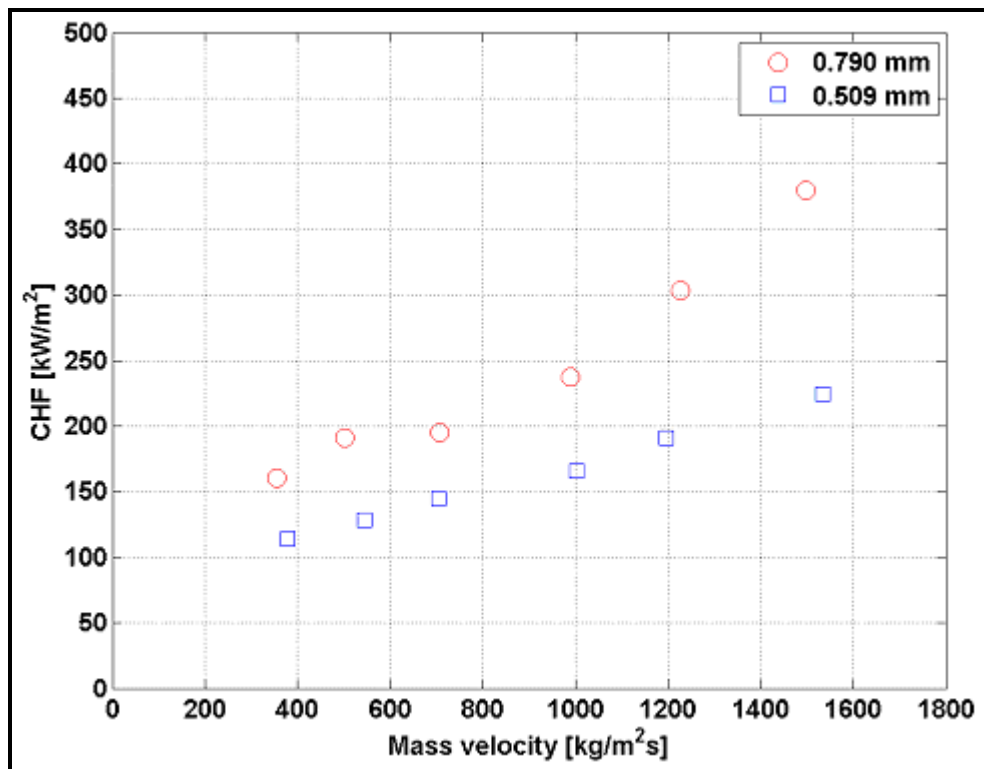


**Figure 20.9.** Wojtan, Revellin and Thome (2007) CHF data as a function of mass velocity for R-134a at a saturation temperature of 35°C, a heated length of 70 mm and inlet subcooling of 8K.

More recently, additional multi-microchannel CHF data have become available. Agostini et al. (2008c) measured CHF for R-236fa in a silicon test section with a special inlet header to provide stable flow and good flow distribution (the joining of the inlet liquid distributor to the microchannels created a rectangular orifice at the inlet of each channel). Figure 20.10 depicts some of their test results, demonstrating a significant effect of mass velocity as expected. On the other hand, small variations in inlet subcooling from 0.8 to 18K had essentially no effect on the results, primarily because the inlet

orifices had a beneficial flashing effect of triggering flow boiling without passing through the onset of nucleate boiling. The wetted wall heat fluxes accounting for the fin efficiency are plotted (not including the top glass plate used for viewing of the process), which ranged from about 219 to 522 kW/m<sup>2</sup>. These values correspond to cooling rates 1120 to 2500 kW/m<sup>2</sup> in terms of the footprint of the test section (i.e. at these conditions, 112 to 250 W/cm<sup>2</sup> could be dissipated from a microprocessor chip of 20 mm by 20 mm). The CHF correlation of Wojtan, Revellin and Thome (2007) described above and the Revellin and Thome (2008) theoretical CHF model (described below) were both found to predict all their 26 CHF data points within ±20%.

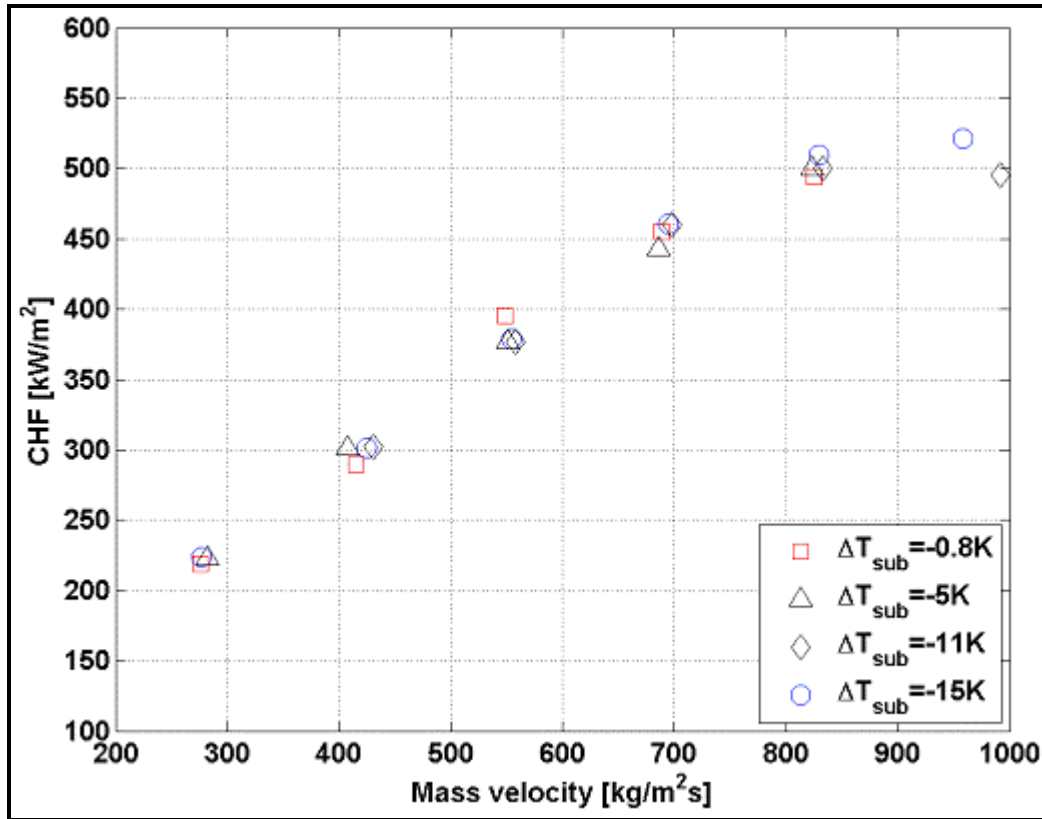


**Figure 20.10. Agostini et al. (2008c) CHF data as a function of mass velocity and inlet subcooling for R-236fa, at an inlet saturation temperature of 26°C. Boiling was in a silicon multi-microchannel element with a heated length and width of 20 mm, with 67 channels of 0.223 mm width, 0.680 mm high and 0.080 mm thick fins.**

For a uniformly heated circular channel, the critical vapor quality can be obtained from a simple energy balance as follows:

$$x_{\text{crit}} = \left( \frac{q_{\text{crit}}}{\dot{m} h_{\text{LG}}} \right) \left( \frac{4L_h}{d_i} \right) - \left( \frac{h_{\text{sub}}}{h_{\text{LG}}} \right) \quad [20.3.11]$$

In this expression,  $q_{\text{crit}}$  is calculated with the correlation of choice, while  $h_{\text{LG}}$  is the latent heat of vaporization and  $h_{\text{sub}}$  is the enthalpy change necessary to bring the incoming subcooled liquid to saturation. Thus, from a design point of view, once the critical heat flux is known, the maximum exit vapor quality to avoid CHF can be calculated. It should be pointed out that  $x_{\text{crit}}$  is not often the same value as  $x_{\text{di}}$ , which is the onset of dryout, since the latter can occur from a hydrodynamic effect at low heat flux.

### 20.3.3 Mechanistic Model for CHF in Microchannels

Revellin and Thome (2008) have proposed a mechanistic model for predicting critical heat flux in microchannels. Their model is based on the premise that CHF is reached when local dryout occurs during evaporation in annular flow at the location where the height of the interfacial waves reaches that of the annular film's mean thickness. To implement the model, they first solve one-dimensionally the conservation equations for mass, momentum and energy, assuming annular flow for determining the variation of the annular liquid film thickness  $\delta$ , and ignoring any interfacial wave formation, along the channel. Then, based on the slip ratio and a Kelvin-Helmoltz critical wavelength criterion (assuming the film thickness to be proportional to the critical wavelength of the interfacial waves), the wave height  $\Delta\delta$  was modelled with the following empirical expression:

$$\Delta\delta = 0.15 \left( \frac{d_i}{2} \right) \left( \frac{u_G}{u_L} \right)^{-\frac{3}{7}} \left( \frac{g(\rho_L - \rho_G)(d_i/2)^2}{\sigma} \right)^{-\frac{1}{7}} \quad [20.3.12]$$

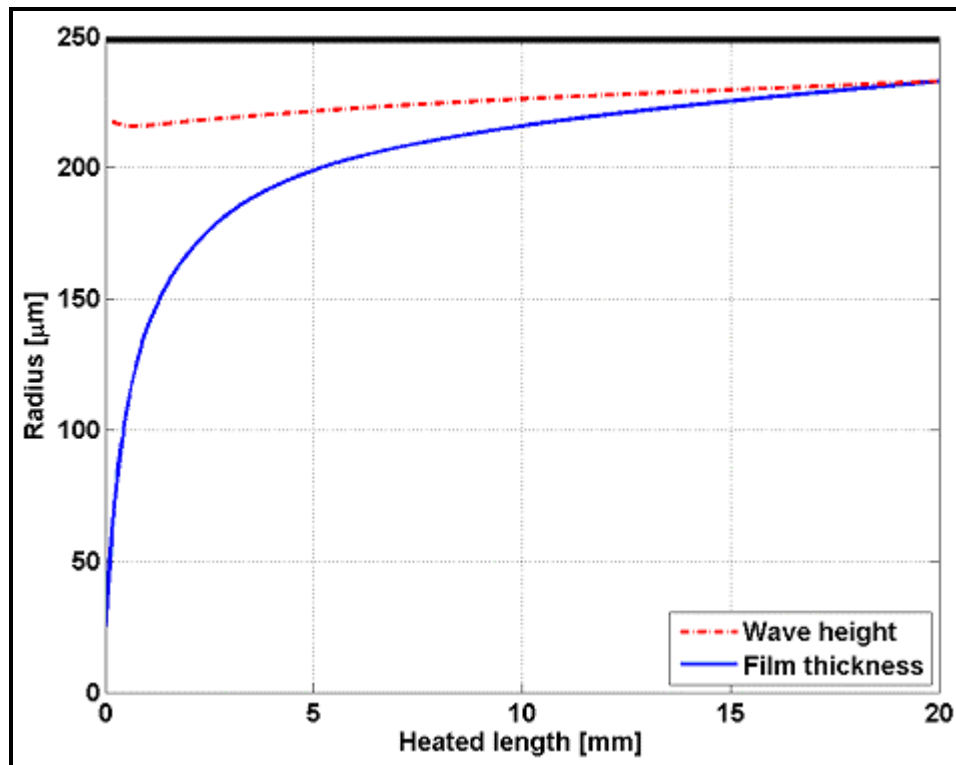


**Figure 20.11. Revellin and Thome (2008) CHF model showing the annular film thickness variation along the channel plotted versus the wave height with respect to the channel centerline. The simulation is for R-134a at a saturation temperature of 30°C in a 0.5 mm channel of 20 mm heated length without inlet subcooling for a mass velocity of 500 kg/m<sup>2</sup>s, yielding a CHF of 396 kW/m<sup>2</sup>.**

Then, when  $\delta$  equals  $\Delta\delta$  at the outlet of the microchannel, CHF is reached. Refer to Figure 20.11 for a simulation showing the profiles from the channel centerline to the wall. The leading constant and two exponents were determined with a database including three fluids (R-134a, R-245fa and R-113) and three circular channel diameters (0.509 mm, 0.790 mm and 3.15 mm) taken from the CHF data of Wojtan,

Revellin and Thome (2007) and Lazarek and Black (1982). Their model also satisfactorily predicted the R-113 data of Bowers and Mudawar (2004) for circular multi-microchannels with diameters of 0.510 and 2.54 mm of 10 mm length. Furthermore, taking the channel width as the characteristic dimension to use as the diameter in their 1-d model, they were also able to predict the rectangular multi-microchannel data of Qu and Mudawar (2004) for water. All together, 90% of the database was predicted within  $\pm 20\%$ . As noted above, this model also accurately predicted the R-236fa multi-microchannel data of Agostini et al. (2008c), utilizing the hydraulic diameter of the heated perimeter. Furthermore, in a yet to be published comparison, this model also predicts microchannel CHF data of liquid nitrogen and also  $\text{CO}_2$  data from three independent studies.

### 20.3.4 Hot Spot Model for CHF in Microprocessor Cooling Elements

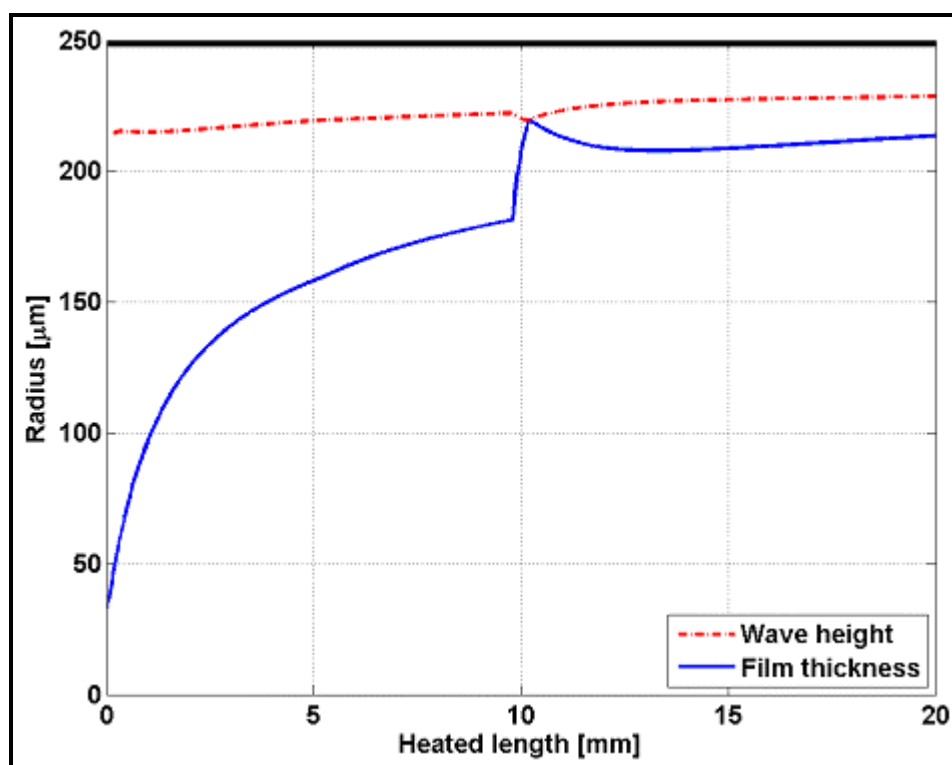


**Figure 20.12.** Revellin et al. (2008a) simulation of a hot spot of 0.4 mm length located half way along a heated channel of 20 mm length for R-134a at a saturation temperature of  $30^\circ\text{C}$  in a 0.5 mm channel without inlet subcooling for a mass velocity of  $500 \text{ kg/m}^2\text{s}$ .

Microprocessors in computers can have local heat dissipation rates that are ten times or more the die average, thus leading to the creation of “hot spots”. Similar situations can also occur in cooling of power electronics. When cooling such devices, it is interesting to know if this local hot spot will trigger the onset of CHF when applying flow boiling in the multi-microchannels to cool the chip. Implementing the mechanistic CHF model of Revellin and Thome (2008) described above, but now for a *non-uniform* heat flux boundary condition along the channel, Revellin et al. (2008a) simulated the effects of hot spots on triggering of CHF. Figure 20.12 shows the effect of a small hot spot of 0.4 mm length around the perimeter of the channel on the variation of the annular liquid film thickness with respect to the channel centerline and the liquid film wave height, and its triggering of CHF at their point of intersection. At the conditions shown, CHF at the local hot spot occurs at  $3000 \text{ kW/m}^2$  for the otherwise uniform heat flux of  $218 \text{ kW/m}^2$ . Hence, in this case, a local heat flux 13.8 times the mean value can be sustained. The value

of CHF without a hot spot (that is, with the hot spot heat flux equal to that of the rest of the channel) for these same conditions is  $396 \text{ kW/m}^2$  as noted above, and hence the hot spot value is still over 7 times that. For cooling of microprocessors and power electronics, this means that very high local hot spot heat fluxes can be sustained as long as they are not located near the exit of the flow channel. In their paper, Revellin et al. (2008a) also simulated the effects of the location, size and number of hot spots on CHF for various channel sizes, lengths and mass velocities.

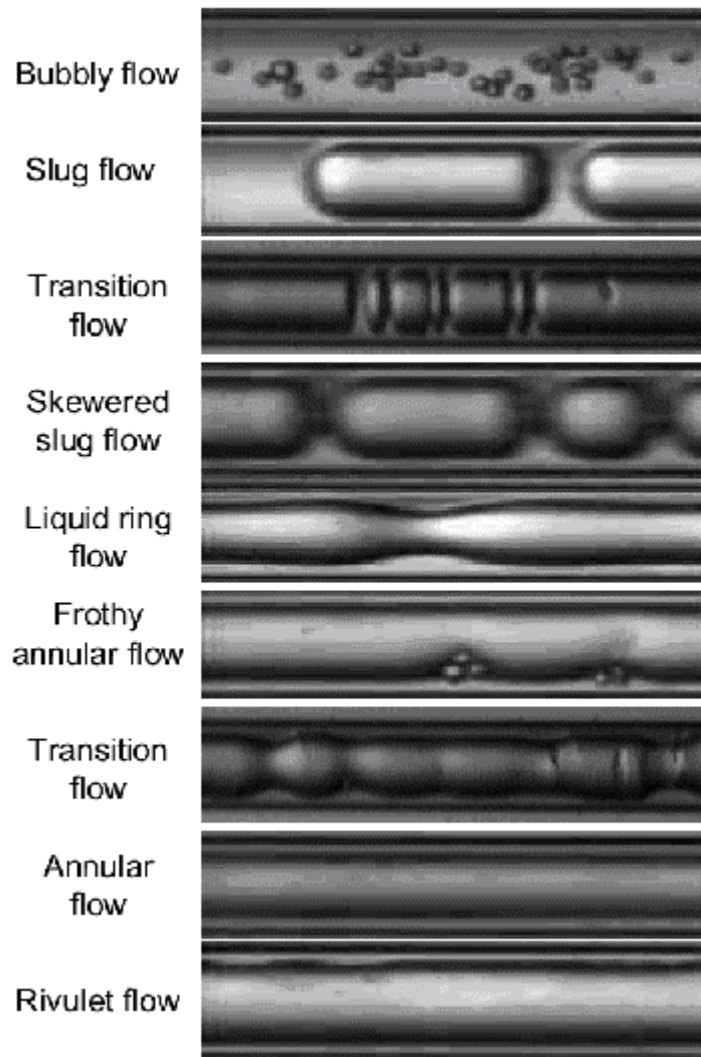
## 20.4 Two-Phase Flow Pattern Observations and Maps for Microchannels

Numerous two-phase flow pattern observations are now available. Chapter 1 of this book now contains a large number of microchannel two-phase flow and boiling videos from various sources. Apparently, the first detailed study on flow patterns in microchannels is that by Suo and Griffith (1964), who observed three different flow patterns in their study using channels of 1.03 and 1.60 mm diameter: bubbly/slug, slug and annular flow. Their study covered heptane and water as the liquid phase, and helium and nitrogen as the gas phase. Similarly, the study of Cornwell and Kew (1992) noted three different flow patterns in rectangular channels ( $1.2 \times 0.9 \text{ mm}$  and  $3.5 \times 1.1 \text{ mm}$ ) for tests with R-113 and R-141b: isolated bubbles, confined bubbles, and slug/annular flow. Many others have observed these three basic flow patterns: Damianides and Westwater (1988) for a 1 mm tube, Mertz, Wien and Groll (1996) with water and R-141b evaporating in multi-microchannels, Kasza, Didascalou and Wambsganss (1997) for a single rectangular channel of 2.5 mm by 6 mm, Lin, Kew and Cornwell (1998) using a single round tube of 2.1 mm diameter, and Sheng and Palm (2001) for 1 to 4 mm tubes.

Some authors describe microchannel two-phase flow using additional flow pattern designations, such as Triplett et al. (1999a) who used both rectangular and circular channels. As a further example, Coleman and Garimella (1999, 2000, 2003) classified their observations into a total of 16 regimes subdivided into four main traditional groups (dispersed, intermittent, wavy and annular) that were then subdivided as follows: dispersed flow into 3 types of bubbly flow, intermittent flow into 4 types of slug and plug flow, wavy flow into 4 types of waves, and annular into 5 categories of annular films. Some very good photographs of the flow regimes are shown in their papers. Yang and Shieh (2001) concluded their study on flow patterns of air-water and two-phase R-134a in small circular tubes by saying that none of the existing flow pattern maps were able to predict the air-water and refrigerant flow pattern transitions in small tubes. Hetsroni et al. (2003) performed experiments for air-water and steam-water flow in parallel triangular microchannels and emphasized the discrepancy between flow patterns of air-water and steam-water flow. In a comprehensive study of very small diameters, Serizawa and Feng (2001), Serizawa, Feng and Kawara (2002), Serizawa et al. (2002) and Serizawa (2004) documented several distinctive flow patterns using air-water and steam-water flow in circular tubes of 20, 25, 50 and 100  $\mu\text{m}$  diameter: dispersed bubbly flow, slug flow, liquid ring flow, liquid lump flow, annular flow, skew (Yakitori) flow, frothy or wispy annular flow, rivulet flow and liquid droplet flow. Notable for their absence is any reference to stratified flows, which no longer appear in small channels or at least at the flow conditions tested.

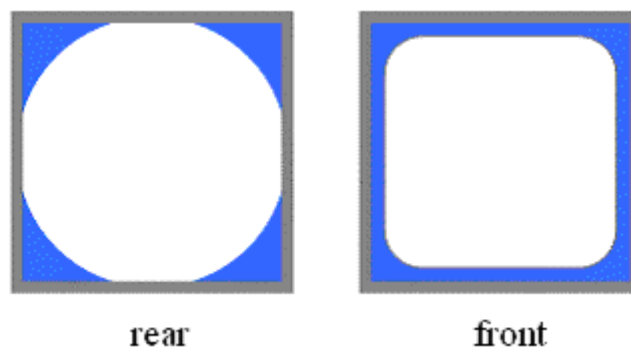
Serizawa and Feng (2001) have provided one of the most interesting insights into two-phase flow patterns and what constitutes a microchannel. Figure 20.13 depicts their flow pattern observations made for a 0.100 mm glass channel with steam-water. Here, a new flow pattern type was identified, namely *liquid ring flow*. Similarly, for air-water in a 0.020 mm channel, they again observed this liquid ring flow but furthermore identified yet another new flow pattern they named *liquid lump flow*. Hence, this is apparently the first experimental evidence to support the case that there should be a sub-microchannel two-phase channel classification for flow patterns, i.e. perhaps a *micron-scale* range.





**Figure 20.13. Flow regimes observed by Serizawa and Feng (2001) in a 0.100 mm channel for steam-water flows: (1) bubbly flow, (2) slug flow, (3) transition, (4) skewed “Yakitori” flow, (5) liquid ring flow, (6) frothy annular flow, (7) transition, (8) annular flow, (9) rivulet flow.**

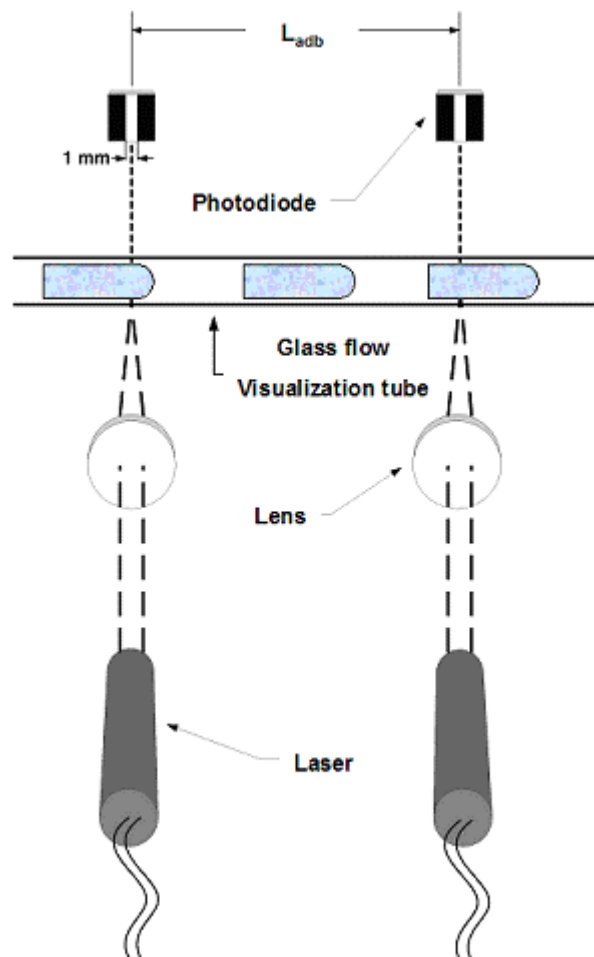
Cubaud and Ho (2004) made an interesting study and analysis for air-water flows in small square channels. Several of their liquid film profiles they observed are shown here schematically in Figure 20.14. In particular, the liquid film was continuous around the channel (right) near the nose end of elongated bubbles, while near the rear there were dry patches at the middle of each face (left). They called these wedge flows. This regime may be more likely to occur in air-water flows than others because of the large surface tension and contact angle of water.



**Figure 20.14. Wedge flow of elongated bubbles observed by Cubaud and Ho (2004) for air and water in 0.200 and 0.525 mm square channels where blue = water flow, white = air flow and grey = channel walls. Left: dry faces of the channel walls towards the rear of the bubble. Right: completely wetted perimeter near the front nose of the bubble.**

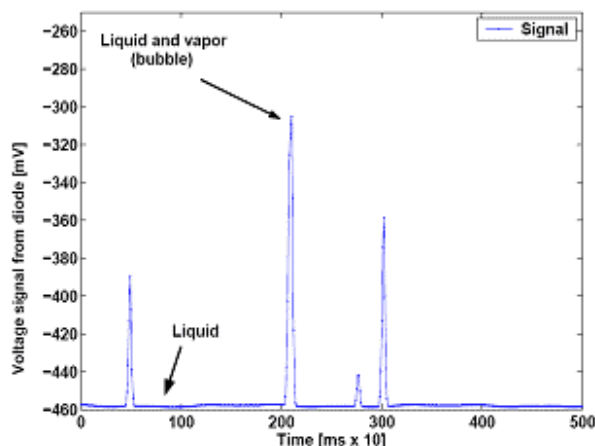
Another important aspect of two-phase flow patterns in microchannels is how to identify them, qualitatively and/or quantitatively. The difficulty of identifying flow regimes and their transitions visually comes from the difficulties in obtaining good high-speed images. Then, the interpretation of the images is subjective and the identified flow pattern can depend on the author. A better approach is to use a quantitative means to identify flow patterns, for which various techniques are available. One inexpensive optical technique is described below.

Figure 20.15 depicts the two laser / two diode optical technique developed by Revellin et al. (2006) for microchannels. The technique uses two low power lasers (less than 1 mW) and two diodes. These are mounted together with a lens to focus the laser light through the glass tube, through the fluid inside and then onto the diode (whose active surface has been reduced to get sharper light signals). Using two lasers instead of one gives two high frequency, light intensity signals, which can then be cross-correlated using signal processing to determine the velocity of bubbles, for instance. In the diagram, elongated bubbles of a slug flow in a microchannel are illustrated.

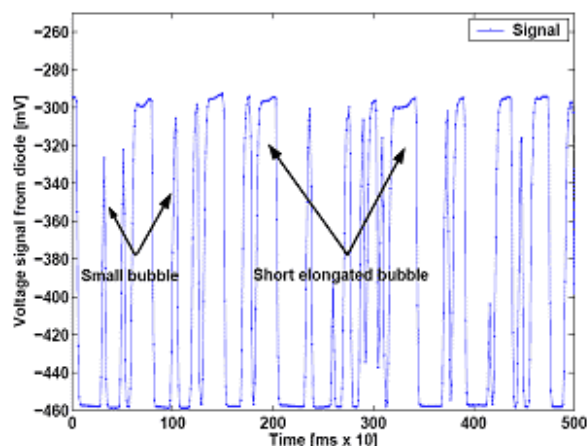


**Figure 20.15. Optical flow pattern identification technique using two lasers and diodes by Revellin et al. (2006) for a microchannel (not to scale).**

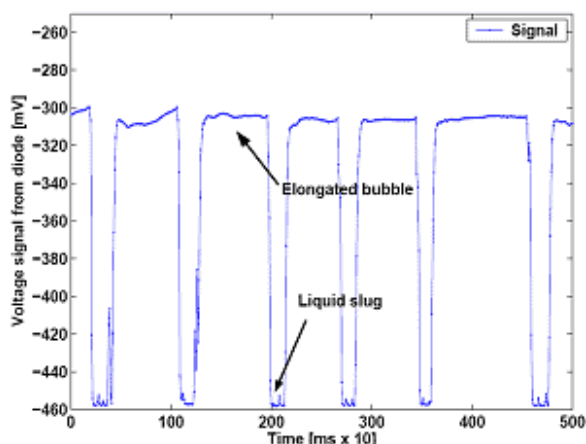
Figure 20.16 and Figure 20.17 of Revellin (2005) and Revellin et al. (2006) show the resulting laser signals for the respective flow patterns observed, actual images of selected flow patterns and schematic diagrams of the flow patterns. The plots show the intensity of light (in negative voltage) versus time for the light incident on the diode and recorded by the data acquisition system. Even without any signal processing, it is possible to identify some flow patterns only by comparing the signals to the corresponding images; however, the corresponding videos were taken separately since its light source interfered with the diode light signals. Processing the signals using the procedure described in Revellin et al. (2006), it is possible to distinguish (i) the flow pattern, (ii) the bubble frequency when they are present, (iii) bubble velocity using a cross-correlation to find the delay time between the two signals, (iv) the bubble length, and (v) indirectly the void fraction from the elongated bubble velocity.



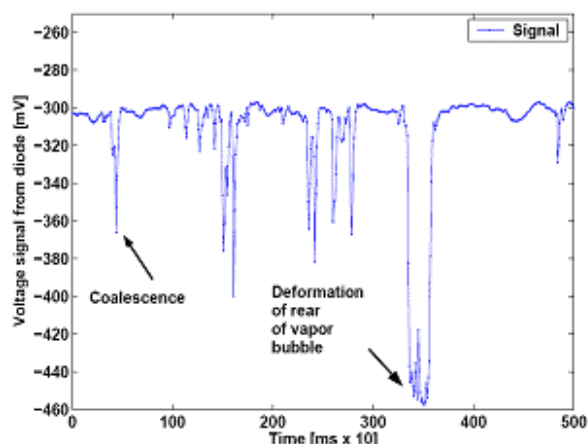
(a) Bubbly flow signal at  $x = 0.02$  and  $f_A = 131 \text{ Hz}$



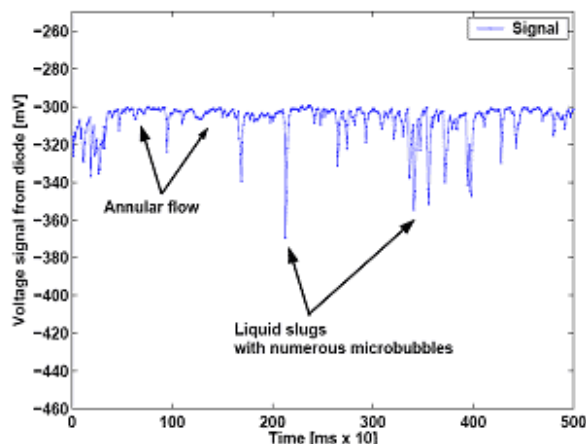
(b) Bubbly/slug flow signal for at  $x = 0.04$  and  $f_A = 520 \text{ Hz}$



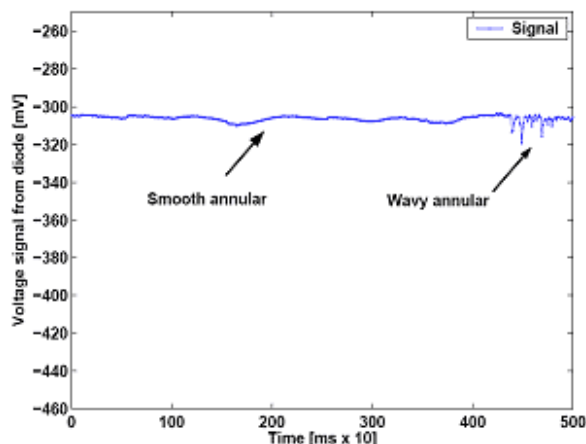
(c) Slug flow signal at  $x = 0.11$  and  $f_A = 136 \text{ Hz}$



(d) Slug/semi-annular flow signal at  $x = 0.19$  and  $f_A = 33 \text{ Hz}$



(e) Semi annular flow signal at  $x = 0.40$  and  $f_A = 0 \text{ Hz}$



(f) Annular flow signal at  $x = 0.82$  and  $f_A = 0 \text{ Hz}$

**Figure 20.16. Temporal laser light intensity signals of Revellin (2006) and Revellin et al. (2006) for R-134a in a 0.509 mm glass channel at the exit of a micro-evaporator tube at a mass velocity of  $500 \text{ kg/m}^2\text{s}$  and saturation temperature of  $30^\circ\text{C}$ . Below each image, the flow regime identified is indicated at the particular vapor quality along with the bubble frequency measured.**

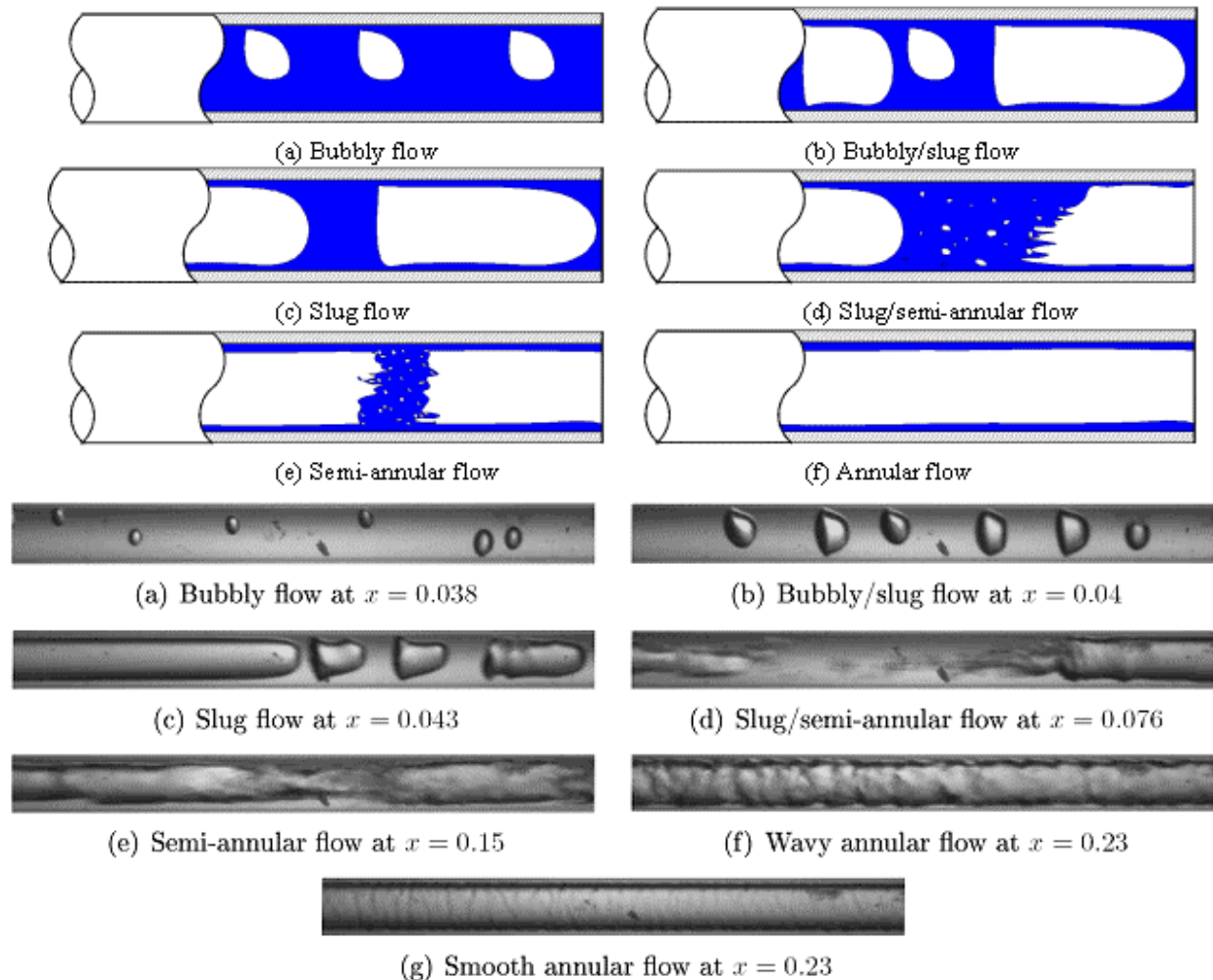


**Figure 20.17.** Flow patterns and transitions observed by Revellin (2006) for R-245fa in a 0.509 mm glass channel at the exit of a micro-evaporator tube at a mass velocity of 500 kg/m<sup>2</sup>s and saturation temperature of 35°C. *Top:* schematic diagrams of observed flows. *Bottom:* images show actual flows.

Various two-phase flow pattern maps have been proposed for microchannels over the years. The first such map was that of Suo and Griffith (1964), who proposed some simple correlations for transition boundaries based on their observations using channels of 1.03 and 1.60 mm diameter to divide the flows into bubbly/slug, slug and annular flow regimes. Their study covered heptane and water as the liquid phase and helium and nitrogen as the gas phase.

Triplett et al. (1999a) proposed a graphical map in terms of the superficial liquid velocity versus the superficial vapor velocity as shown in Figure 20.18, based on their flow pattern observations for air-water in a 1.1 mm horizontal glass channel (that is, essentially drawing in boundaries on the map). The flows were made using a mixer for the air and water upstream of the observation point. They also made observations in a 1.45 mm channel and in several small semi-triangular test sections using a strobe and digital camera for their observations. Also plotted on the map are the experimentally determined flow transitions for R-134a of Revellin et al. (2006) taken with the above described quantitative flow pattern detection technique. These illustrate a significant difference in the transition locations, caused by the large difference in physical properties of air-water compared to R-134a. Hence, this points to the need of flow



pattern transition prediction methods that incorporate the properties of the gas and liquid phases in order to generalize the map to work for other than the original fluid(s).

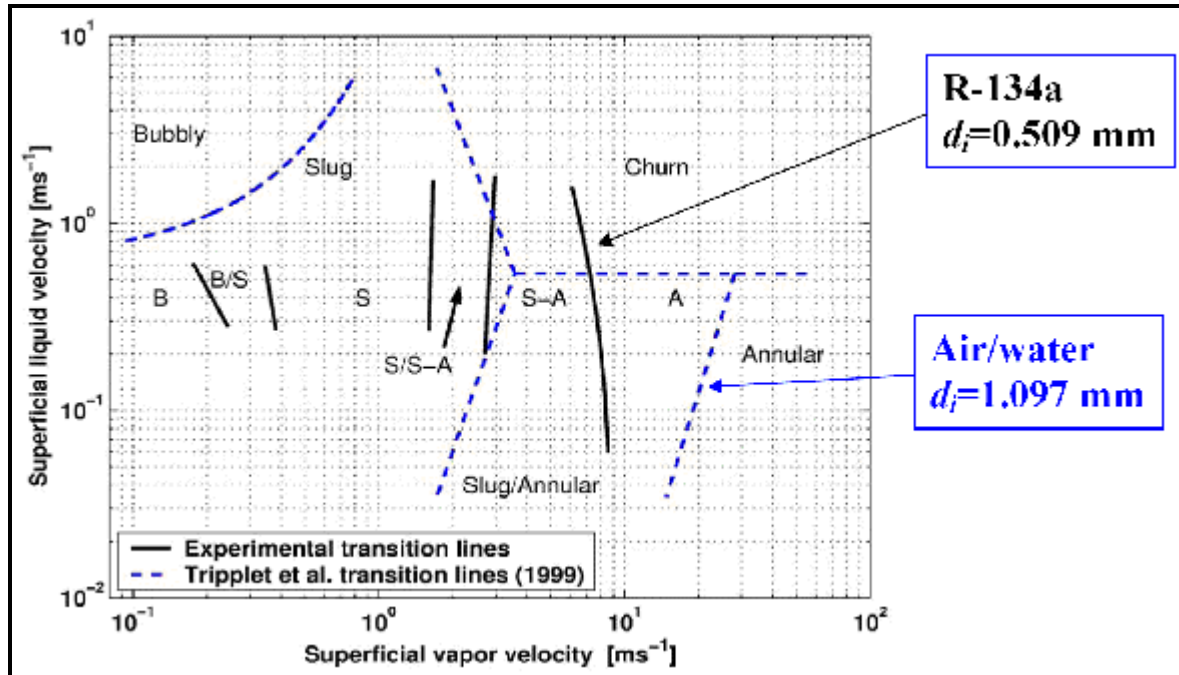


**Figure 20.18. Flow pattern map of Triplett et al. (1999a) for air-water in a 1.1 mm horizontal channel showing their experimentally determined transition boundaries and plotted the experimental transition lines from Revellin et al. (2006) for R-134a flow pattern observations.**

Coleman and Garimella (1999) and Garimella, Killion and Coleman (2002) have also proposed graphical flow pattern maps based on their extensive observations of air-water flows and R-134a condensing flows in circular and non-circular channels. They have also proposed empirical expressions for some of the transitions. Yang and Shieh (2001) also proposed a flow pattern map of superficial liquid velocity versus superficial vapor velocity basis on their observations made in a 2.0 mm channel, noting that the transition lines were quite different for air-water flows compared to R-134a flows.

Akbar, Plummer and Ghiaasiaan (2003) proposed a flow pattern map based on all available air-water observations in circular and near-circular channels with hydraulic diameters less than or equal to 1.0 mm. Their transition boundaries are as follows for their log-log map plotted as  $We_{SG}$  versus  $We_{SL}$ . For their surface tension dominated zone (comprised of bubbly, plug and slug flows), its upper threshold boundary is determined in terms of the liquid and vapor superficial Weber numbers, which were defined earlier in Section 20.2:

$$We_{SG} \leq 0.11We_{SL}^{0.315} \quad (\text{for } We_{SL} \leq 3.0) \quad [20.4.1a]$$

$$We_{SG} \leq 1.0 \quad (\text{for } We_{SL} > 3.0) \quad [20.4.1b]$$

Thus, at all conditions for which  $We_{SG}$  is below this boundary, the flow is in the surface tension dominated zone. The first inertia dominated zone (annular flow zone) is bounded by the following transition threshold:

$$We_{SG} \geq 11.0We_{SL}^{0.14} \quad (\text{and } We_{SL} \leq 3.0) \quad [20.4.1c]$$

Thus, at all conditions above and to the left of this boundary, the flow is in the annular flow zone. The second inertia dominated zone (dispersed flow zone or froth) is bounded by the following transition threshold:

$$We_{SL} > 3.0 \quad (\text{and } We_{SG} > 1.0) \quad [20.4.1d]$$

Therefore, at all conditions above and to the right of this boundary, the flow is in the dispersed flow zone. The transition zone falls below the annular zone and above the surface tension dominated zone as follows:

$$0.11We_{SL}^{0.315} < We_{SG} < 11.0We_{SL}^{0.14} \quad (\text{and } We_{SL} \leq 3.0) \quad [20.4.1e]$$

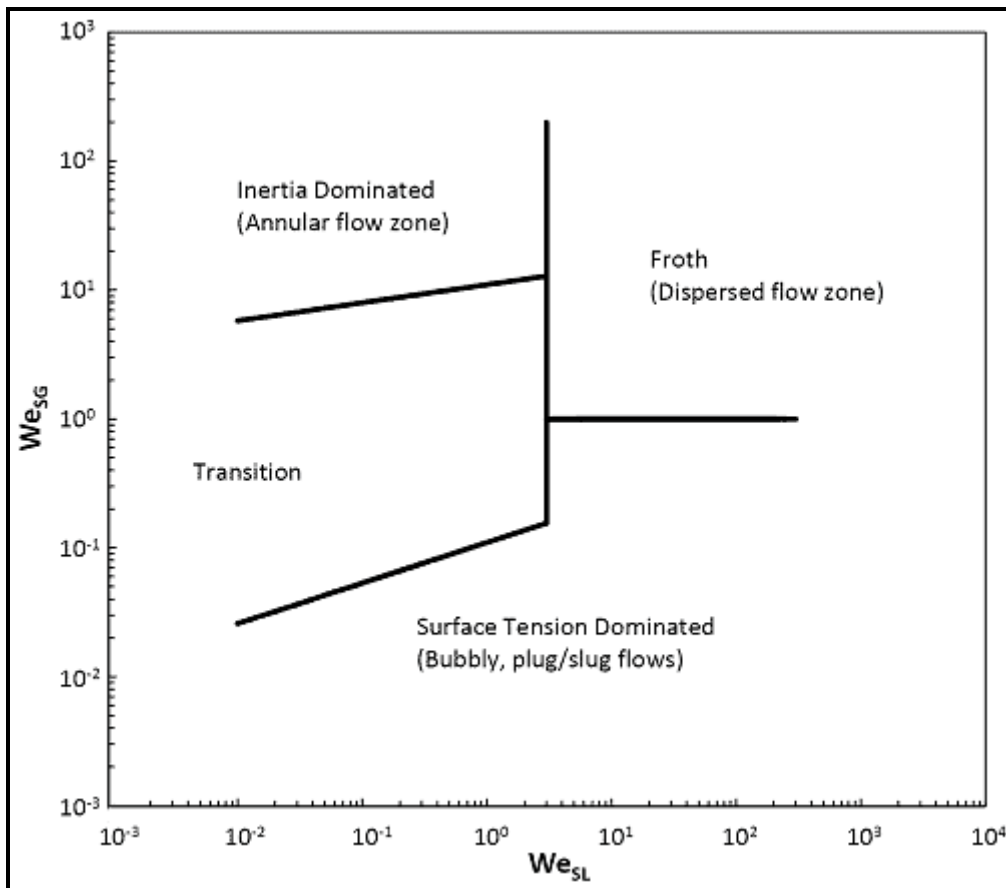


**Figure 20.19. Flow pattern map of Akbar, Plummer and Ghiaasiaan (2003).**

Figure 20.19 shows a diagram of this flow pattern map. According to Chen, Tian and Karayiannis (2006), this map worked very well for air-water in channels close to 1 mm in diameter for flow pattern observations taken in four independent studies. Furthermore, based on their analysis, the superficial vapor and liquid Weber numbers work better for distinguishing flow pattern transitions than the tradition superficial vapor and liquid velocities in microchannels. However, they found that the map of Akbar, Plummer and Ghiaasiaan (2003) did not predict their flow pattern observations for R-134a in vertical small diameter tubes (1.10, 2.01, 2.88 and 4.26 mm) very well, perhaps, as they noted, because the map is

suggested for use only when the Bond number is less than 0.3, which corresponds to a channel diameter of about 0.25 mm at 6 bar for R-134a.

Ullmann and Brauner (2007) have recently proposed a microscale flow pattern map based on analysis of the mechanisms controlling each flow pattern transition. They used the flow pattern observations of Triplett et al. (1999a) for air-water in a 1.1 mm, horizontal glass channel as their experimental database. Significant modifications were made to well-known macroscale transition theories, i.e. Taitel and Dukler (1976) and Barnea and Taitel (1986), to make them work for this small channel. Afterwards, they were able to reliably predict these transitions using their new methods for each transition. Furthermore, they noted that the stratified flow region shrinks to a very small zone on their map at relatively very low liquid flow rates and very high gas flow rates. Interestingly, they pointed out that their analysis showed that the difference between a stratified flow whose interface is curved up to the top of the channel by capillary forces and an annular flow becomes ambiguous in small channels since both regimes then look essentially the same, and such a flow could still be classified as an annular flow.

Revellin and Thome (2007a) have utilized flow pattern data, bubble frequency data and the CHF correlation of Wojtan, Revellin and Thome (2007) to produce a new type of flow pattern map for diabatic (evaporating) flows. Their map classifies these evaporating flow regimes as follows:

- *Isolated bubble regime*: this refers to bubbly flow (defined as having bubbles shorter in length than the channel diameter), slug flow (defined as bubbles longer than the channel diameter) and mixed bubble flows displaying both long and short bubbles and where the frequency of bubbles increases with increasing heat flux and thus vapor quality at a fixed mass velocity;
- *Coalescing bubble regime*: this refers to slug flows and churn flows (the latter are long bubbles followed by aerated liquid slugs) but where some short bubbles may still exist, where the frequency of the bubbles decreases with increasing heat flux and thus vapor quality at a fixed mass velocity;
- *Annular flow regime*: this refers to both smooth annular flows with nearly no interfacial waves and wavy annular flow where interfacial waves are very evident;
- *Dryout regime*: this refers to the post-dryout region after passing through CHF at the critical vapor quality.

Figure 20.20 shows an example of some bubble frequency data obtained in a 0.5 mm diameter sight glass at the exit of a 0.5 mm diameter micro-evaporator tube, detected using the laser/diode measurement technique described earlier by Revellin et al. (2006). At a fixed mass velocity, the bubble frequency is seen to increase rapidly up to a peak with increasing heat flux and hence increasing exit vapor quality at which the observations are made in the sight glass (and where the flow is comprised of short and long bubbles with respect to the channel diameter). After the peak, the frequency falls first very sharply and then less sharply all the way to a bubble frequency of zero. The first sharp fall off involves the coalescence of all the smaller bubbles into long bubbles, and the slower fall off then is from coalescence of the long bubbles into even longer and thus fewer bubbles, until annular flow is reached. The change in trend during the fall off in frequency has been identified from the data processing to coincide with the disappearance of the last short bubbles.

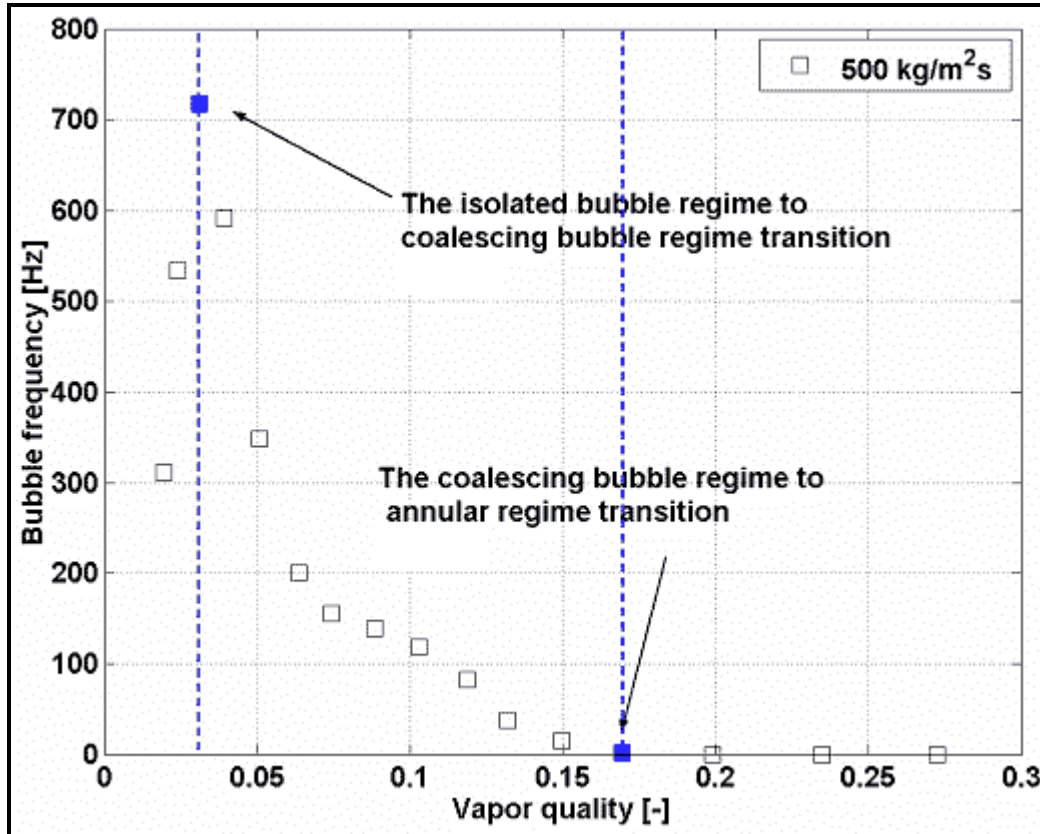


**Figure 20.20. Bubble frequency data measured by Revellin et al. (2006) for R-134a at the outlet of a 0.509 mm microchannel using their laser technique, indicating where the bubble frequency reaches its maximum value and where it becomes zero.**

For the development of mechanistic models to predict local flow boiling heat transfer coefficients and two-phase frictional pressure drops, significant information about the flow regime and its structure is required. For example, for modeling flow boiling in the slug flow regime in a microchannel, this requires knowledge of the bubble frequency, bubble length, liquid slug length, thickness of the liquid film trapped between the bubble and the wall, etc., e.g. the Thome, Dupont and Jacobi (2004) three-zone model that will be described later in this chapter. Thus, this justifies the creation of a flow pattern map that reflects these requirements. Hence, in partial response to this, Revellin and Thome (2007a) have proposed a new type of flow pattern map that classifies flows as isolated bubble (IB) flow (that is, flows at vapor qualities before the peak in bubble frequency), coalescing bubble (CB) flow, annular (A) flow and dryout (DO) flows. Figure 20.21 shows a simulation of their diabatic flow pattern map for R-134a where the transitions are predicted as described below.

To predict the local peak in bubble frequency at the IB/CB transition, different combinations of non-dimensional numbers were examined but in the end only the Boiling number  $Bo$ , the liquid Reynolds number  $Re_L$  and the vapor Weber number  $We_G$  were found to have a significant influence on the location of this peak. Using a least square method to determine the empirical coefficients, the resulting correlation predicts the transition location  $x_{IB/CB}$  as:

$$x_{IB/CB} = 0.763 \left( \frac{Re_L Bo}{We_G} \right)^{0.41} = 0.763 \left( \frac{q \rho_G \sigma}{\mu_L h_{LG} \dot{m}^2} \right)^{0.41} \quad [20.4.2]$$

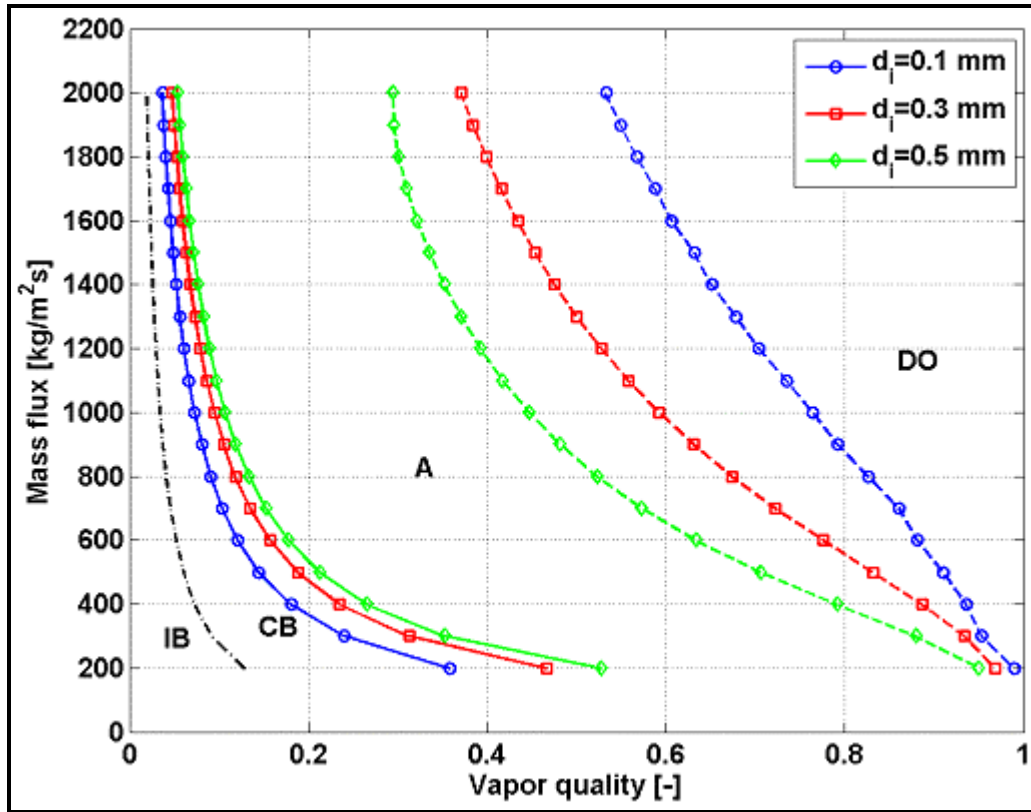


Figure 20.21. Diabatic flow pattern map of Revellin and Thome (2007a) simulated for R-134a at 30°C for three channel sizes in a horizontal uniformly heated channel ( $q = 60 \text{ kW/m}^2$  without inlet subcooling and simulated for a channel length of 20 mm) showing the theoretical CHF model transitions from annular flow to dryout (IB: isolated bubble regime; CB: coalescing bubble regime; A: annular flow regime; DO: dry out regime).

As can be seen, this boundary is *not* a function of channel diameter  $d_i$ , probably because of the limited range of channel diameters used in their tests (0.509 and 0.790 mm) but is a function of heat flux. The liquid Reynolds number, the Boiling number and the vapor Weber number are defined as:

$$\text{Re}_L = \frac{\dot{m} d_i}{\mu_L} \quad [20.4.3]$$

$$\text{Bo} = \frac{q}{\dot{m} h_{LG}} \quad [20.4.4]$$

$$\text{We}_G = \frac{\dot{m}^2 d_i}{\sigma \rho_G} \quad [20.4.5]$$

Thus, once the fluid is chosen together with its saturation temperature and the imposed heat flux, the entire transition curve depends only inversely on the mass velocity. In fact, the diameter cancels out in the bracketed term of the three dimensionless numbers and this transition is thus independent of tube



diameter. On the other hand, the location of  $x_{IB/CB}$  is directly dependent on the heat flux and thus this boundary moves to the right on the map with increasing heat flux. Physically speaking, this is expected as the bubble nucleation rate is dependent on the heat flux and this thus creates a higher bubble frequency. Comparing this transition to an *adiabatic* flow pattern map with bubbly flow and slug flow designations, the present boundary  $x_{IB/CB}$  is approximately equivalent to an *adiabatic* map's transition between bubbly flow and slug flow, i.e. where one regime becomes dominant over the other in such a map. Since  $x_{IB/CB} \sim q^{0.41}$ , the present *diabatic* map demonstrates quite explicitly that this boundary is a function of heat flux in an evaporating flow, hence illustrating the importance of using a *diabatic* map for modeling this transition in evaporating flows rather than extrapolating an *adiabatic* map to determine this boundary.

The  $x_{CB/A}$  transition is the vapor quality at which the bubble frequency reaches zero, i.e. it is the end of the presence of liquid slugs and distinct vapor bubbles. Only the liquid Reynolds number  $Re_L$  and the liquid Weber number  $We_L$  were found to have an influence on this transition from a parametric study, but *not* the heat flux. The resulting  $x_{CB/A}$  transition correlation is:

$$x_{CB/A} = 0.00014 Re_L^{1.47} We_L^{-1.23} \quad [20.4.6]$$

The liquid Weber number  $We_L$  is defined as:

$$We_L = \frac{\dot{m}^2 d_i}{\sigma \rho_L} \quad [20.4.7]$$

Thus, again for a chosen fluid at a predetermined saturation temperature and diameter, the entire transition curve is made by varying the mass velocity input into these expressions. As can be seen in the simulation for R-134a, this transition moves to lower vapor qualities as the diameter is decreased. Since  $x_{IB/CB}$  is not a function of  $q$ , one can expect that this transition boundary can also be predicted using methods proposed for it in *adiabatic* flow pattern maps, such as that of Ullmann and Brauner (2007).

To complete the model, the A/DO transition from annular flow to dryout is obtained using the CHF correlation [20.3.10] of Wojtan, Revellin and Thome (2007) and the expression for the critical vapor quality [20.3.11]. Assuming no inlet subcooling, combining these two expressions and solving for  $x_{crit}$  gives:

$$x_{crit} = 1.748 \left( \frac{\rho_G}{\rho_L} \right)^{0.073} \left( \frac{\rho_L^{0.24} \sigma^{0.24}}{\dot{m}^{0.48}} \right) \left( \frac{1}{d_i^{0.28}} \right) L_h^{0.04} \quad [20.4.8]$$

This expression is a function of physical properties, the mass velocity and the channel diameter whilst only a very weak function of the heated length, but *not* a function of the imposed heat flux  $q$ . Hence, to simulate the map, one assumes values for the physical properties, mass velocity, channel diameter, heat flux and heated length (and subcooling as necessary) of the channel being simulated. Then, the value of  $x_{crit}$  is calculated. From an energy balance along the channel that gives the variation of  $x$  along the length  $L_h$ , one locates the position of  $x_{crit}$ . Repeating this calculation for different values of mass velocity, one generates the A/DO transition curve on the map that corresponds to the location of the onset of the critical heat flux. It is true that the above expression is a slight function of  $L_h$ , but only to the 0.04 power. This has a negligible effect on the calculation of say a 0.020 m length compared to a 0.010 m length (less than 3% when doubling the value of  $L_h$ ). As can be seen in the simulation for R-134a, this A/DO transition moves to lower vapor qualities as the mass velocity is increased. Furthermore, this transition moves to higher vapor qualities as the channel diameter is decreased.

As an example, consider the following conditions for R-134a at a mass velocity of  $500 \text{ kg/m}^2\text{s}$ :  $d_i = 0.0005 \text{ m}$ ,  $L_h = 0.020 \text{ m}$ ,  $p_{\text{sat}} = 7.7 \text{ bar}$  (for  $T_{\text{sat}} = 30^\circ\text{C}$ ), no subcooling at the inlet, and  $q = 180000 \text{ W/m}^2$ . For these conditions:  $x_{\text{IB/CB}} = 0.10$ ,  $x_{\text{CB/A}} = 0.21$ ,  $x_{\text{crit}} = 0.93$ , and  $x_{\text{outlet}} = 0.33$  from an energy balance. Hence, at these conditions the critical vapor quality (and critical heat flux) will not be reached before the end of the channel. Now, if the heat flux is increased to  $q = 540000 \text{ W/m}^2$ , then for these conditions:  $x_{\text{IB/CB}} = 0.15$ ,  $x_{\text{CB/A}} = 0.21$ ,  $x_{\text{crit}} = 0.93$ , and  $x_{\text{outlet}} = 0.99$  from an energy balance and in this case critical conditions will be reached before the end of the channel.

Their database for development of this map covered two fluids (R-134a and R-245fa), two diameters (0.509 and 0.790 mm), various micro-evaporator heated lengths (20-70 mm), mass velocities from 210-2094  $\text{kg/m}^2\text{s}$  (always at the stable flow conditions), uniform heat fluxes from 3.1-597  $\text{kW/m}^2$  in their micro-evaporator and saturation temperatures from 26-35°C (saturation pressures from 2.1-8.9 bar). The ranges covered by the dimensionless numbers were as follows:  $0.00003 \leq \text{Bo} \leq 0.00632$ ,  $640 \leq \text{Re}_L \leq 8855$ ,  $125 \leq \text{We}_G \leq 12525$  and  $4 \leq \text{We}_L \leq 34970$ . Bubble frequencies as high as 928 bubbles/second were observed in their database. It should be noted that they used a valve before the micro-evaporator test section to stabilize the flow; thus, these observations are all for stable flows without oscillations. As an alternative, the A/DO boundary in this map can also be predicted using the Revellin and Thome (2008) mechanistic model for predicting critical heat flux in microchannels, which was presented earlier in Section 20.3.

It is important to point out that there are *two* paths from annular flow into the dryout regime: one is by surpassing CHF and another is by complete entrainment of the annular liquid film by the shear of the vapor core. The first path tends to be reached first at high heat fluxes while the second path tends to be reached first at low heat fluxes or for adiabatic flows. In the above described map, only the CHF path is included so far. For the second path, the map of Ullmann and Brauner (2006) is recommended for determining this transition in microchannels.

This diabatic flow pattern map has been further advanced by a mechanistic approach proposed by Revellin, Agostini and Thome (2008) using an elongated bubble velocity model proposed in the first part of their study by Agostini, Revellin and Thome (2008). Their elongated bubble velocity model is described in Section 20.5 of the present chapter, which predicts that elongated bubbles travel faster as their lengths increase, as was found experimentally. Furthermore, their study found that the distribution of the lengths of elongated bubbles followed a log-normal distribution when measuring bubble lengths from videos at a fixed test condition. To implement their diabatic bubble coalescence model, they assumed: (i) an initial average bubble length, (ii) that the bubble lengths vary as a log-normal distribution, (iii) a value for the initial variance in the bubble length distribution and (iv) that the bubbles coalesce upon touching one another. The initial average bubble length and the initial variance were both set equal to  $0.2d_i$ . Then, accounting for the difference in bubble velocities of different lengths, the increase in bubble length due to the vaporization process, the increase of bubble velocity due to the acceleration of the flow, the decrease in liquid slug length as its liquid is consumed by the evaporation process, the increase in bubble length from collisions and so forth, their model predicts the bubble frequency and mean bubble length as a function of vapor quality in a micro-evaporator. In fact, the model not only predicts the experimental bubble frequencies but also yields the locations of the transitions  $x_{\text{IB/CB}}$  (the peak in the frequency) and  $x_{\text{IB/CB}}$  (zero frequency) as shown in Figure 20.22 in a comparison to one of their numerous data sets. Hence, their mechanistic flow pattern map based on modeling of bubble velocities and bubble collisions provides a diabatic flow pattern map, to which  $x_{\text{crit}}$  can be added for the A/DO boundary, and that also yields bubble frequencies and bubble lengths. Thus, this model can potentially be used for the future development of physically based heat transfer or pressure drop models for microchannels. The reader is referred to their two-part paper for further details.

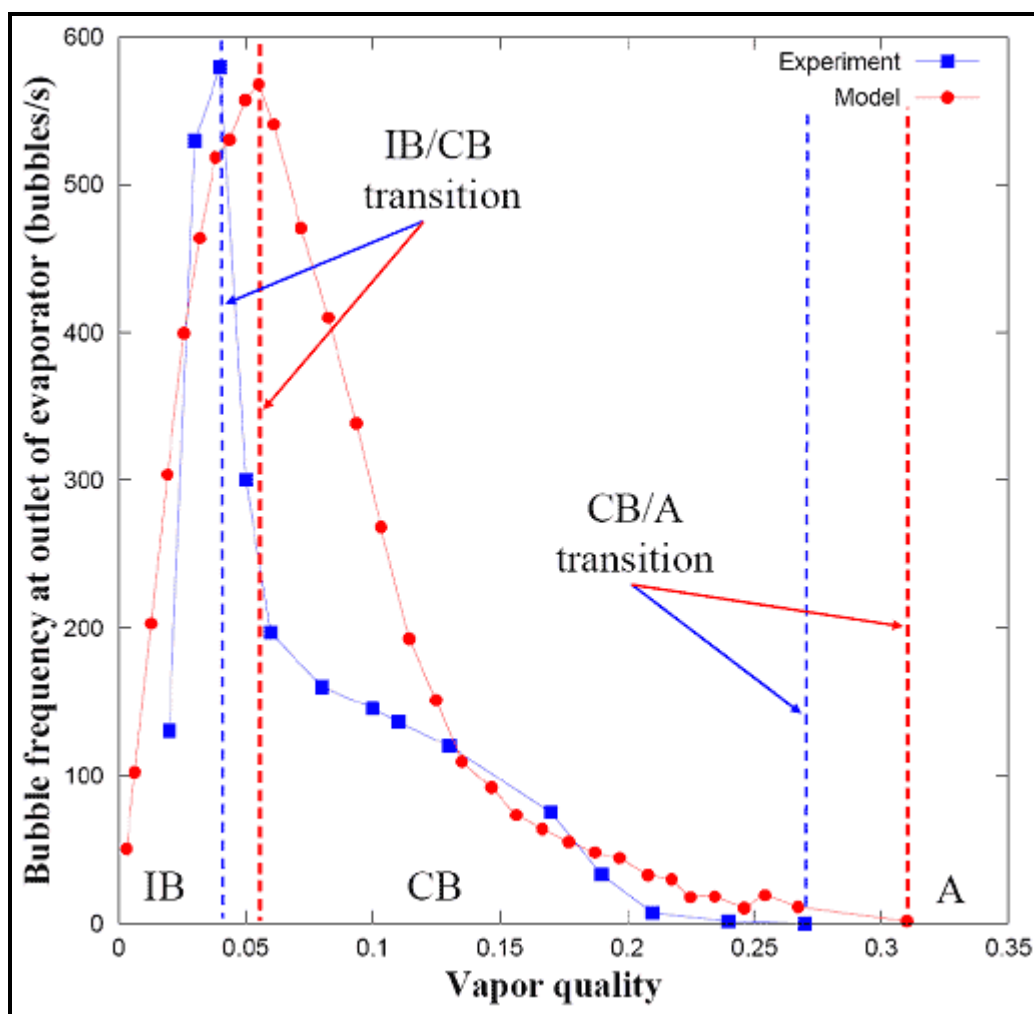


Figure 20.22. Bubble frequencies versus vapor quality predicted using the Revellin, Agostini and Thome (2008) bubble coalescence model, compared to data for R-134a at an outlet saturation temperature of 30°C in 0.509 mm channel heated over a length of 70.7 mm for a mass velocity of 500 kg/m<sup>2</sup>s.

## 20.5 Void Fraction and Bubble Dynamics in Microchannels

Void fraction is one of the most important parameters used in characterizing and modeling of two-phase flow and its value in microchannels is quite challenging to measure. Most measurements so far have been obtained via image processing of high speed, high definition photographs and videos, albeit with various simplifications and assumptions.

One of the first studies to measure void fractions in microchannels was that of Triplett et al. (1999b), who made measurements using air and water in circular glass channels of 1.1 and 1.45 mm diameter. In their tests, they varied the superficial gas and liquid velocities from about 0.02 to 80 m/s and 0.02 to 8 m/s, respectively. The void fractions were obtained from image processing of one or more photographs of a 6 mm long section of the channel for each test condition. They processed their images as follows: (i) bubbly flow: individual bubbles were assumed to be spheres or ellipsoids, (ii) slug flow: the long bubbles were divided into cylinders and spherical segments, (iii) annular flow: the vapor core was divided into several

cylinders to find the average situation, (iv) slug-annular: these were not analyzed because of the difficulty in accurately processing these images, and (v) churn flow: a void fraction of 0.5 was assumed for the dispersed gas segments in the images. Figure 20.23 shows their void fraction data plotted versus the volumetric quality  $\beta$ , which is defined as follows:

$$\beta = \frac{\dot{Q}_G}{\dot{Q}_G + \dot{Q}_L} \quad [20.5.1]$$

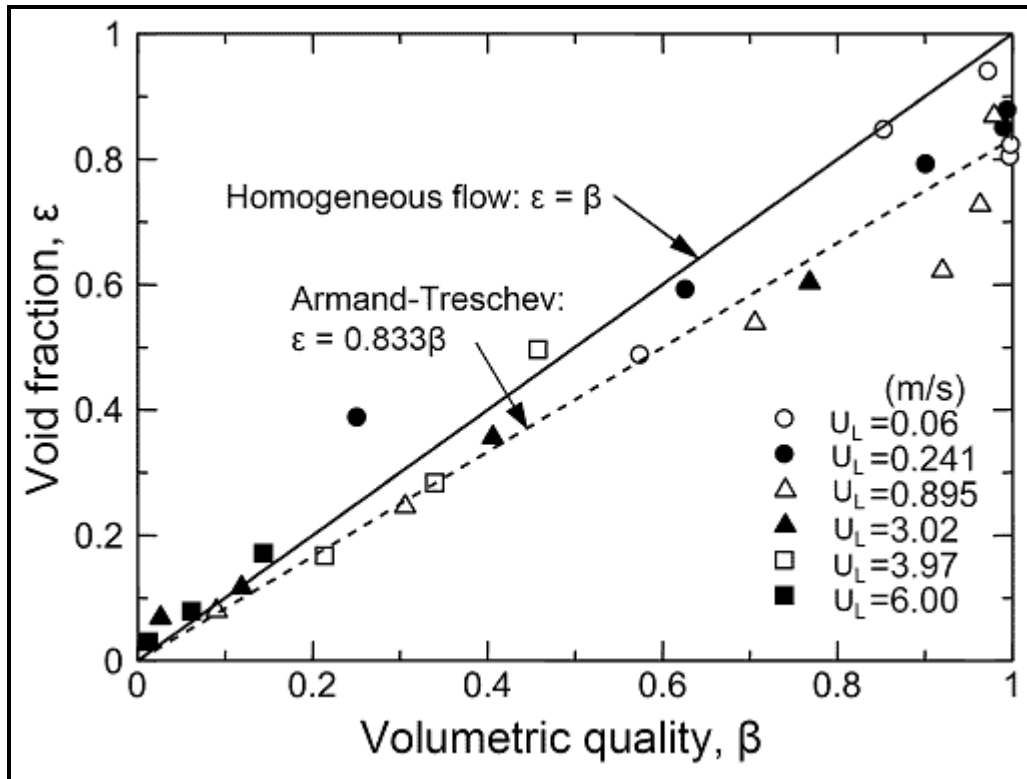


**Figure 20.23. Void fraction data of Triplett et al. (1999b) for a 1.1 mm channel compared to the homogeneous model and the Armand and Treschev (1946) correlation.**

The comparison is made versus the homogeneous model, for which  $\varepsilon = \beta$ , and the correlation of Armand and Treschev (1946), which is given as:

$$\varepsilon = 0.833\beta \quad [20.5.2]$$

At these conditions, the correlation works reasonably well except at large values where void fraction should go to its natural limit of 1.0 but instead goes to a limiting value of 0.833. It can be seen that the experimental results also do not correctly go to the limit of 1.0, probably because of the inaccuracies introduced by the image processing of very thin annular films.

Serizawa, Feng and Kawara (2002) made a detailed flow visualization study of two-phase flows in circular microchannels of 0.020, 0.025 and 0.100 mm diameter using air/water and 0.050 mm diameter for steam/water. Their void fraction data were obtained from high speed video images, assuming symmetrical shapes of bubbles, liquid slugs, etc. Their 0.020 mm channel data are shown in Figure 20.24

compared to the correlation of Armand and Treschev (1946). Comparing these data to the homogeneous model, this latter model was found to work better.

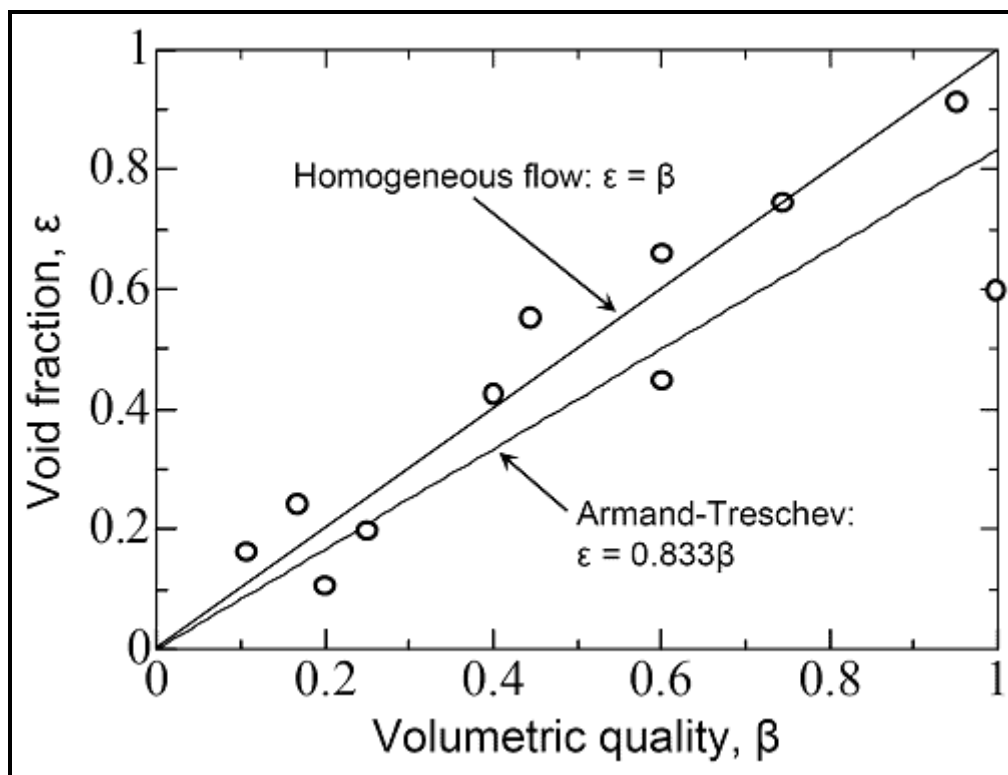


**Figure 20.24. Void fraction data of Serizawa, Feng and Kawara (2002) for a 0.020 mm channel compared to homogeneous model and Armand and Treschev (1946) correlation.**

Chung and Kawaji (2004) measured void fractions for nitrogen gas/water mixtures flowing in circular channels of 0.050, 0.100, 0.250 and 0.530 mm diameter. They proposed a simple empirical correlation, based on the volumetric quality, to describe their data:

$$\epsilon = \frac{C_1 \beta^{0.5}}{1 - C_2 \beta^{0.5}} \quad [20.5.3]$$

The empirical constants are as follows for the two smaller channels:  $C_1 = 0.03$  and  $C_2 = 0.97$  for their 0.100 mm channel and  $C_1 = 0.02$  and  $C_2 = 0.98$  for their 0.050 mm channel. A void fraction correlation for two-phase flows in narrow channels by Ali, Sadatomi and Kawaji (1993) was also compared to their two larger channels' data:

$$\epsilon = 0.8\beta \quad [20.5.4]$$

Figure 20.25 shows a comparison of their data to the homogeneous model, the empirical expression of Ali, Sadatomi and Kawaji (1993) and their new correlation. In the lower right diagram, both versions of their correlation are shown to illustrate the need for the second set of empirical constants for the smallest channel. For the largest channel, the homogeneous model is seen to work the best, although the data are surprising above the homogeneous void fraction which means that the slip ratio must be slightly less than



1.0 (this may have come from inaccuracies in the image processing). For the 0.250 mm channel, the Ali, Sadatomi and Kawaji (1993) correlation gives satisfactory results but tends to under predict the data; visually, a constant of 0.9 would seem to work better. For the two smallest channels, a huge deviation from the homogeneous model is evident. However, this is in sharp contrast to the data of Serizawa, Feng and Kawara (2002) described earlier for a 0.020 mm channel. Serizawa (2004) ascribed these large differences between his 0.020 mm data and these 0.025 mm data to the different flow patterns observed in each study, his with mostly bubbly and slug flow data while the latter are mostly annular flow data. On the other hand, if the discrepancy is related to the flow pattern, then it would be expected that the void fraction data for the 0.100 and 0.050 mm channels at low volumetric qualities would be close to the homogeneous values while in fact they are not. Hence, more analysis is required to explain and understand these contrasting experimental trends.

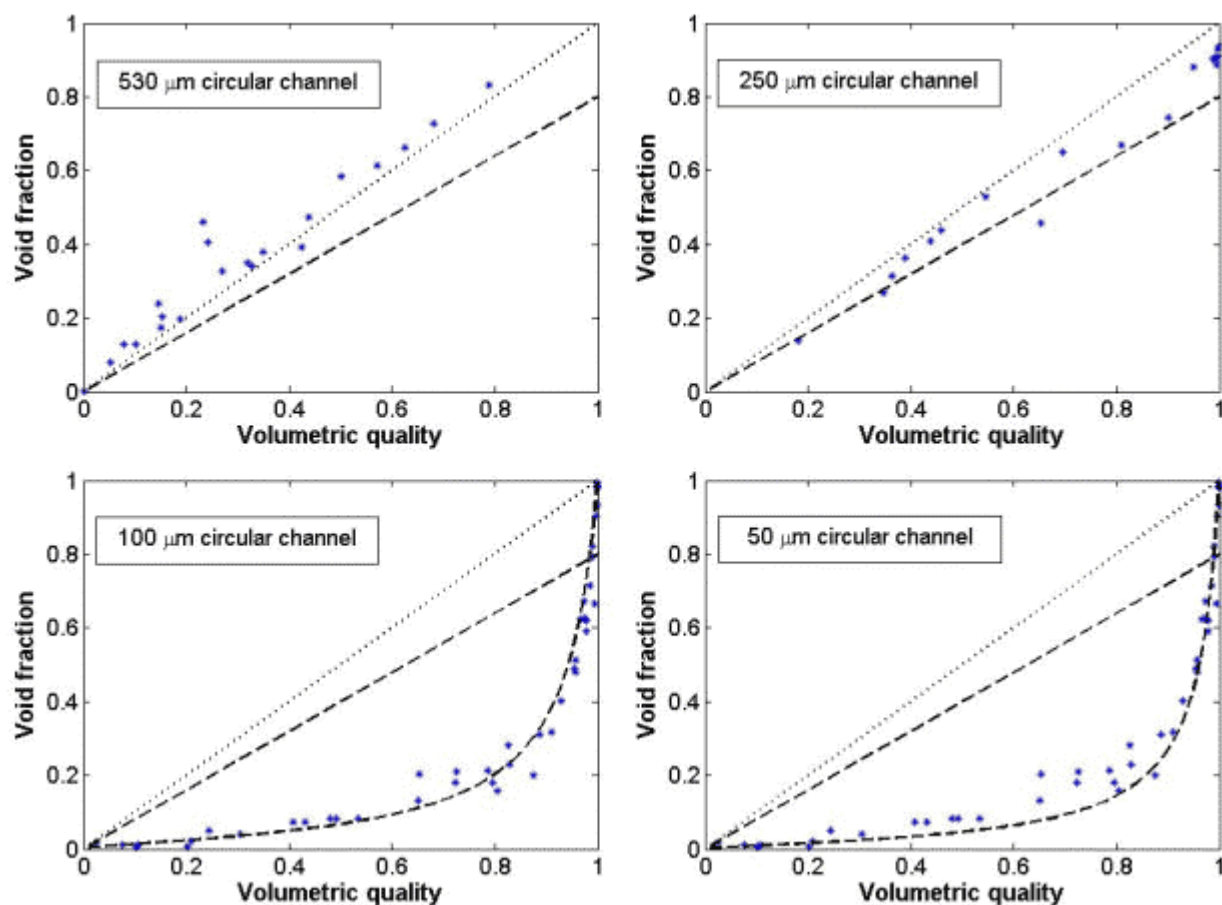


**Figure 20.25. Void fraction data of Chung and Kawaji (2004) for four channel sizes compared to the homogeneous model, the Ali, Sadatomi and Kawaji (1993) correlation and their new correlation for very small channels.**

Kawaji and Chung (2003) have also noted that the inlet geometry and channel size can produce either of the following two types of adiabatic two-phase flows in microscale channels:

- Quasi-homogeneous flow with alternating short gas and liquid plugs/slugs;
- Quasi-separated flow with alternating flows of a long gas core with a thin liquid film trapped between the gas and channel wall and a long liquid slug that moves slowly.

The former flow results in time average void fractions obeying the Armand and Treschev (1946) void fraction correlation, whilst the latter obeys the above void fraction correlation proposed by Chung and Kawaji (2004). With respect to inlet mixers, according to Kawaji (2007), a reducer inlet tends to produce the quasi-separated flow while a T-junction inlet tends to produce the quasi-homogeneous flow. However, even with a T-junction inlet, if the ratio of the T-junction diameter to the microchannel diameter is more than 2 or 3, a quasi-separated flow tends to result. Furthermore, even if the T-junction has the same diameter as the microchannel, a quasi-separated flow tends to result if the inlet gas volume upstream of the T-junction is large enough to have a compressible gas effect. A large inlet gas volume can cause intermittent injection of gas into the microchannel rather than steady flow. Kawaji believes the inlet geometry effect has not been given sufficient attention as an important factor impacting flow pattern; however, according to him it is a critical factor in determining the type of adiabatic two-phase flow in microchannels.

Kawahara et al. (2005) undertook an extensive set of tests to obtain void fraction data for the following gas/liquid combinations: nitrogen/water, nitrogen/water-ethanol mixtures and nitrogen/ethanol. They ran tests on channel diameters ranging from 0.050 to 0.251 mm. They provided time-averaged void fractions based on image analysis. They found that their 0.251 mm diameter void fraction data for water, ethanol and ethanol-water mixtures were approximately described by the Armand and Treschev (1946) correlation, which is in line with the observations of the other studies above. For their 0.075 and 0.100 mm channels for these fluids, there was again a huge deviation in the void fractions to much lower values, similar to those observed in the Chung and Kawaji (2004) study. The effect of the wide variation in physical properties between water and ethanol created a wide band of values in their data. Once again, these data are in sharp contrast to the data of Serizawa, Feng and Kawara (2002) described earlier for a 0.020 mm channel that approximately follow the Armand and Treschev (1946) correlation.

Agostini, Revellin and Thome (2008) have indirectly obtained void fraction data by applying the relationship among the void fraction, the superficial vapor velocity  $U_G$  (which can be determined experimentally from the mass velocity and local vapor quality exiting their micro-evaporator channel) and the mean vapor velocity in the sight glass channel  $u_G$ :

$$\varepsilon = \frac{U_G}{u_G} = \frac{\dot{m}x / \rho_G}{u_G} \quad [20.5.5]$$

They obtained the mean vapor velocity  $u_G$  by measuring the bubble velocities for bubbly and slug flows (and hence their approach is limited to only bubble types of flows) as well as the respective bubble lengths. The velocity of individual bubbles were determined from computerized image analysis of high speed, high definition digital video camera sequences and from these the bubble velocity and length were determined. The tests were done in 0.509 and 0.790 mm circular channels with R-134a for mass velocities from 200 to 1500 kg/m<sup>2</sup>s and vapor qualities from 0.02 to 0.19 at a nominal saturation temperature of 30°C. Figure 20.26 shows some of their results, where the relative bubble velocity (actual bubble velocity minus the homogeneous velocity  $u_H$  calculated from the mass velocity and vapor quality of the measurement) is divided by the parameter  $\gamma$  and plotted versus the bubble length. The parameter  $\gamma$  is the gradient of the superficial bubble velocity along the channel axis  $z$ , assuming no liquid or vapor superheating and that the annular liquid film surrounding the bubble is very thin compared to the channel diameter:

$$\gamma = \frac{d}{dz} \left( \frac{\dot{Q}_G}{A} \right) = \frac{d}{dz} U_G \quad [20.5.6]$$

After several simplifications, it is derived in their paper to be:

$$\gamma = \frac{4q}{d_i h_{LG} \rho_G} \quad [20.5.7]$$

In this expression, the uniform heat flux  $q$  applied to the evaporating fluid in the micro-evaporator channel of the same internal diameter is input together with the channel diameter  $d_i$ , the latent heat  $h_{LG}$  and the vapor density  $\rho_G$ , i.e. the thermal process that created the vapor bubble. It is quite evident that the bubble velocity increases with bubble length, beginning at the homogeneous velocity for short bubbles, then first rising rapidly with bubble length and then much more slowly for very long bubbles. It is also noteworthy to point out that elongated bubbles had lengths up to 69 mm in the 0.509 mm channel, which gives a bubble length to channel diameter ratio of 135!

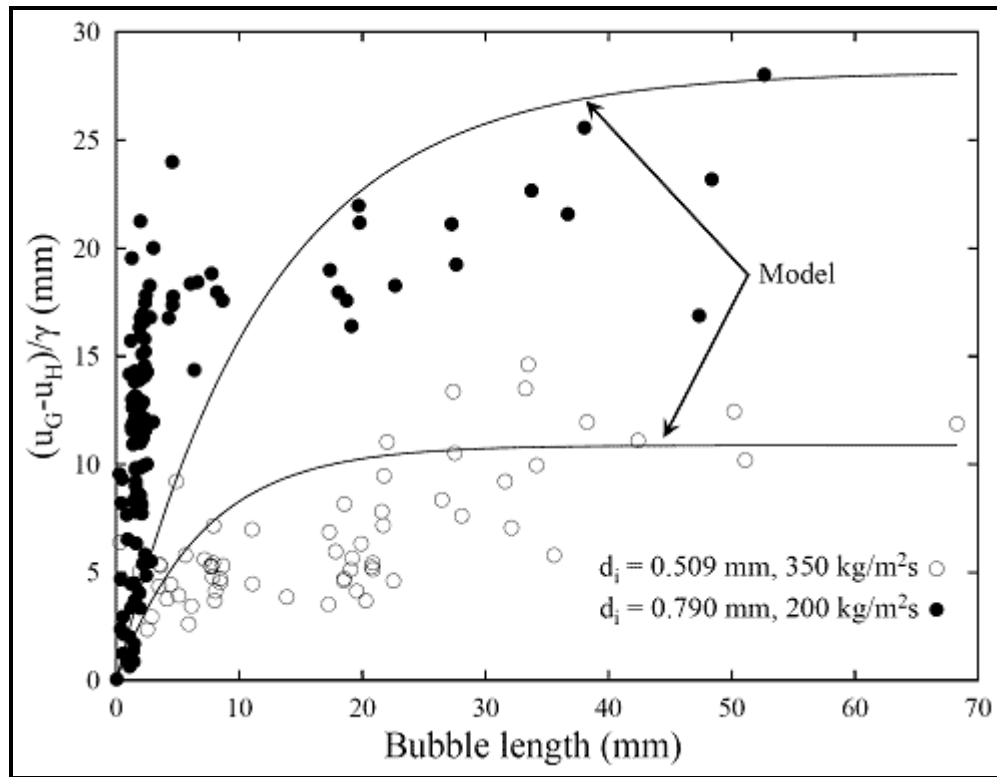


**Figure 20.26. Bubble velocity data of Agostini, Revellin and Thome (2008) for R-134a compared to their bubble velocity model.**

Agostini, Revellin and Thome (2008) proposed a model based on the conservation laws to predict the velocity of elongated bubbles in microchannels as a function of the bubble length. The following expression was derived for the elongated bubble velocity  $u_G$ :

$$u_G = \left( \frac{d_i \gamma}{1 - (0.58/Co)} \right) \frac{1 - \exp(-2f_i L_G/d_i)}{2f_i} + u_H \quad [20.5.8]$$

In this expression  $Co$  is the confinement number defined earlier,  $L_G$  is the length of the bubble and 0.58 is an empirically determined constant. The interfacial friction factor  $f_i$  is determined using the conventional relationships assuming the interface of the elongated bubble is smooth:

$$f_i = \frac{64}{\text{Re}_G} \text{ for } \text{Re}_G \leq 2000 \quad [20.5.9a]$$

$$f_i = \frac{0.316}{\text{Re}_G^{0.25}} \text{ for } \text{Re}_G > 2000 \quad [20.5.9b]$$

The Reynolds number of the vapor is based on the bubble velocity  $u_G$  ignoring the much smaller velocity of the liquid film:

$$\text{Re}_G = \frac{\rho_G u_G d_i}{\mu_G} \quad [20.5.10]$$

Hence, if the values of  $L_G$ ,  $d_i$ ,  $x$  and  $q$  are taken as the input for a specified flow and fluid properties, the bubble velocity can be calculated directly for a bubble of assumed length  $L_G$ . As yet, however, no proven method is available for predicting elongated bubble lengths in microchannels to obtain the values of  $L_G$ . The method was shown to predict nearly all of their bubble velocity data  $u_G$  to within  $\pm 20\%$  for both sizes of channels over a wide range of mass velocities and bubble lengths.

Knowing the elongated bubble velocity, the void fraction of elongated bubble flows is then easily predicted using the above method by inputting the calculated value of  $u_G$  into the above void fraction expression. Interestingly, this approach gives the void fraction of elongated bubble (slug) flows as a function of bubble length, where the longer the bubble the larger the deviation from the homogeneous model (that is, the longer is the bubble, the lower is the void fraction). Hence, for very short bubbles the method returns void fractions equal to the homogeneous void fraction as one would expect. Furthermore, the void fraction is seemed to be affected as bubbles grow in length during the evaporation process and coalescing.

In separate tests described in Revellin et al. (2008b), the same indirect approach was applied except that the bubble velocities were determined using the two laser / diode technique to determine the bubble velocities in the slug flow regime. The two light intensity signals from the two lasers were processed by a cross-correlation technique to find the time delay between the lasers and knowing the distance between the lasers, the mean bubble velocity of the bubbles was measurable, thus yielding the value of  $u_G$ . In this manner, they obtained 440-bubble velocity and indirectly 440 void fraction data points for R-134a in their 0.509 mm channel. Their set up was only applicable to elongated bubble (slug) flows and transition flows between bubbly and slug flows, as the distance between their two lasers was optimized for these types of flows. To study bubbly flows, the two lasers would need to be much closer together as the cross-correlation fails to fit the time delay when only very small bubbles are present. Figure 20.27 shows some of their data compared to the above model, where the red lines and symbols indicate the predicted values. The elongated bubble velocity model predicted 92% of their new bubble velocity database for R-134a measured by the two lasers / diode sets to within  $\pm 20\%$ .

In summary, various methods have been proposed for predicting void fractions in microchannels, but at present there does not appear to be one general method that is proven to work for a wide range of fluids and diameters. Further experimental work and a multi-fluid/multi-lab database are required to achieve this goal.

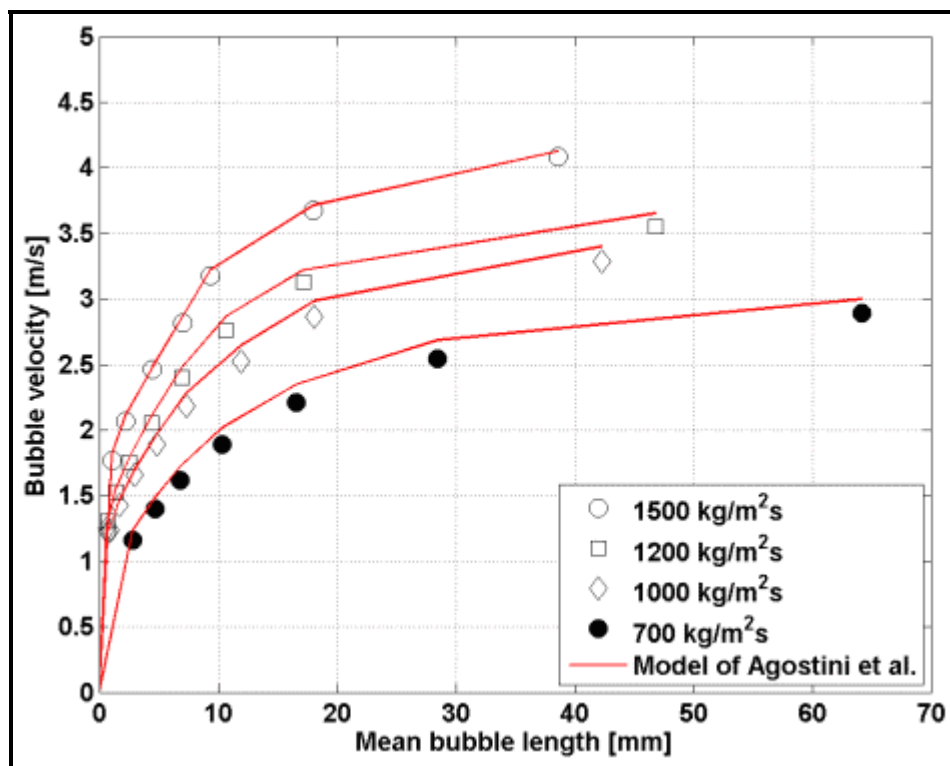


Figure 20.27. Bubble velocity data of Revellin et al. (2008b) for R-134a compared to the bubble velocity model of Agostini, Revellin and Thome (2008).

## 20.6. Flow Boiling in Microchannels

Flow boiling in microchannels has become in the past decade one of the “hottest” research topics in heat transfer. Numerous experimental studies are now available and new ones appear nearly every month in the leading journals. Below, a few examples of such experimental results will be given, the basic trends will be discussed and then the principal prediction methods proposed to date discussed.

### 20.6.1 Experimental Studies on Boiling in Microchannels

Numerous experimental studies on boiling in microchannels have appeared over the past decade, especially in the past few years. It is not possible to describe or list all of these here. Most tests have been done with refrigerants but tests have also been done with water, acetone, CO<sub>2</sub>, nitrogen, FC-72, etc. Below, a brief description of a selection of experimental studies is given.

Lazarek and Black (1982) investigated evaporation of R-113 in a 3.1 mm stainless steel tube with a two-part vertical test section heated by direct current. They performed experiments starting with subcooled liquid at the inlet. Figure 20.28 depicts their data for subcooled and saturated flow boiling. The saturated test results show a strong dependence on heat flux but a negligible influence of vapor quality, which is quite different than the usual trend in macroscale flow boiling in which the heat transfer coefficient tends to rise with increasing vapor quality and be less sensitive to heat flux. This suggested to them that nucleate boiling was controlling the heat transfer process in their 3.1 mm test section.

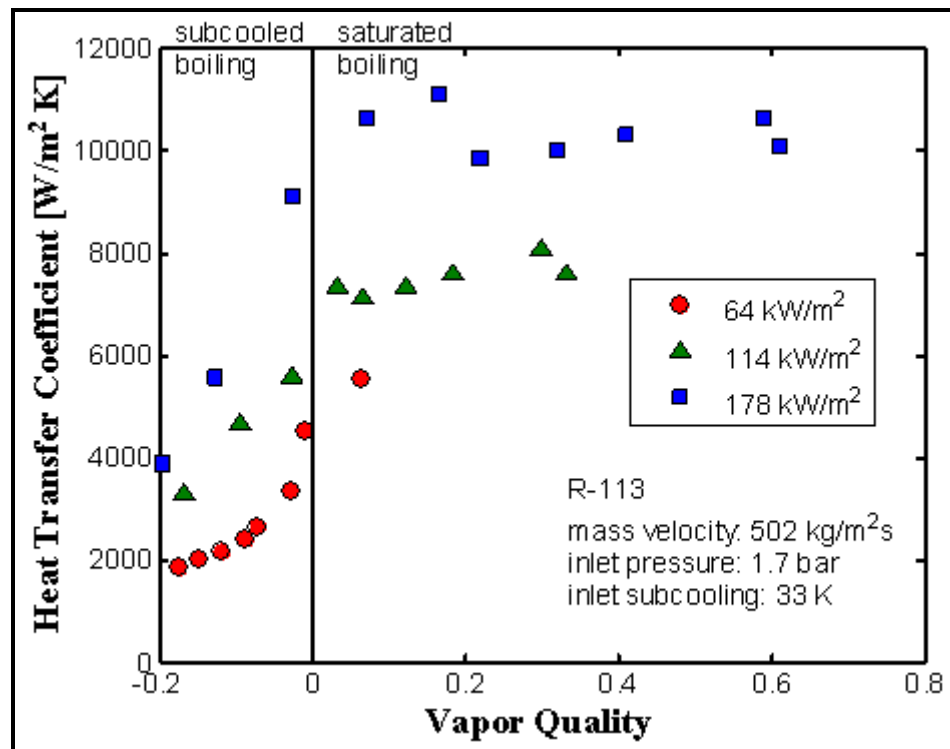


Figure 20.28. Flow boiling data of Lazarek and Black (1982) for R-113 in a 3.1 mm channel.

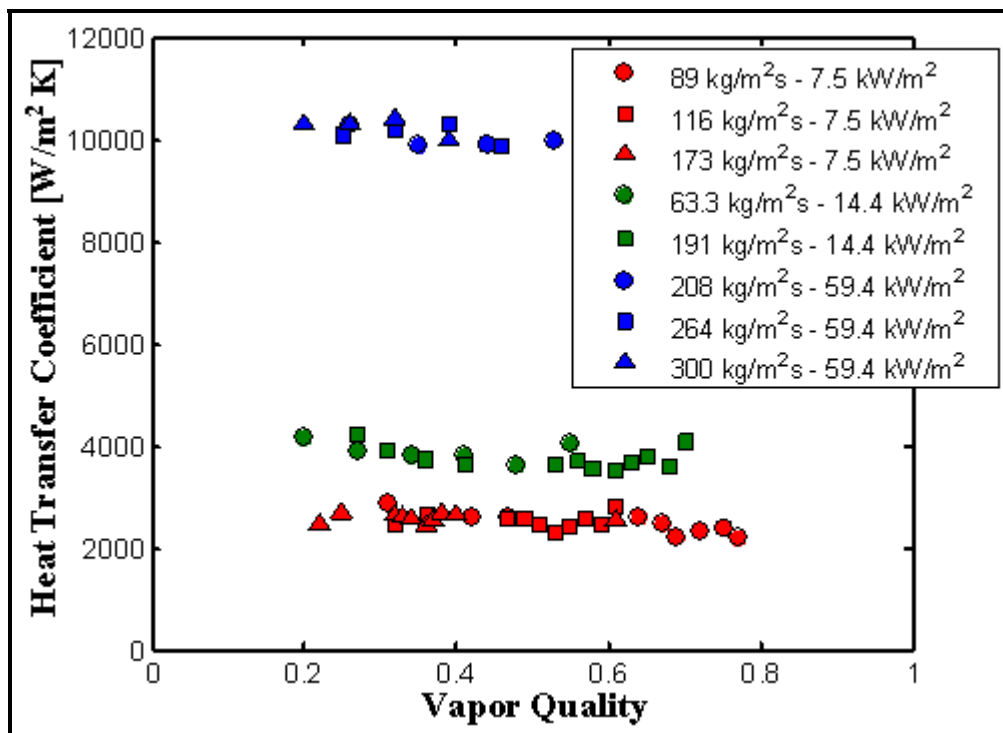
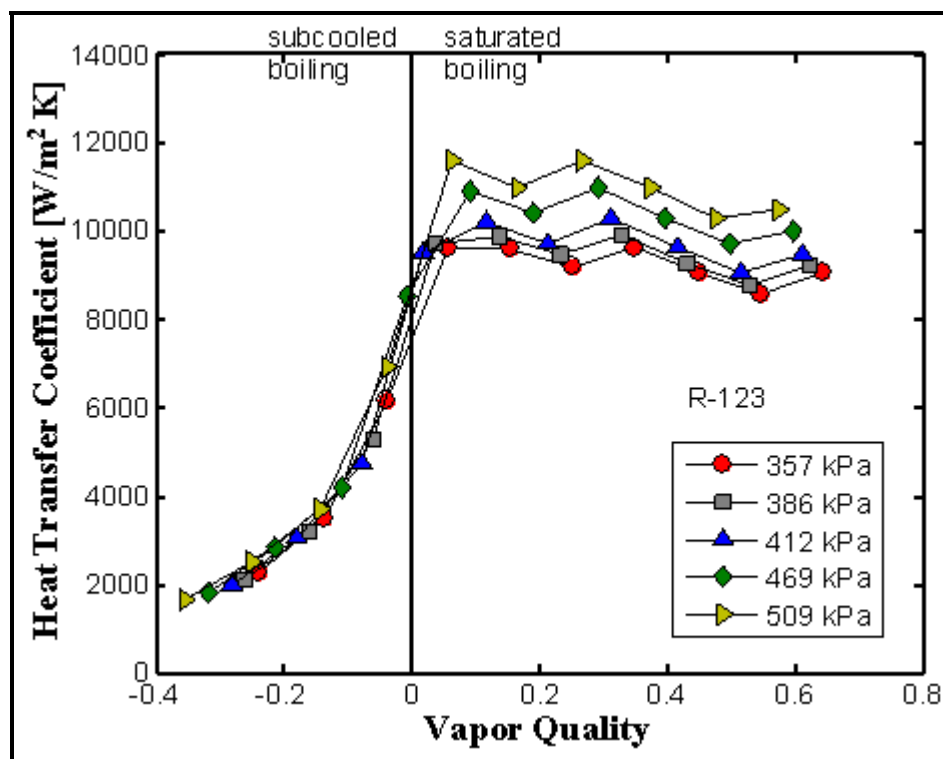


Figure 20.29. Flow boiling data of Tran, Wambsganss and France (1996) for R-12 evaporating in a 2.46 mm circular channel.



In a systematic study at Argonne Laboratory by Tran, Wambsganss and France (1996), they measured boiling heat transfer coefficients for R-12 evaporating in a 2.46 mm circular channel at three heat fluxes and a range of mass velocities. Their results are shown here in Figure 20.29. As can be seen, again there was little influence of vapor quality on the heat transfer coefficient but a large effect of heat flux. They also attributed this heat flux effect to the dominance of nucleate boiling in their small channel.

Bao, Fletcher and Haynes (2000) reported local flow boiling coefficients for R-11 and R-123 inside a copper tube with a diameter of 1.95 mm. They used a single piece of tubing, 870 mm long whose first 400 mm was an unheated entrance region. This was followed by a 270 mm long test zone and then by a 200 mm unheated exit zone. They did tests for mass velocities from 50 to 1800 kg/m<sup>2</sup>s, enthalpies from subcooled to saturated, heat fluxes from 5 to 200 kW/m<sup>2</sup>, and a range of saturation pressures. Some of their results are depicted in Figure 30.30. They observed that heat transfer coefficients were a strong function of heat flux and increased with saturation pressure while the effects of vapor quality and mass flux were small, although there was a slight decreasing trend in the heat transfer with increasing vapor quality. Similar to the previous studies, they concluded that nucleate boiling dominated the heat transfer process. Using the same type of set-up, Baird et al. (2000) also reported local heat transfer data for R-123 in a 0.92-mm-diameter tube and CO<sub>2</sub> in the previous 1.95 mm tube. They observed the same trends as in their earlier work.



**Figure 30.30. Flow boiling data of Bao, Fletcher and Haynes (2000) for R-123 inside a copper tube with a diameter of 1.95 mm.**

Lin, Kew and Cornwell (2001) studied evaporation of R-141b in a vertical 1.1 mm tube. Figure 20.31 depicts some of their results. The outlet pressure of the test section was atmospheric while the inlet pressure varied from 1.34 to 2.19 bar over the test conditions, which means their data include a small saturation pressure effect. As opposed to the above studies, they found a significant influence of vapor quality on the heat transfer coefficient. At high heat fluxes, their data exhibit a sharp peak at low vapor qualities followed by a monotonic decrease. At low heat fluxes, there was a significant monotonic rise in

value up to a peak at about  $x = 0.60$ . At intermediate heat fluxes, such as 42 and 48  $\text{kW/m}^2$ , the heat transfer coefficients were nearly independent of vapor quality as in previous investigations. Significantly, their results depict a more complex dependency of the heat transfer coefficient on heat flux and vapor quality than those in previous studies. They hypothesized that nucleate boiling dominated at low vapor qualities and that convective boiling dominated at high vapour quality.

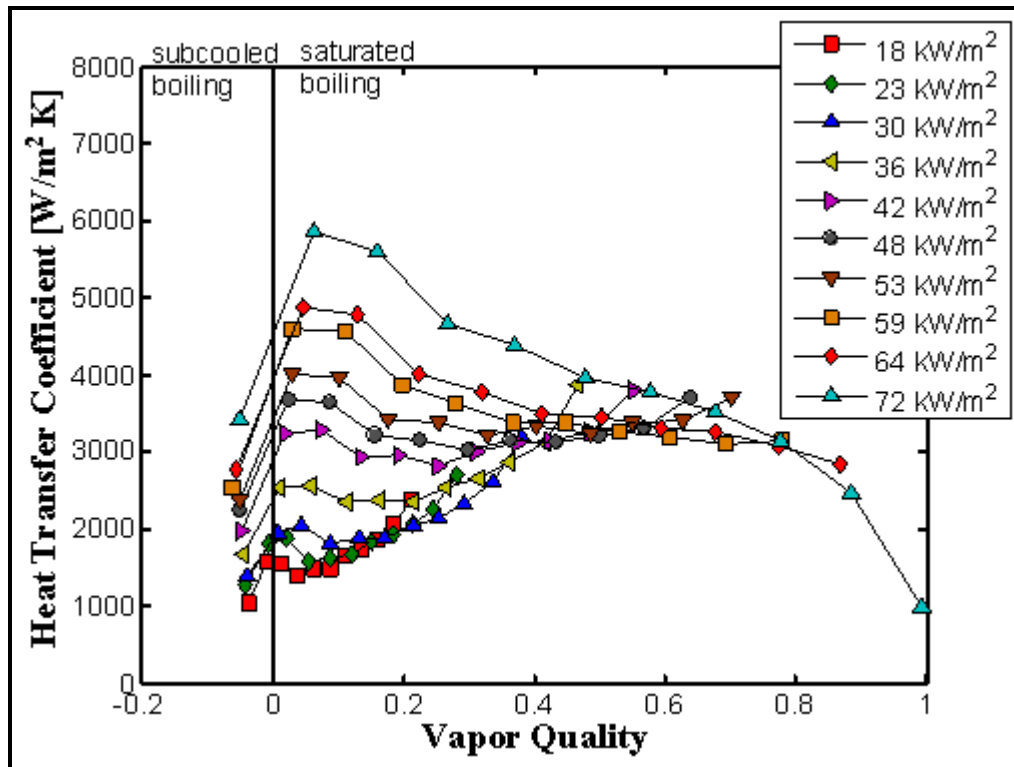


**Figure 20.31. Flow boiling data of Lin, Kew and Cornwell (2001) for R-141b inside a vertical tube of 1.1 mm diameter at 510  $\text{kg/m}^2\text{s}$ .**

Saitoh, Daiguji and Hihara (2005) investigated flow boiling of R-134a in 0.51, 1.12 and 3.1 mm horizontal channels over a significant range of test conditions. They found that the effect of heat flux was strong for all three tube diameters but that the effect of mass velocity decreased with decreasing tube diameter. In their tests, the fluid entered their test section as a two-phase flow created by an expansion valve. They only observed annular flows and intermittent (plug and slug) flows according to their paper, but in fact were limited to vapor qualities with  $x > 0.2$ , which precluded them from obtaining any data in the bubbly flow regime. The heat transfer was highest in their 0.51 mm tube for vapor qualities less than 0.5. In another study on the tube diameter effect with R-134a, Owhaib, Martin-Callizo and Palm (2004) found that the heat transfer coefficients were higher as tube diameter decreased for their vertical glass tubes of 0.83, 1.22 and 1.70 mm diameters. In another study by the same lab, Martin-Callizo, Ali and Palm (2007) presented results for a vertical 0.64 mm stainless steel microchannel, finding that once again the dominant effect was that of heat flux while mass velocity was less important. They found that their heat transfer coefficients were rather insensitive to vapor quality until reaching the higher range of their heat flux test range, where upon the heat transfer coefficients then decreased monotonically from vapor qualities of about 0.01-0.02 down to values of about 0.6-0.8 without going through any maximum or minimum. Chen, Tian and Karayiannis (2006) and Shiferaw et al. (2007) also studied flow boiling of R-134a in vertical 1.10 to 4.26 mm stainless steel tubes together with flow pattern observations.

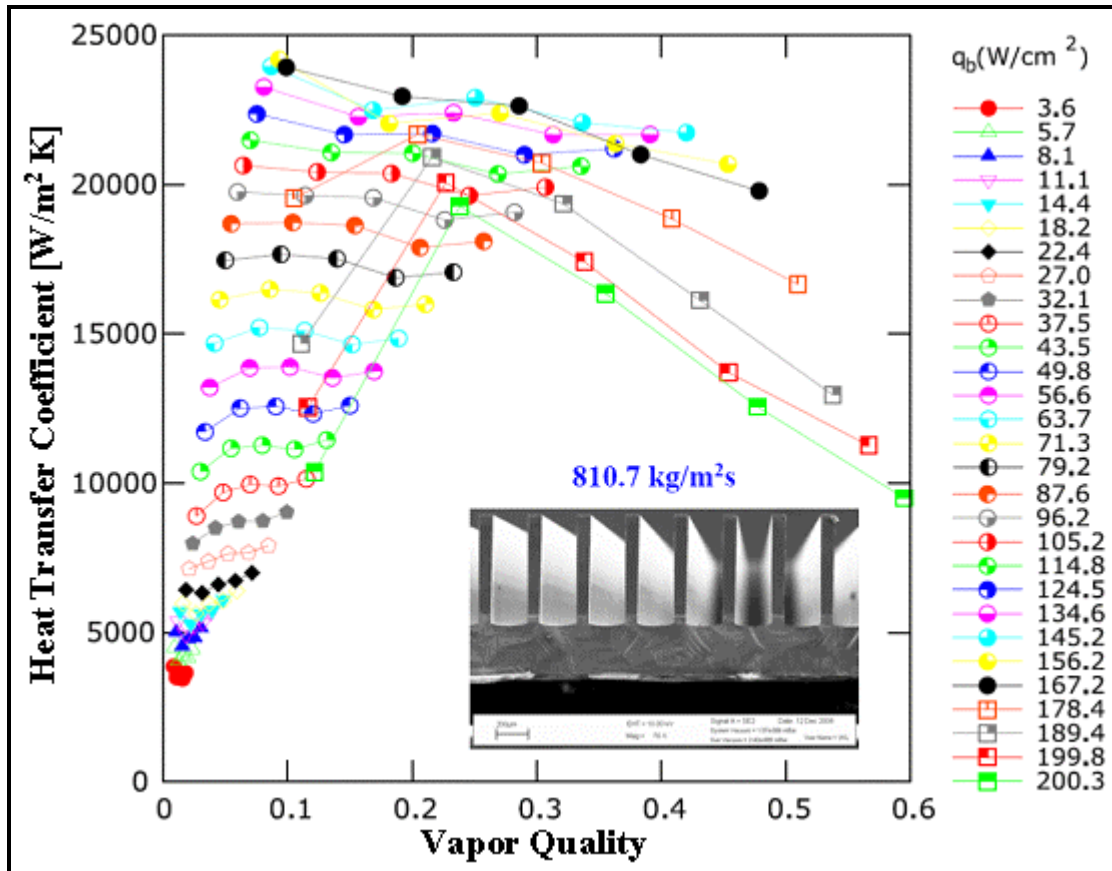


**Figure 20.32.** Flow boiling data of Agostini et al. (2008a) for R-236fa in a silicon multi-microchannel test section at a mass velocity of  $810.7 \text{ kg/m}^2\text{s}$ , a nominal pressure of 2.73 bar and saturation temperature of  $25^\circ\text{C}$ . The silicon test section without its cover plate is shown in the inset photograph.

Agostini et al. (2008a) and Agostini et al. (2008b) have measured flow boiling heat transfer coefficients for R-236fa and R-245fa, respectively, in a silicon heat sink made with 67 parallel, high aspect ratio, rectangular channels that were 0.223 mm wide, 0.680 mm high and 20.0 mm long with 0.080 mm fins between the channels. The top of the channels was closed with a transparent plate for flow visualization while small rectangular orifices were formed at the entrance to each individual channel by the connection of the inlet distributor to the channels. *These orifices resulted in uniform flow (based on videos taken), prevented back flow into the inlet distributor and slightly flashed the subcooled inlet liquid to “jump start” the boiling process with a stream of bubbles that then grew along the channels, thus avoided any temperature overshoot to initiate the boiling process.* Consequently, they resolved several annoying problems with multi-microchannel evaporator elements in one stroke. Some of their results for R-236fa are shown in Figure 20.32, where the base heat flux  $q_b$  refers to that through the base of the 2 cm by 2 cm silicon test section into the channels. The heat transfer coefficients instead refer to the effective heat transfer area of the silicon channels taking into account the fin efficiency for each individual test condition. It can be seen that the heat transfer data at low heat fluxes tend to increase with vapor quality until intermediate heat fluxes where they first increase with vapor quality and then show nearly no influence of vapor quality. At higher heat fluxes, the heat transfer coefficients start to decline with increasing vapor quality. While the heat transfer coefficients rise sharply with increasing heat flux, at the high values starting at  $q_b = 178.4 \text{ W/cm}^2$ , a peak is reached and the heat transfer coefficients begin to decrease with increasing heat flux as CHF is approached (but not reached) in this data set. Notably, local

heat transfer coefficients were measured in this study at base heat fluxes over  $200 \text{ W/cm}^2$ , which are in the range of those required for the design of computer microprocessor cooling elements.

Agostini et al. (2008d) have also measured local flow boiling heat transfer coefficients for R-236fa in a silicon test section with 134 parallel, rectangular channels that were 0.067 mm wide and 0.680 mm high with fins 0.092 mm thick on a heated area of 20 mm by 20 mm. The channels had a surface roughness of  $0.160 \mu\text{m} \pm 0.050 \mu\text{m}$ . They used one central inlet at the center of the channel length and two outlets, one at each end, to greatly reduce the two-phase pressure drop. The narrow but wide inlet header and each channel created a rectangular orifice at the top of each channel, with the flow then splitting as it made a  $90^\circ$  turn to flow along the channel in both directions. They found that they could achieve base temperatures uniform within about  $\pm 1\text{K}$  at base heat fluxes up to as high as  $210 \text{ W/cm}^2$ . The highest base heat flux they reached was  $255 \text{ W/cm}^2$ , not the critical heat flux but from a limitation of their pump, while maintaining the base temperature below  $52^\circ\text{C}$  at a R-236fa flow rate of 0.49 l/min. The pressure drop at this condition was about 0.9 bar, but about one-third of this was due to the orifices their test section also had at the exit with another  $90^\circ$  bend in the flow, orifices which would not be necessary in an actual microprocessor cooling application. In their tests, they reached flow boiling heat transfer coefficients, relative to the base area of their test section, up to nearly  $180 \text{ kW/m}^2\text{K}$  using a refrigerant, in particular underneath the impinging jets created by the orifices, while the corresponding heat transfer coefficients near the exit were nearly  $160 \text{ kW/m}^2\text{K}$ .

Many other test results can be found in the literature for a growing list of fluids, for example for liquid nitrogen by Qi et al. (2007a) and for FC-72 by Muwanga and Hassan (2007). The latter used liquid crystal thermography to measure local flow boiling heat transfer coefficients for a 1.067 mm diameter channel.

Some general comments are in order with respect to published experimental results that should be considered when making new tests. Most studies have not measured subcooled liquid laminar and/or turbulent flow heat transfer coefficients prior to the flow boiling tests, which is an important experimental benchmark to prove that the test section is providing accurate results and giving good energy balances. Secondly, most studies do not report the internal surface roughness of the test section which may influence the heat transfer process, and thus may be useful in the eventual prediction of the data set. Thirdly, achieving steady-state conditions seems in some cases to be an experimental challenge and hence it is important to label data as being obtained at *stable* or *unstable* conditions, i.e. it seems that boiling in very long microchannel test sections is inherently unstable due to compressible volume effects. Finally, for non-circular channels it is important to cite which perimeter, the actual or that of the hydraulic diameter, is used to calculate the heat flux and hence utilized to report the boiling heat transfer coefficient.

Agostini and Thome (2005) analyzed 13 published microchannel flow boiling studies, noting numerous widely different trends in the heat transfer data. Figure 20.33 shows a composite diagram of these trends in the local flow boiling heat transfer coefficient plotted versus the vapor quality and denotes whether or not the heat transfer coefficient varied with another parameter, where an arrow with the symbol shows the direction of the variation with this parameter. For instance, qx1 means that the heat transfer coefficient decreased with increasing vapor quality but at the same time the heat transfer coefficient increased with increasing heat flux while qx2 showed a similar trend except that the data all came together at a higher vapor quality. In contrast, qx3 describes data in which the heat transfer coefficient increased with vapor quality and with heat flux. The x1 data type decreased sharply with vapor quality but did not depend on mass velocity or heat flux, whereas x2 refers to data sets that only increased with vapor quality while were insensitive to mass velocity and heat flux. The data types mx1, mx2 and mx3 showed three types of trends with respect to mass velocity and vapor quality.

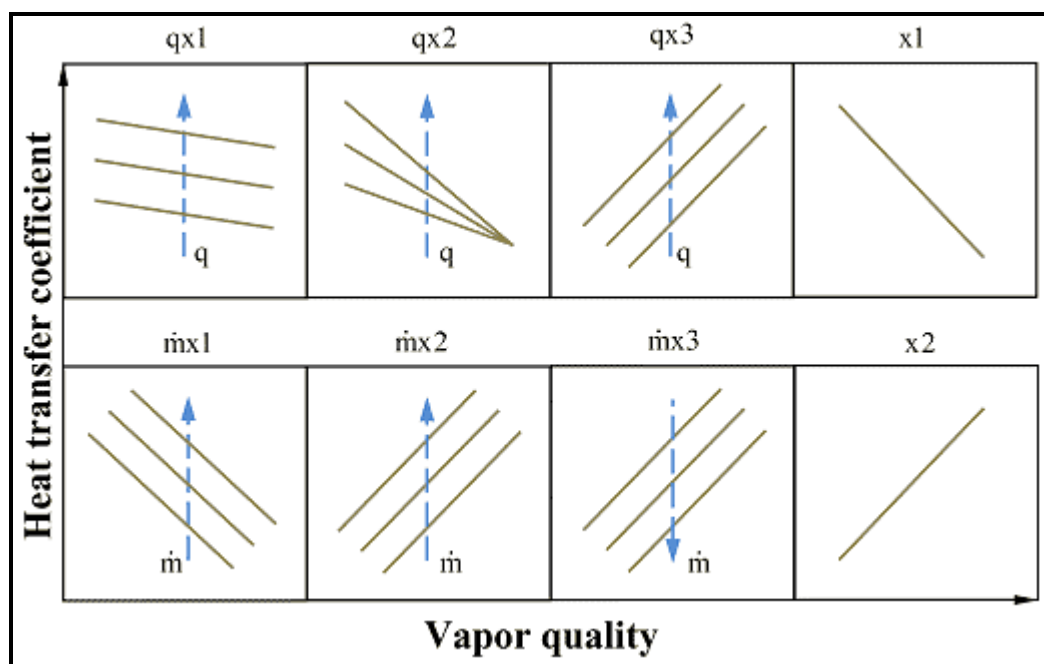


**Figure 20.33. Heat transfer trends versus vapor quality documented by Agostini and Thome (2005) from 13 different studies on boiling in microchannels.**

The majority of the studies found boiling heat transfer trends represented by  $qx1$  and  $x1$  (11 out of 13), although some studies yielded more than one type of trend. It was thus concluded generally that:

- at very low vapor qualities ( $x < 0.05$ ), the heat transfer coefficient either tends to increase with vapor quality or is insensitive to vapor quality while it increases with heat flux (not shown);
- at low to medium vapor qualities ( $0.05 < x < 0.5$ ), the heat transfer coefficient increases with heat flux and decreases, or is relatively constant, with respect to vapor quality;
- at higher vapor qualities ( $x > 0.5$ ), the heat transfer coefficient decreases sharply with vapor quality and does not depend on heat flux or mass velocity;
- increasing the heat flux increases the heat transfer coefficient except at high vapor quality where it tends to have little effect (more recent studies show however that at very high heat flux its effect diminishes and then may even create a decrease in heat transfer with a further increase in heat flux);
- the influence of mass velocity varies from no effect, an increasing effect, or a decreasing effect.

These conflicting trends, which are different than the simple trends typically found in macroscale flow boiling, appear to point to the influence of additional phenomena, surface roughness and/or heat transfer mechanisms coming into play in microchannel boiling. Some additional aspects to consider are:

**Heat transfer mechanisms:** the heat transfer mechanisms active during boiling in microchannels can be summarized as follows: (i) in bubbly flow, nucleate boiling and liquid convection can be assumed to dominate, (ii) in slug flow, the thin film evaporation of the liquid film trapped between the bubble and the wall is usually the most important heat transfer mechanism, while liquid convection to the slug and vapor convection, when there is a dry zone present, are also important, depending on their relative residence times, (iii) in annular flow, convective evaporation across the liquid film should be dominant and (iv) in mist flow, vapor phase heat transfer with droplet impingement will be the primary mode of heat transfer. *Notably, many experimental papers conclude without proof that nucleate boiling is dominant in their data*



only because they find a substantial heat flux dependency; a heat flux dependency, however, does not prove that nucleate boiling is dominant or even present. For instance, Jacobi and Thome (2002) have shown that the heat flux effect can be explained and predicted by the thin film evaporation process occurring around elongated bubbles in the slug flow regime without any nucleation sites. Thome, Dupont and Jacobi (2004) have proven that a mechanistic heat transfer model in this regime can predict the test data for 7 different liquids from 7 different laboratories without including nucleate boiling. Thus, it is not credible to simply label microchannel flow boiling data as being nucleate boiling dominated since this seems to only be the case for the bubbly flow regime, which occurs at very low vapor qualities (typically for  $x < 0.01$ -0.05 depending on the mass velocity, etc.). Incredibly, some experimental flow boiling studies that report that nucleate boiling was dominant at low vapor qualities also report that the flow regime observed at these conditions was elongated bubble flow without any bubbly flow observed; these two conclusions are contradictory. Hence, more attention is required when describing and writing up the analysis of experimental flow boiling results, since it is not correct to label data as being nucleate boiling dominated if no nucleation sites are active at those locations in the test section. In the future, it is highly recommended that researchers provide some fundamental analysis to back up their conclusions on the dominance of a particular heat transfer mechanism (or omit declaring one) rather than just attaching superficially a convenient but potentially incorrect label.

**Non-circular channel effects:** Many types of non-circular microchannels have been tested, for instance square, rectangular, parallel plate, triangular, trapezoidal, etc. Besides the problems associated with characterizing the channel size (e.g., a hydraulic diameter of a non-circular channel has no physical relationship to an annular film flow), the rectangular channels tested sometimes have very high aspect ratios whose effect on heat transfer is not well understood. Recalling the wedge flows observed by Cubaud and Ho (2004) for air-water, a partially wetted perimeter along and around elongated bubbles will have an influence on heat transfer whilst the wet corners may tend to better resist complete dryout. Such a process might explain the decreasing trend in the heat transfer coefficient vs. vapor quality, but only for non-circular channels. Furthermore, it is common practice to use the hydraulic diameter in two-phase flows, but it has never been proven to be correct, i.e. an annular flow has a thin liquid film on the perimeter, which would not appear to be characterized by the hydraulic diameter. Hence, the equivalent diameter may be more appropriate, which is a circular channel with the same cross-sectional area as the non-circular channel; it has the same mass velocity but not the same wetted perimeter (and hence also has its adverse side).

**Explosive boiling effects:** various studies have reported "explosive" boiling phenomena in which bubble nucleation occurs, the bubble grows rapidly in both upstream and downstream directions, then dryout sets in, and finally rewetting occurs, without establishment of the conventional flow regimes. For example, this has been observed in Hetsroni et al. (2002, 2003), Xu et al. (2005), and Yen et al. (2006) and some videos are shown in Chapter 1 of this book. Hetsroni and coworkers observed that high heat fluxes created a quasi-periodic rewetting and refilling of their multi-microchannel test elements, with a cyclic period on the order of 1 Hz, which were attributed to cyclic bubble growth and collapse. In a detailed study, Jiang et al. (2002) investigated boiling in channels from 0.025 to 0.300 mm diameter with water. They noted that annular flow generally was formed in their larger channels, but at hydraulic diameters less than 0.044 mm, the evaporation process changed and appeared as a sudden eruption of vapor. In particular, at the onset of boiling, small bubbles nucleated on their plasma etched silicon surface, grew, departed, became an annular flow and then quickly turned into a mist flow. In effect, at these conditions they reported that boiling always began with a sudden eruption of vapor at any heat flux or flow rate, such that the bubbly flow regime barely existed, and that mist flow formed immediately down stream. Specifically according to their study, this process was very evident in their smallest channels with hydraulic diameters from 0.025 to 0.044 mm, which means that heat transfer at such conditions is controlled by a different set of heat transfer phenomena and mechanisms than in larger microchannels.



Because of the mist flow, this suggests that very small microchannels may be detrimental to achieving good heat transfer and thus more work is needed to clarify and quantify this effect.

**Flow maldistribution/backflow effects:** multi-microchannel flow boiling test sections can suffer from flow maldistribution and backflow effects, where some channels have higher liquid flow rates than others, the fluid may flow backward into the inlet header, and some channels may become prematurely dry. Figure 20.34 of Park (2008) shows the dramatic effect that maldistribution can have on the heat transfer process in his copper test section, which can however be rectified by use of correctly sized inlet orifices.

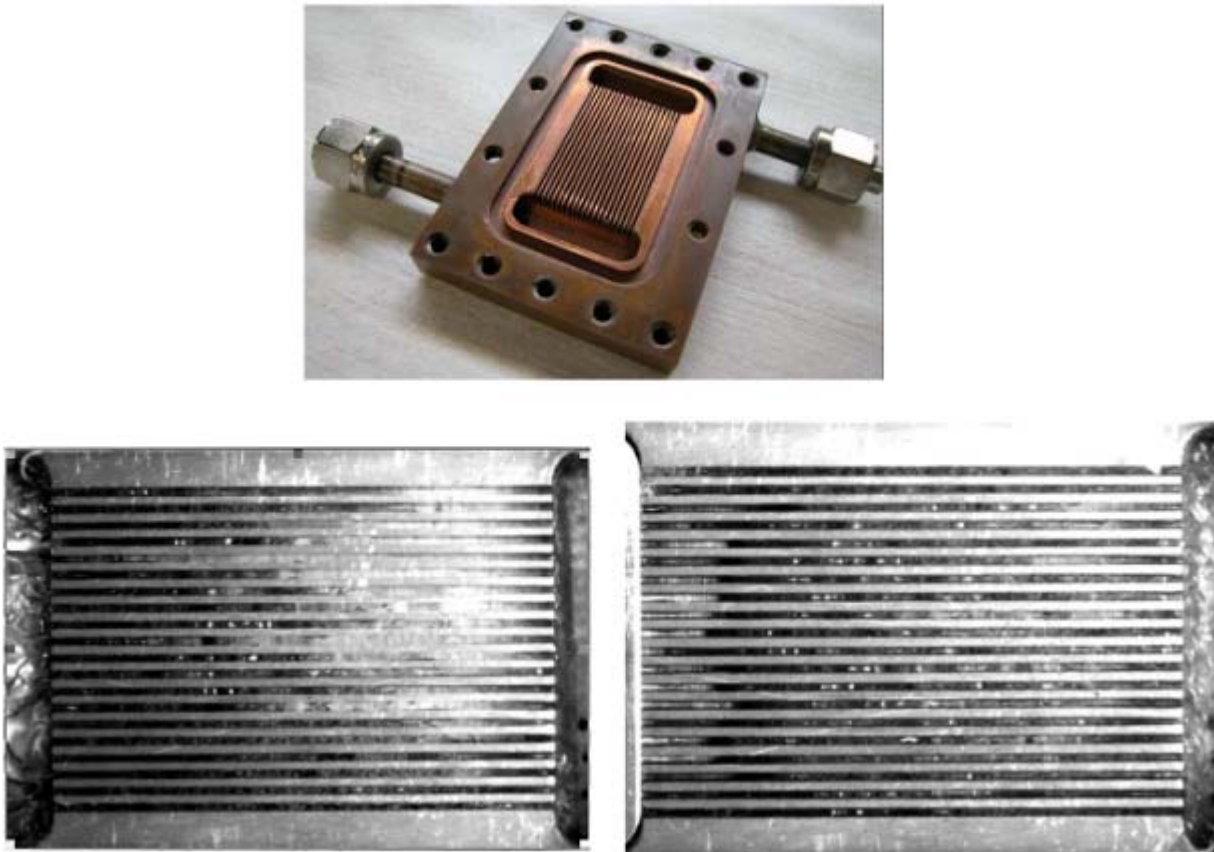


**Figure 20.34.** Flow boiling in copper multi-microchannel test section from Park (2008). *Top:* test section with 20 channels of 0.45 mm width and 4.0 mm height with flow from inlet header at left to right; *Lower Left:* R-245fa at  $q_b = 1150 \text{ kW/m}^2$  at  $80 \text{ kg/m}^2\text{s}$ , saturation temperature of  $40^\circ\text{C}$  and 20 K of subcooling with significant maldistribution, local dryout and backflow; *Lower Right:* R-134a at identical conditions with an inlet orifice at the entrance to each individual channel showing no maldistribution or local dryout.

Thus, in summary, additional work on both steady and unsteady flow boiling is required in single and multiple microchannel test sections to explain all these various trends and phenomena.

### 20.6.2 Empirical Prediction Methods for Boiling in Microchannels

Various empirical expressions for boiling in microchannels have been proposed. Below, those most often cited in the literature are presented.

Apparently, the first empirical prediction method proposed for flow boiling in a small channel was that proposed by Lazarek and Black (1982) based on their limited database for R-113 in a round vertical 3.1 mm tube. Hence, this tube size is near the lower end of the macroscale or mesoscale diameter range and is not necessarily a microchannel. Their database of 728 local heat transfer coefficients covered both upflow and downflow, for which they reported little experimental difference. Their Nusselt type of correlation is:

$$\frac{\alpha_{tp} d_i}{k_L} = 30 \text{Re}_L^{0.857} \text{Bo}^{0.714} \quad [20.6.1]$$

In this expression, the Boiling number Bo and the liquid Reynolds number  $\text{Re}_L$  based on the mass velocity of the total flow of liquid and vapor, are both defined earlier in Section 20.4. The range of parameters were as follows: heat fluxes from 14 to 380 kW/m<sup>2</sup>, mass velocities from 125 to 750 kg/m<sup>2</sup>s, pressures from 1.3 to 4.1 bar,  $\text{Re}_L$  from 860 to 5500, and Bo from 0.00023 to 0.00076. They predicted most of their database within  $\pm 15\%$ . Analyzing this expression, one notes the following tendencies:  $\alpha_{tp} \sim q^{0.714}$ ,  $\alpha_{tp} \sim (d_i)^{-0.143}$ ,  $\alpha_{tp} \sim \dot{m}^{0.143}$  and that  $\alpha_{tp}$  has no dependency on  $x$  at all. In most cases, all four of these tendencies approximately and qualitatively respect the general trends in the experimental data cited above.

Tran, Wambsganss and France (1996) developed a correlation based on their results for two refrigerants (R-12 and R-113) in small circular and rectangular channels. Their test conditions covered vapor qualities up to 0.94, mass velocities from 44 to 832 kg/m<sup>2</sup>s, and heat fluxes from 3.6 to 129 kW/m<sup>2</sup>. Their database of 296 points covered two circular channels (2.46 and 2.92 mm) and one rectangular channel (1.70 by 4.06 mm) with a hydraulic diameter of 2.40 mm while saturation pressures ranged from about 5.1 to 8.2 bar and Boiling numbers from 0.00020 to 0.00230. Only heat transfer data with a wall superheat larger than 2.75 K were considered in making what they called a “nucleate-dominant regime” correlation. Their correlation is:

$$\alpha_{tp} = 840000 (\text{Bo}^2 \text{We}_{d_i})^{0.3} \left( \frac{\rho_L}{\rho_G} \right)^{-0.4} \quad [20.6.2]$$

The heat transfer coefficient is given in W/m<sup>2</sup>K by this dimensional correlation. The lead constant in their publication is given as  $8.4 \times 10^{-5}$ , but this apparently is a typographical error as that would yield values of  $\alpha_{tp}$  close to zero. The hydraulic diameter is used for non-circular channels in place of  $d_i$ , and the liquid Weber number, based on the channel diameter, is defined as:

$$\text{We}_{d_i} = \frac{\dot{m}^2 d_i}{\rho_L \sigma} \quad [20.6.3]$$

This simple heat transfer correlation is independent of vapor quality and predicted most of their data to within  $\pm 15\%$ . Interestingly, this expression completely cancels out any effect of mass velocity on the heat transfer coefficient when combining its influence in the Boiling and Weber numbers and also says that  $\alpha_{tp} \sim q^{0.6}$  and that  $\alpha_{tp} \sim (d_i)^{0.3}$ . While the heat flux dependency is approximately in line with experimental data of others, the recent experimental studies on the diameter effect noted earlier found that heat transfer increased with decreasing diameter, so this last tendency appears not to be correct. Furthermore, quite surprisingly, this correlation says that the heat transfer coefficient is completely independent of the liquid thermal conductivity, which again seems to be quite unlikely.

Zhang, Hibiki and Mishima (2004) proposed a micro-scale version of the macro-scale flow boiling correlation proposed by Chen (1963). In their approach, the correlation by Foster and Zuber (1955) was retained to predict the nucleate boiling heat transfer component. The boiling suppression factor proposed by Chen was also utilized. However, in the new version, to determine the convective enhancement factor and the single-phase heat transfer coefficient, flow conditions (laminar or turbulent) were taken into account. This correlation was compared against experimental data from the literature for water, R-11, R-12 and R-113 taken from 13 publications, including vertical and horizontal orientations and circular and non-circular channels, and gave a mean deviation of 18.3%. Their Chen-like correlation is given as:

$$\alpha_{tp} = \alpha_{FZ} S + \alpha_L F \quad [20.6.4]$$

The Forster-Zuber correlation gives the nucleate pool boiling coefficient as:

$$\alpha_{FZ} = 0.00122 \left[ \frac{k_L^{0.79} c_{pL}^{0.45} \rho_L^{0.49}}{\sigma^{0.5} \mu_L^{0.29} h_{LG}^{0.24} \rho_G^{0.24}} \right] \Delta T_{sat}^{0.24} \Delta p_{sat}^{0.75} \quad [20.6.5]$$

where the wall superheat  $\Delta T_{sat}$  is the local temperature difference between the inner tube wall ( $T_{wall}$ ) and the local saturation temperature ( $T_{sat}$ ), such that  $\Delta T_{sat} = (T_{wall} - T_{sat})$ . The pressure difference  $\Delta p_{sat}$  is obtained from the vapor pressures of the fluid at the wall temperature ( $p_{wall}$ ) and at the saturation temperature ( $p_{sat}$ ), such that  $\Delta p_{sat} = (p_{wall} - p_{sat})$ . In this expression,  $\Delta p_{sat}$  is in the units of  $N/m^2$ . The liquid-phase convective heat transfer coefficient  $\alpha_L$  is given by the Dittus-Boelter (1930) correlation when the flow is turbulent:

$$\alpha_L = 0.023 Re_L^{0.8} Pr_L^{0.4} \left( \frac{k_L}{d_i} \right) \quad [20.6.6]$$

Here, the liquid Reynolds number  $Re_L$  of the liquid fraction is used:

$$Re_L = \frac{\dot{m}(1-x)d_i}{\mu_L} \quad [20.6.7]$$

The local vapor quality is  $x$  and the total mass velocity of the liquid plus vapor is  $\dot{m}$  in the tube of internal diameter  $d_i$ .  $Pr_L$  is the liquid Prandtl number defined as:

$$Pr_L = \frac{c_{pL} \mu_L}{k_L} \quad [20.6.8]$$

For laminar flow liquid heat transfer, the fully developed uniform heat flux expression is used:

$$Nu_L = \frac{\alpha_L d_i}{k_L} = 4.36 \quad [20.6.9]$$

A third expression is also presented to account for natural convection effects in laminar flow in vertical tubes and a fourth expression for rectangular channels; refer to the original paper for those details. The Chen boiling suppression factor  $S$  is changed to:

$$S = \frac{1}{1 + 0.00000253 \text{Re}_L^{1.17}} \quad [20.6.10]$$

That is, the use of the two-phase Reynolds number of Chen ( $= \text{Re}_L F$ ) was abandoned in calculating  $S$ . The rest of the method then gives their new approach to calculate the value of  $F$  for laminar, turbulent and transition flows in circular and non-circular channels using specific friction factor expressions; the reader is referred to their paper for the rest of these details. In particular, the authors provided no proof that nucleate boiling was actually present in their database for flow boiling in microchannels; they only cited experimental studies that had concluded that there was nucleate boiling. Consequently, if nucleate boiling is not an important heat transfer mechanism, as seems to be likely in slug flow and annular flow as discussed earlier, then the suppression factor should effectively cancel out the nucleate boiling influence in the above method at nearly all test conditions.

Kandlikar and Balasubramanian (2004) extended the macro-scale flow boiling prediction method of Kandlikar (1990) to channels with diameters less than 3 mm by taking into account the liquid flow conditions (laminar or turbulent) in calculating the all-liquid heat transfer coefficient. Since stratified flows do not exist in these small channels, the Froude number was eliminated from the method whilst the values for the empirical fluid/material constant  $F_{sf}$  were kept the same as in the previous version, for which values are available for a number of fluid and tube material combinations (refer to their papers). They proposed new correlations for predicting the nucleate boiling heat transfer coefficient  $\alpha_{nb}$  and the convective boiling heat transfer coefficient  $\alpha_{cb}$  (choosing the larger of the two as their value of  $\alpha_{tp}$ ). Their method for predicting the nucleate boiling heat transfer coefficient, using the Boiling number, is:

$$\frac{\alpha_{nb}}{\alpha_L} = 0.6683 \left[ \left( \frac{\rho_G}{\rho_L} \right)^{0.5} \left( \frac{1-x}{x} \right)^{0.8} \right]^{-0.2} (1-x)^{0.8} + 1058.0 \text{Bo}^{0.7} (1-x)^{0.8} F_{sf} \quad [20.6.11]$$

The convective boiling heat transfer coefficient is similarly predicted by:

$$\frac{\alpha_{cb}}{\alpha_L} = 1.136 \left[ \left( \frac{\rho_G}{\rho_L} \right)^{0.5} \left( \frac{1-x}{x} \right)^{0.8} \right]^{-0.9} (1-x)^{0.8} + 667.2 \text{Bo}^{0.7} (1-x)^{0.8} F_{sf} \quad [20.6.12]$$

They assumed all the flow as liquid for calculating their liquid Reynolds number:

$$\text{Re}_L = \frac{\dot{m} d_i}{\mu_L} \quad [20.6.13]$$

For  $\text{Re}_L > 3000$ , they recommended using either the Gnielinski (1976) correlation or the Petukhov (1970) correlation to obtain all liquid heat transfer coefficients  $\alpha_L$ . For  $\text{Re}_L < 1600$ , they suggested using the appropriate laminar flow heat transfer method, such as  $\text{Nu}_L = 4.364$  for fully developed laminar flow with a uniform heat flux boundary condition. For  $1600 < \text{Re}_L < 3000$ , they proposed using an interpolation to find the transition value of  $\alpha_L$ . Finally, for  $\text{Re}_L < 100$ , they directly used the nucleate boiling heat transfer coefficient  $\alpha_{nb}$  as the value of  $\alpha_{tp}$ . Similar to the experimental studies and flow boiling correlations above, they gave no direct proof that nucleate boiling was present in their database other than from the existence of a heat flux dependency. Interestingly, their nucleate boiling and convective boiling heat transfer

correlations are nearly identical, except for the numerical values of the two lead constants and one of the exponents.

Figure 20.35 depicts a comparison of the four empirical methods described above (and the three-zone model to be presented below) for R-134a boiling in a 0.5 mm microchannel taken from Consolini (2008). As can be seen, the Lazarek-Black and the Tran et al. correlations predict no influence of vapor quality and hence give a fixed value at all values of  $x$ . The Zhang-Mishima-Hibiki correlation depicts a slight increase in heat transfer at low vapor quality, nearly no effect of vapor quality at intermediate values and then an upward tendency, but its extrapolation to high vapor qualities is clearly not appropriate. The Kandlikar-Balasubramanian correlation shows a tendency to decrease with vapor quality before flattening off at the present simulated conditions. Meanwhile, the Thome-Dupont-Jacobi three-zone model for elongated bubble flows depicts a monotonic decrease in the heat transfer coefficient when also extrapolating it to low vapor qualities characterized by bubbly flow and to high vapor qualities characterized by annular flow. Notable in this simulation is the large discrepancy in the predicted values, which range from about 4000 to 11,000 W/m<sup>2</sup>K. Furthermore, it is evident that reliable application of heat transfer prediction methods requires use of a diabatic flow pattern map, such as that of Revellin and Thome (2007a) presented earlier, to determine the critical vapor quality and hence the location where the post-dryout heat transfer regime begins with much lower heat transfer coefficients.

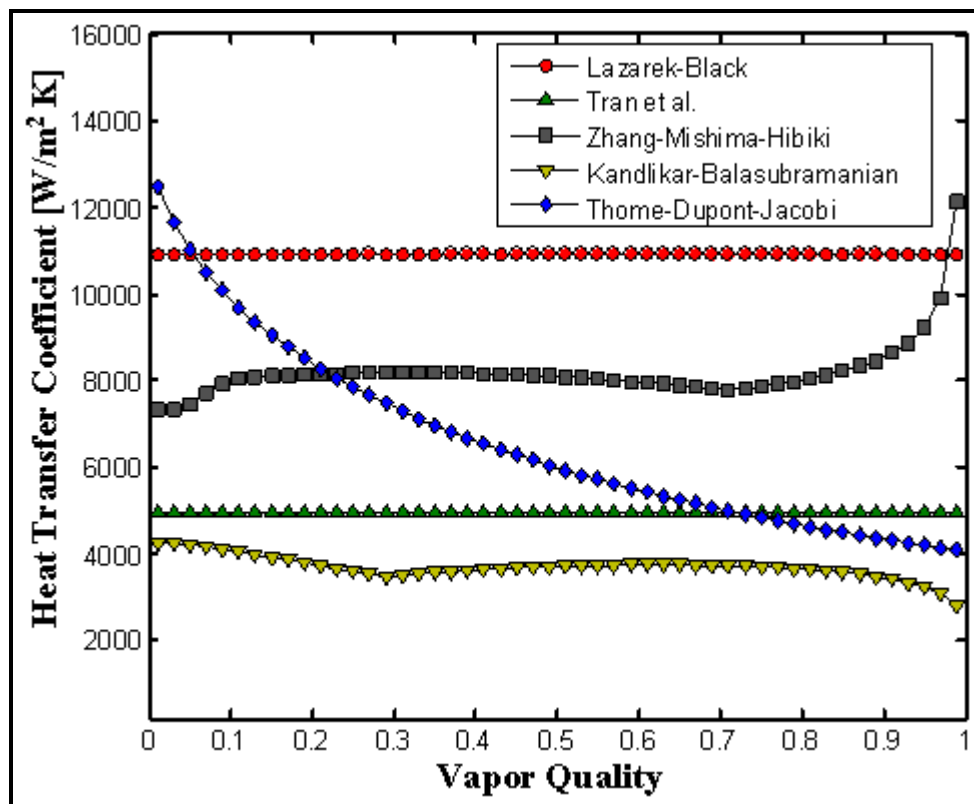


**Figure 20.35. Predicted flow boiling heat transfer trends versus vapor quality for five different methods. Simulation is for R-134a at 7 bar at a heat flux of 50 kW/m<sup>2</sup> and a mass velocity of 500 kg/m<sup>2</sup>s for a 0.5 mm diameter channel.**

In addition, Warriar, Dhir and Momoda (2002) have proposed a flow boiling correlation based on their data for FC-84 boiling inside 5 parallel rectangular channels with a hydraulic diameter of 0.75 mm:



$$\frac{\alpha_{ip}}{\alpha_L} = 1 + 6.0 \text{Bo}^{1/16} + [-5.3(1 - 855 \text{Bo})] x^{0.65} \quad [20.6.14]$$

The single-phase liquid heat transfer coefficient  $\alpha_L$  is calculated from a fully developed flow method like that given above for turbulent flow and Bo is the boiling number. Their method includes a significant effect of vapor quality. Extrapolating this method to the FC-72 and using a developing flow method for  $\alpha_L$  to increase the predicted values, Muwanga and Hassan (2007) found that this method tended to significantly under predict their results for a 1.067 mm diameter channel, although approximately capturing their experimental trends.

Some further comments about the above methods are in order. All of the above *microscale* methods are essentially modifications of *macroscale* flow boiling methods or ideas, and thus assume that nucleate boiling is an important heat transfer mechanism without proof of its existence for the two principal microchannel flow regimes: slug (elongated bubble) flow and annular flow. Furthermore, using a tubular single-phase flow correlation for an annular flow is not physically realistic since convective occurs across the annular liquid film and is thus governed by the film Reynolds number rather than by a tubular Reynolds number *and* by the film thickness rather than the tube diameter. Furthermore, similar to the Nusselt (1916) laminar film condensation model, as long as there are no interfacial waves, the local *laminar* annular flow heat transfer coefficient is dependent on heat conduction across the liquid film and it is thus not appropriate to calculate its value in terms of the tubular solution of  $\text{Nu}_L = 4.36$ , where the film value changes as a function of local thickness while the second one does not.

To put this situation into its proper context, apparently no one applies the *tubular* flow solution to predict laminar falling *film* condensation on a vertical plate so it does not seem to be appropriate to apply it to a laminar annular *film* flow either. For that matter, turbulent falling film condensation on a vertical plate is correlated based on its local liquid film Reynolds number in which the film thickness is the active characteristic dimension (as can be seen in Chapter 7) and hence turbulent annular film evaporation should be correlated in the same manner, not using a *tubular* flow Reynolds number.

Notwithstanding the above comments, wholly empirical methods can usually be fit to experimental databases for prediction purposes. On the other hand, one should remember that because of all the conflicting trends in published data, as illustrated in the diagram by Agostini and Thome (2005) presented earlier, no existing correlation is able to predict all these diverse trends in heat transfer coefficient versus vapor quality.

In part, this problem of numerous diverse trends possibly inadvertently arises because many publications apparently combine stable and unstable boiling results into one common database without segregating the data. To address this issue and the resulting trends, Consolini (2008) has measured local flow boiling data for R-134a, R-245fa and R-236fa at stable conditions and at mildly, medium and highly unstable conditions. Figure 20.36 shows some of his heat transfer results for R-245fa and an example of the pressure trace for the highly unstable case. At the lowest vapor quality, there is no effect of flow instability on the heat transfer coefficient, but with rising vapor quality the stable and mildly unstable data diverge from the medium and highly unstable data completely, resulting in two distinct trends with respect to vapor quality (one rising and one flat). Notably, the trend of no effect of vapor quality on the heat transfer coefficient is found for the significantly unstable flow data. On the other hand, this divergence between stable and unstable data was most evident for their lowest pressure test fluid, R-245fa, while the effect was nearly negligible for the highest pressure fluid, R-134a.



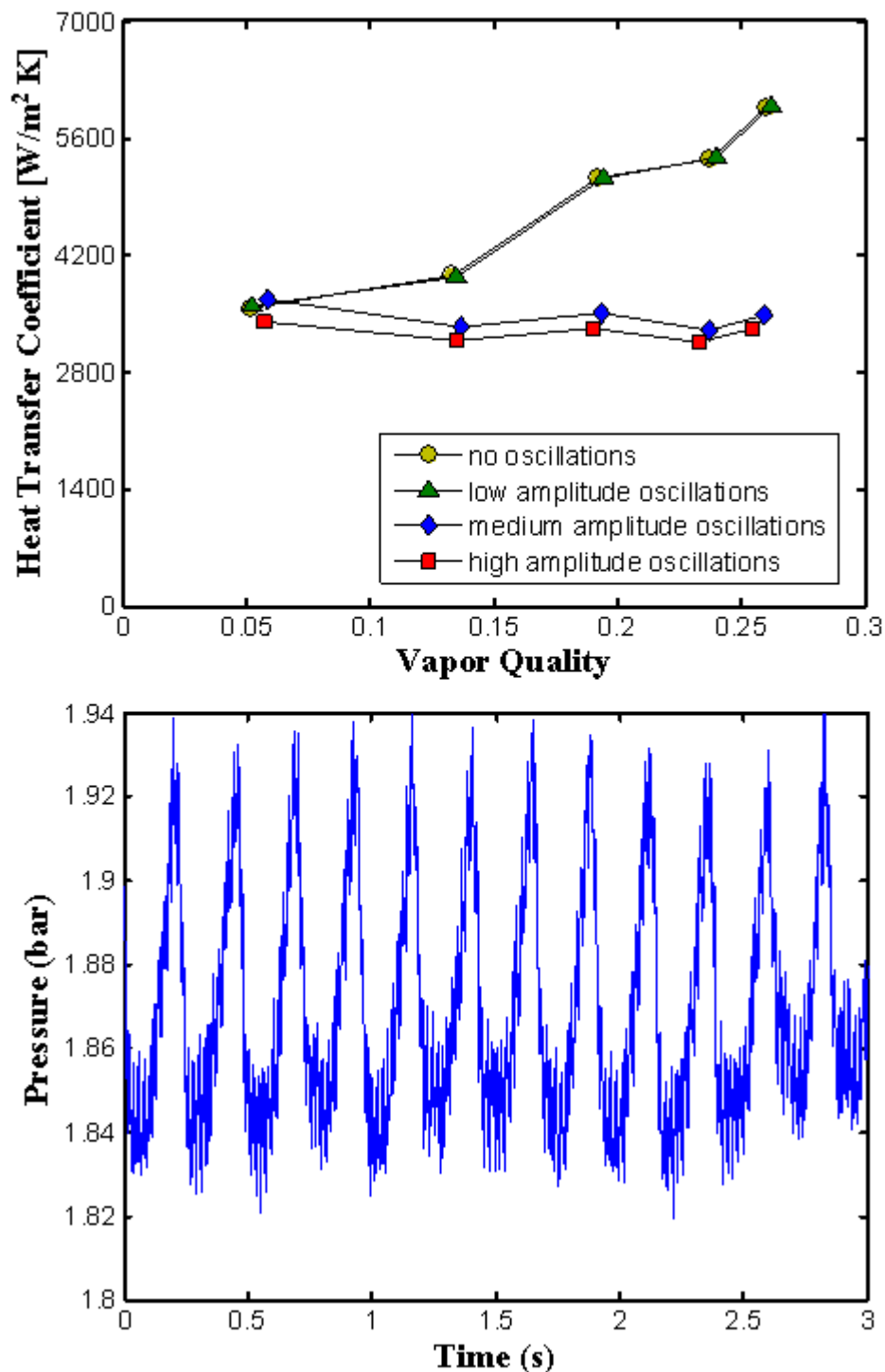


Figure 20.36. Flow boiling data of Consolini (2008) for R-245fa at an inlet temperature of 30°C, an outlet saturation temperature of 32°C, a heat flux of 37 kW/m<sup>2</sup> and a mass velocity of 400 kg/m<sup>2</sup>s in a 0.510 mm diameter channel. *Top*: stable and unstable heat transfer coefficients. *Bottom*: pressure fluctuations measured at the exit of the evaporator test section for a highly unstable flow.

### 20.6.3 Theoretically Based Prediction Methods for Boiling in Microchannels

Jacobi and Thome (2002) proposed a theoretically-based, elongated bubble (slug) flow boiling model for microchannels, modeling the thin film evaporation of the liquid film trapped between these bubbles and the channel wall, and also accounting for the liquid-phase convection in the liquid slugs between the bubbles. The focus of their study was to demonstrate that the thin film evaporation mechanism was the principal heat transfer mechanism controlling heat transfer in slug flows in microchannels, not nucleate boiling as cited in many earlier experimental studies. Specifically, Jacobi and Thome (2002) showed that the thin film heat transfer mechanism along the length of the bubbles was very dominant compared to the liquid convection occurring in the liquid slugs. Furthermore, their thin film evaporation model predicted that  $\alpha_{tp} \sim q^n$ , where the exponent  $n$  depended on the elongated bubble frequency and initial liquid film thickness laid down by the passing bubble. That is, the thin film evaporation heat transfer mechanism, without any local nucleation sites in slug flows, yields the same type of functional dependency as the nucleate boiling curve. Hence, since nucleate boiling in microchannels tends to occur only upstream at or near the onset of boiling (at very low vapor qualities), they concluded that downstream it is the thin film evaporation heat transfer mechanism that dominates boiling in microchannels in the slug flow regime, up until of course the flow regime changes to annular. Thus, this seems to prove that it is not physically logical to manipulate macroscale flow boiling correlations to make them fit microchannel flow boiling data since such models include a nucleate boiling heat transfer dependency rather than a thin film evaporation heat transfer mechanism. On the other hand, macroscale flow boiling correlations and nucleate pool boiling correlations do not actually *model* the physical process of nucleate boiling, they only bring the heat flux dependency of the nucleate boiling process into the method empirically; since the Jacobi-Thome slug flow model shows a strong, direct dependency of  $\alpha_{tp}$  on the bubble frequency in the thin film evaporation process of elongated bubbles, this probably explains why this pseudo-nucleate boiling dependency is incorrectly identified in these earlier papers.

Following this initial work, a three-zone flow boiling model for slug (elongated bubble) flow in microchannels was proposed in a two-part paper by Thome, Dupont and Jacobi (2004) and Dupont, Thome and Jacobi (2004), i.e. an updated version of the prior two-zone model of Jacobi and Thome (2002). Only the three-zone model will be described here in this chapter in detail and the interested reader is referred to the two-zone model paper for its details.

**Description of the three-zone heat transfer model.** Figure 20.37 shows a representation of the three-zone model where  $L_p$  is the total length of the pair or triplet,  $L_L$  is the length of the liquid slug,  $L_G$  is the length of the bubble including the length of the dry wall of the vapor slug  $L_{dry}$ , and  $L_{film}$  is the length of the liquid film trapped by the bubble. The internal radius and the diameter of the tube are  $R$  and  $d_i$  while  $\delta_o$  and  $\delta_{min}$  are respectively the thicknesses of the liquid film trapped between the elongated bubble and the channel wall at its formation and at dry out of the film (only when dryout occurs). The evolution of successive bubbles is shown in the lower diagram. The local vapor quality, heat flux, microchannel internal diameter, mass flow rate and fluid physical properties at the local saturation pressure are input parameters to the model.

The three-zone model predicts the heat transfer coefficient of each zone and the local time-averaged heat transfer coefficient of the cycle at a fixed location along a microchannel during evaporation of an elongated bubble at a constant, uniform heat flux boundary condition. The elongated bubbles grow in axial length, trapping a thin film of liquid between the bubble and the inner tube wall as they flow along the channel. The thickness of this film plays an important role in heat transfer. At a fixed location, the process is assumed to proceed as follows: (i) a liquid slug passes (without any entrained vapor bubbles, contrary to macroscale flows which often have numerous entrained bubbles), (ii) an elongated bubble

passes (whose liquid film is formed from liquid removed from the liquid slug) and (iii) a vapor slug passes, if the thin evaporating film of the bubble dries out before the arrival of the next liquid slug. The cycle then repeats itself upon arrival of the next liquid slug at a frequency  $f_p$  ( $=1/\tau$ ). Thus, a liquid slug and an elongated bubble *pair* or a liquid slug, an elongated bubble and a vapor slug *triplet* pass this fixed point at a frequency  $f_p$ . This frequency is a function of the formation rate of the bubbles upstream, and this frequency is assumed to be constant downstream, i.e. it neglects the coalescence of elongated bubbles into longer, less frequent bubbles. The reader is referred to Chapter 1 where numerous videos of elongated bubble flows at the exit of a micro-evaporator channel are shown, in which these bubble characteristics can be viewed (with the exception of the dry zone after elongated bubbles since the sight glass is adiabatic so the end of the bubble does not dry out in it).

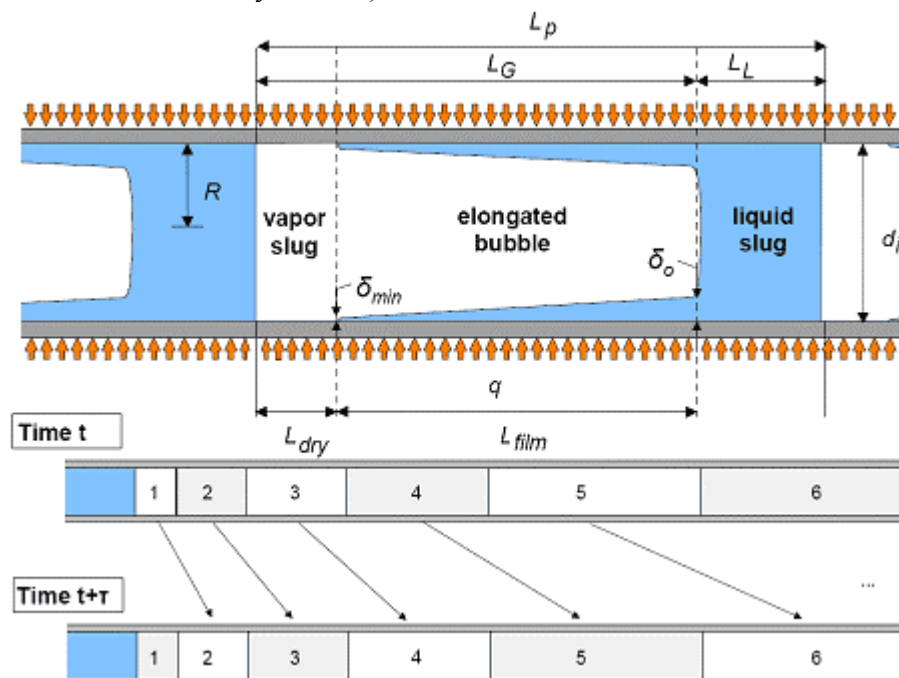


**Figure 20.37. Three-zone heat transfer model of Thome, Dupont and Jacobi (2004) for the elongated bubble flow regime in microchannels. *Top*: Diagram illustrating a triplet comprised of a liquid slug, an elongated bubble and a vapor slug; *bottom*: Bubble tracking of a triplet with passage of a new bubble at time intervals of  $\tau$ .**

In brief, the heat transfer model is formulated as follows. The homogeneous model of two-phase flow is utilized to obtain the void fraction and two-phase velocity along the channel at the desired vapor quality. From the pair (or triplet) frequency, the local length of the pair or triplet in the channel passing by this point is calculated as a function of the vapor quality, which is obtained from an energy balance from the mass flow rate and the uniform heat flux applied to the inner channel wall. The respective lengths of the liquid slug  $L_L$  and vapor  $L_G$  in the pair or triplet are obtained directly from the void fraction at this location, ignoring the small fraction of liquid in the film. Then, from the local mean velocity of the liquid slug, the initial liquid film thickness  $\delta_0$  is calculated and dry out of the wall occurs if the film thickness reaches a predetermined value of  $\delta_{\min}$  before the arrival of the next liquid slug. Mean heat transfer coefficients are determined from the liquid and vapor slugs while the average value of the heat transfer coefficient of the evaporating film is determined from conduction across its varying thickness. The time-averaged heat transfer coefficient is then determined at the local vapor quality for one pair or triplet passing by this location of the channel with respect to the residence time of each process during one time cycle  $\tau$ . The following assumptions were made in developing the model:

1. The flow is assumed to be an elongated bubble (slug) flow.
2. The vapor and liquid travel at the same velocity (homogeneous flow) and the flow is stable.
3. The heat flux is uniform and constant with time along the inner wall of the microchannel.
4. The fluid is saturated liquid at the entrance of the channel with elongated bubbles generated at an as yet unknown frequency  $f_p$ .
5. All energies entering the fluid are used to vaporize liquid such that the temperatures of the liquid and vapor remain at  $T_{\text{sat}}$ , i.e. neither the liquid nor the vapor is superheated.
6. The local saturation pressure is used to determine the local saturation temperature and any flashing effect due to the pressure drop is ignored (but could be included in calculating the variation in  $x$  together with the wall heat flux).
7. The liquid film remains attached to the wall whilst the influence of vapor shear stress on the liquid film is negligible, so that the film remains smooth without ripples.
8. The thickness of the film is very small with respect to the inner radius of the tube:  $\delta_o \ll R$ .
9. The thermal inertia of the channel wall can be neglected during this cyclical heat transfer process.

For the development of the model, the experimental database of the “time-averaged” local heat transfer coefficients were taken from six different laboratories covering seven different fluids (R-11, R-12, R-113, R-123, R-134a, R-141b and  $\text{CO}_2$ ); refer to Dupont, Thome and Jacobi (2004) for the list of studies. All together, they took 1591 test data from the literature which covered channel diameters from 0.77 to 3.1 mm, mass velocities from 50 to 564  $\text{kg/m}^2\text{s}$ , pressures from 1.24 to 57.66 bar, heat fluxes from 5 to 178  $\text{kW/m}^2$ , and vapor qualities from 0.01 to about 0.99. The database included five single channel and two multi-microchannel test setups.

**Bubble formation and frequency.** The model is based on the premise that bubble nucleation occurs at the location where the fluid reaches saturation, that is at  $x = 0$ . In Jacobi and Thome (2002), it was assumed that these small bubbles grew in a uniformly superheated liquid to a diameter equal to the internal diameter of the channel before departing, using the heat diffusion limited model of Plesset and Zwick (1954) in the interest of the simplicity, to obtain the rate of bubble growth:

$$r(t) = \frac{\rho_L c_{pL} \Delta T_{\text{sat}}}{\rho_G h_{LG}} [12a_L t / \pi]^{1/2} \quad [20.6.15]$$

In this expression  $a_L$  is the liquid thermal diffusivity,  $t$  is the bubble growth time and  $\Delta T_{\text{sat}}$  is the wall superheat resulting from the applied heat flux. Thus, each bubble divided the liquid flow into successive pairs or triplets. Assuming the waiting time between successive bubbles was zero, the frequency of bubble departure  $f_p$  and period of pair/triplet generation  $\tau$  was obtained from the bubble growth rate and the internal radius of the tube  $R$  to be:

$$f_p = \frac{1}{\tau} = \left[ \frac{\rho_L c_{pL} \Delta T_{\text{sat}}}{\rho_G h_{LG} R} \right]^2 [12a_L / \pi] \quad [20.6.16]$$

The predicted pair frequency  $f_p$  for R-134a using the above equation at two superheats ( $\Delta T_{\text{sat}} = 1 \text{ K}$  and  $20 \text{ K}$ ), for channel diameters from 0.5 to 2 mm, ranges from over 20 Hz to as low as 0.05 Hz, depending on the diameter of the microchannel, for a variation of up to 400 times! In reality, the shear exerted by the liquid flow in the channel removes the bubble before it blocks the channel and thus a hydrodynamic model is required to predict bubble departure and hence also bubble frequency. As can be seen in some of the videos illustrating bubble nucleation in Chapter 1, the bubbles tend to depart with diameters much smaller than the channel diameter but rapidly grow and coalesce downstream to form elongated bubbles.

In the development of the three-zone model, the values of  $f_p$  are determined (later) from back calculation of the three-zone heat transfer model applied to the experimental flow boiling heat transfer results, and then an empirical method is proposed to predict these values of  $f_p$  as a function of the process variables.

**Basic equations.** The liquid and the vapor are assumed to travel at the same mean velocity in the homogeneous model, so that  $u_L = u_G$ , where:

$$u_G = \frac{\dot{Q}_G}{A\varepsilon} = \frac{\dot{m}}{\rho_G} \left( \frac{x}{\varepsilon} \right) \quad [20.6.17]$$

$$u_L = \frac{\dot{Q}_L}{A(1-\varepsilon)} = \frac{\dot{m}}{\rho_L} \left( \frac{1-x}{1-\varepsilon} \right) \quad [20.6.18]$$

From the equality of these two velocities, the cross-sectional void fraction for homogeneous flow is expressed as a function of vapor quality as:

$$\varepsilon = \frac{1}{1 + \left( \frac{1-x}{x} \right) \frac{\rho_G}{\rho_L}} \quad [20.6.19]$$

The initial conditions assumed are consistent with the homogeneous void fraction model, and in particular the volumetric void fraction is identical to the cross-sectional void fraction in a homogeneous flow.

Since  $u_G = u_L$ , then the velocity of the pair  $u_p$  (or triplet) is:

$$u_p = \dot{m} \left( \frac{x}{\rho_G} + \frac{1-x}{\rho_L} \right) \quad [20.6.20]$$

Since normally  $\rho_L \gg \rho_G$  in the above expression, then the pair (or triplet) velocity varies nearly linearly along the tube and so simplifying:

$$u_p \approx \dot{m} \left( \frac{x}{\rho_G} \right) \quad [20.6.21]$$

At any location along the microchannel, a pair (or triplet) passes during each time period  $\tau$ . It is thus possible to deduce the mean equivalent length of the pair (or triplet)  $L_p$  at any given point using the following expression:

$$L_p = u_p \tau = \tau \dot{m} \left( \frac{x}{\rho_G} + \frac{1-x}{\rho_L} \right) \quad [20.6.22]$$

This is the apparent length of the pair (or triplet) seen by an observer at location  $z$ . To evaluate the residence time of an elongated bubble  $t_G$  at location  $z$  from the entrance (which is assumed to be at saturation with  $x = 0$ ), the equivalent length of the vapor  $L_G$  is calculated using the local void fraction:

$$L_G = \varepsilon L_p = \frac{\tau \dot{m}}{\rho_G} x \quad [20.6.23]$$

The vapor residence time  $t_G$  is thus:

$$t_G = \frac{L_G}{u_p} = \frac{\tau}{1 + \frac{\rho_G}{\rho_L} \frac{1-x}{x}} \quad [20.6.24]$$

This time  $t_G$  corresponds to the period of time that vapor (dryout and elongated bubble zones) passes through the cross section at location  $z$ . Similarly, the equivalent length of the liquid slug  $L_L$  and the liquid residence time  $t_L$  are calculated as follows:

$$L_L = (1 - \varepsilon) L_p = \frac{\tau \dot{m}}{\rho_L} (1 - x) \quad [20.6.25]$$

$$t_L = \frac{L_L}{u_p} = \frac{\tau}{1 + \frac{\rho_L}{\rho_G} \frac{x}{1-x}} \quad [20.6.26]$$

The time  $t_L$  corresponds to the period of time that it takes for the liquid slug to pass through the cross section at location  $z$ . Furthermore, the following relationships hold:  $t_G + t_L = \tau = 1/f_p$  and  $L_G + L_L = L_p$ .

**Liquid film thickness.** The initial thickness of the liquid film  $\delta_o$  at the front of the bubble is a key parameter in the present model. This thickness has a large influence on the thin film evaporation process and thus a relation for predicting the initial thickness of the film  $\delta_o$  is required. For this, Thome, Dupont and Jacobi (2004) modified two film thickness correlations of Moriyama and Inoue (1996), converting their Bond number into a Weber number, to find  $\delta_o$  as a function of the pair velocity  $u_p$ . Moriyama and Inoue (2004) experimentally measured the radial liquid film thickness of bubbles growing between two parallel, heated transparent plates using an indirect technique they developed, comprised of video vapor front tracking and transient wall temperature analysis. The gap between the two plates in their tests ranged from 0.100 to 0.400 mm and the tests were conducted with R-113. They showed that for a large superheat or bubble velocity, the viscous boundary layer controlled the liquid film formation thickness  $\delta_o$  while at a low bubble speed or for a small gap between the plates, the surface tension force was dominant. They proposed an empirical correlation for each mode. In the three-zone model, these two expressions were joined together using an asymptotic expression to the 8<sup>th</sup> power and the expression was converted using some assumptions from its parallel plate geometry to the present circular channel geometry in terms of the present variables (see original paper of the three-zone model for details). Furthermore, the two expressions for  $\delta_o$  of Moriyama and Inoue (2004) were developed only from R-113 tests and the aforementioned range of gaps. Therefore, an empirical correction factor  $C_{\delta_o}$ , whose value was statistically backed out of the heat transfer database using the three-zone model (giving  $C_{\delta_o} = 0.29$ ), was included in the asymptotic initial liquid film thickness model:

$$\frac{\delta_o}{d_i} = C_{\delta_o} \left[ 3 \left( \frac{\mu_L}{\rho_L u_p d_i} \right)^{1/2} \right]^{0.84} \left[ (0.07 We_p^{0.41})^{-8} + 0.1^{-8} \right]^{-1/8} \quad [20.6.27]$$



The Weber number  $We_p$ , which was incorrectly labeled as a Bond number in the paper of Thome, Dupont and Jacobi (2004), in this expression is based on the pair velocity  $u_p$  and channel diameter  $d_i$  as:

$$We_p = \frac{\rho_L d_i u_p^2}{\sigma} \quad [20.6.28]$$

Figure 20.38 shows the predicted variation of the initial thickness of the liquid film for R-113 at a saturation temperature of 47.2°C in terms of the pair velocity for two microchannel diameters according to this method. The values of  $\delta_o$  range from 2.1 to 6.1 microns for pair velocities from 0.5 to 1.0 m/s, which is the same order of magnitude as those measured by Moriyama and Inoue (1996) for R-113 for small gaps (0.1 to 0.4 mm) for the corresponding range of velocity.

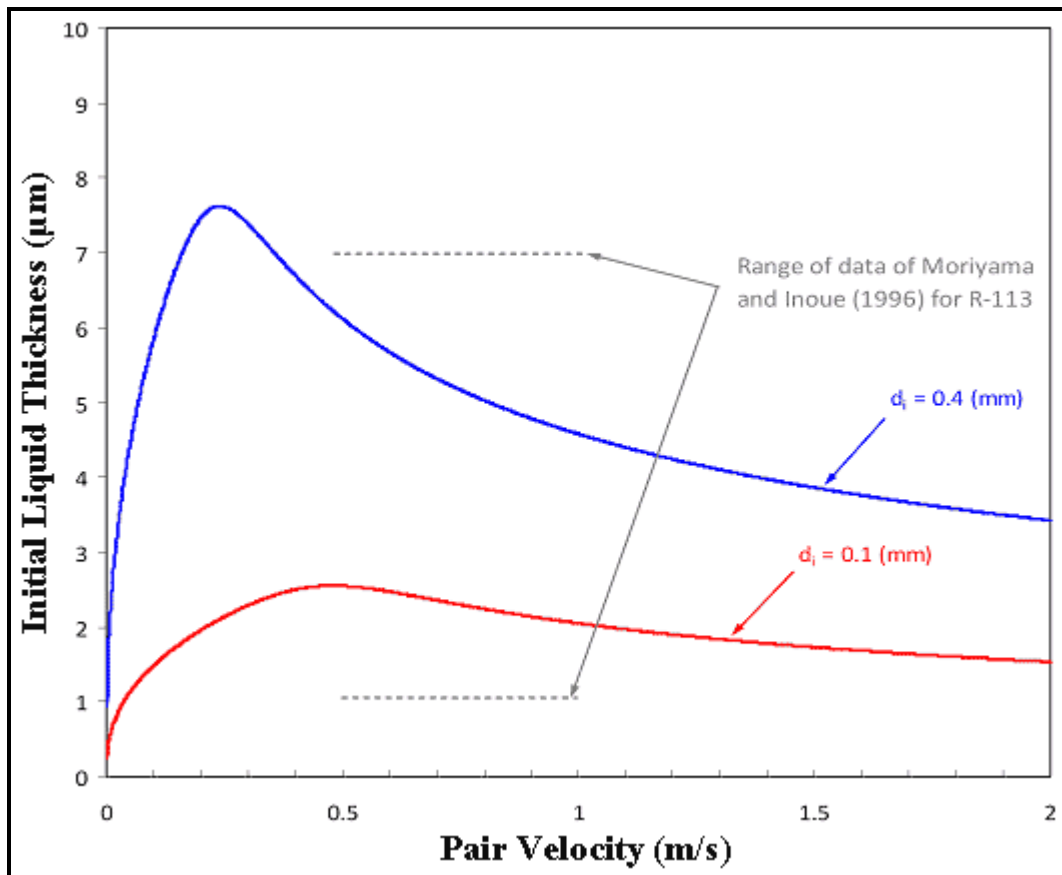


**Figure 20.38. Predicted thickness of the initial liquid film  $\delta_o$  as a function of bubble pair velocity for R-113 with  $C_{\delta o}$  set equal to 1.0. The maximum and minimum values of  $\delta_o$  measured by Moriyama and Inoue (1996) between two parallel plates of the same gap size are indicated by the dashed lines.**

The variation of the liquid film thickness from its initial value of  $\delta_o$  due to vaporization by the uniform heat flux  $q$  at the inner wall of the tube is obtainable from an energy balance over a differential length of the film  $dz$ , assuming all the energy transferred by conduction from the wall is used to vaporize the liquid. The rate of latent heat transfer depends on the rate of evaporation of the liquid phase,  $dM_l/dt$ , and hence from the assumption that  $\delta \ll R$  for an annular film, this is:

$$Q = -\frac{dM_L}{dt} h_{LG} = -\rho_L 2\pi(R - \delta) \frac{d\delta}{dt} dz h_{LG} \quad [20.6.29]$$

The heat dissipated from the wall is:

$$Q = q(2\pi R dz) \quad [20.6.30]$$

Equating these two expressions and solving for the variation in the film thickness gives:

$$d\delta = -\frac{q}{\rho_L h_{LG}} \frac{R}{R - \delta} dt \quad [20.6.31]$$

Again, from assumption that  $\delta \ll R$ , we see that  $R - \delta \approx R$ . The time reference is defined so that time  $t = 0$  corresponds to the instant when the film is created at position  $z$ . Integration of the above expression with the initial condition  $\delta(z, 0) = \delta_0(z)$  results in:

$$\delta(z, t) = \delta_0(z) - \frac{q}{\rho_L h_{LG}} t \quad [20.6.32]$$

The value of  $\delta_0(z)$  is obtained with the asymptotic expression above. From this relation, the maximum duration of the film  $t_{\text{dry film}}$  at position  $z$  is obtained in terms of the minimum thickness at dryout  $\delta_{\min}$  to be:

$$t_{\text{dry film}}(z) = \frac{\rho_L h_{LG}}{q} [\delta_0(z) - \delta_{\min}] \quad [20.6.33]$$

The actual final film thickness  $\delta_{\text{end}}$  and residence time of the film  $t_{\text{film}}$  depend on whether or not the film dries out. If  $t_{\text{dry film}} > t_G$ , then the next liquid slug arrives before dryout occurs, so that:

$$\delta_{\text{end}}(z) = \delta(z, t_G) \quad [20.6.34]$$

$$t_{\text{film}} = t_G \quad [20.6.35]$$

If  $t_{\text{dry film}} < t_G$ , then local dryout occurs when the liquid film thickness reaches the minimum feasible film thickness  $\delta_{\min}$ , so that:

$$\delta_{\text{end}}(z) = \delta_{\min} \quad [20.6.36]$$

$$t_{\text{film}} = t_{\text{dry film}} \quad [20.6.37]$$

In this case, the time duration that the local wall is dry is  $t_{\text{dry}}$ :

$$t_{\text{dry}} = t_G - t_{\text{film}} \quad [20.6.38]$$

From this time period and the velocity of the pair, the equivalent length of the dry zone at the location  $z$  is:

$$L_{\text{dry}} = u_p t_{\text{dry}} \quad [20.6.39]$$

The minimum film thickness at dryout  $\delta_{\min}$  is physically related to the roughness of the surface (if known, but not usually cited in most microchannel flow boiling papers), the thermo-physical properties of the fluid, the contact angle between the vapor, liquid and wall, and the local hydrodynamics of the flow. To obtain its value is beyond current modeling capabilities and thus a fixed empirical value for  $\delta_{\min}$  was statistically backed out of the heat transfer database using the three-zone model (giving  $\delta_{\min} = 0.0000003 \text{ m} = 0.3 \text{ }\mu\text{m}$ ).

**Heat transfer model.** Now that the flow parameters have been derived, the heat transfer coefficient in each zone (liquid slug, elongated bubble and vapor slug) is analyzed. The time-averaged local heat transfer coefficient  $\alpha_{\text{film}}$  in the evaporating liquid film between the elongated bubble and the wall, assuming that the thin liquid film is stagnant and heat transfer is controlled only by one-dimensional conduction across the film, is given by the following integral:

$$\alpha_{\text{film}}(z) = \frac{1}{t_{\text{film}}} \int_0^{t_{\text{film}}} \frac{k_L}{\delta(z, t)} dt \quad [20.6.40]$$

Integrating over the time period of the passage of the bubble, this yields:

$$\alpha_{\text{film}}(z) = \frac{k_L}{\delta_o - \delta_{\text{end}}} \ln \left( \frac{\delta_o}{\delta_{\text{end}}} \right) \quad [20.6.41]$$

The value of  $\delta_{\min}$  is assumed to be nonzero and of the same order of magnitude as the surface roughness, whose value however is not usually cited in published data sources. Because of the complexity in predicting the finite thickness of this very thin layer, the minimum film thickness  $\delta_{\min}$  was taken as one of the three adjustable parameters in the three-zone model (along with  $f_p$  and  $C_{\delta_o}$ ) that were determined statistically from comparison of the model to their experimental heat transfer database of seven fluids from six different laboratories.

The heat transfer coefficients for the liquid and vapor slugs (the latter only when intermittent dryout has been reached) are calculated from their respective local Nusselt numbers. These values are then applied to the respective equivalent lengths of the liquid slug  $L_L$  and dry wall zone  $L_{\text{dry}}$  passing by a given location  $z$ . The local Nusselt number at this location is assumed to be hydrodynamically and thermally developing. For laminar developing flow, for which  $Re \leq 2300$ , the London and Shah correlation given by the VDI (1997) is used to obtain the local tubular flow Nusselt number ( $Nu = \alpha d_i/k$ ):

$$Nu_{\text{lam}}(z) = 0.455 \sqrt[3]{Pr} \left( \frac{d_i Re}{L(z)} \right)^{1/2} \quad [20.6.42]$$

The averaged value over the length  $z$ , using the liquid slug of length  $L_L$  or vapor slug of  $L_{\text{dry}}$  for  $L(z)$ , gives:

$$Nu_{\text{lam},z} = 2 Nu_{\text{lam}}(z) \quad [20.6.43]$$

For transition and turbulent developing flows, the Gnielinski (1976) correlation given by the VDI (1997) is assumed to be valid for  $Re > 2300$  so that the local Nusselt number is:

$$\text{Nu}_{\text{turb}}(z) = \frac{(f/2)(\text{Re}-1000)\text{Pr}}{1 + 12.7\sqrt{f/2}(\text{Pr}^{2/3}-1)} \left[ 1 + \frac{1}{3} \left( \frac{d_i}{L(z)} \right)^{2/3} \right] \quad [20.6.44]$$

The friction coefficient  $f$  is:

$$f = (1.58 \ln \text{Re} - 3.28)^{-2} \quad [20.6.45]$$

Again using the liquid slug of length  $L_L$  or vapor slug of  $L_{\text{dry}}$  for  $L(z)$ , the averaged value on  $z$  is obtained from:

$$\text{Nu}_{\text{turb},z} = \frac{(f/2)(\text{Re}-1000)\text{Pr}}{1 + 12.7\sqrt{f/2}(\text{Pr}^{2/3}-1)} \left[ 1 + \left( \frac{d_i}{L(z)} \right)^{2/3} \right] \quad [20.6.46]$$

The respective properties of the saturated liquid and vapor are used in implementing these expressions and the Reynolds number  $\text{Re}$  of the particular phase is obtained using the channel diameter  $d_i$ , the local pair velocity  $u_p$ , and the dynamic viscosity of that phase:

$$\text{Re} = \frac{\rho u_p d_i}{\mu} \quad [20.6.47]$$

To avoid the jump in the value of the Nusselt number at  $\text{Re} = 2300$ , a continuous expression of the mean convective heat transfer coefficient as a function of Reynolds number was obtained by applying a 4<sup>th</sup> power asymptotic expression as follows:

$$\alpha_{\text{slug}} = [\alpha_{\text{lam}}^4 + \alpha_{\text{turb}}^4]^{1/4} = \frac{k}{d_i} [\text{Nu}_{\text{lam}}^4 + \text{Nu}_{\text{turb}}^4]^{1/4} \quad [20.6.48]$$

These expressions are applicable to the liquid in the slug and to the vapor in the dry zone for their respective equivalent lengths,  $L_L$  and  $L_{\text{dry}}$ .

Finally, from these three zonal heat transfer coefficients, the time-averaged local heat transfer coefficient  $\alpha_{\text{tp}}$  is calculated over one time period  $\tau$ , which is the value actually reported in flow boiling experiments. The local, time-averaged heat transfer coefficient of a pair (or triplet) passing by location  $z$  is:

$$\alpha_{\text{tp}} = \frac{t_L}{\tau} \alpha_{\text{slug},L}(z) + \frac{t_{\text{film}}}{\tau} \alpha_{\text{film}}(z) + \frac{t_{\text{dry}}}{\tau} \alpha_{\text{slug},G}(z) \quad [20.6.49]$$

**Adjustable parameters.** The three-zone model has three adjustable parameters, all of which are difficult to predict theoretically. They are:

$\delta_{\text{min}}$ : the minimum thickness of the liquid film at dryout, which is related to the often unknown roughness of the surface, the thermo-physical properties of the fluid and the hydrodynamics of the flow (but should be similar in value to the surface roughness as a first estimate when available);

$C_{\delta_0}$ : the correction factor on the prediction of  $\delta_0$ , which takes into account the difference between the fluids and the geometries in the present database compared to the original R-113 tests used to establish the current asymptotic prediction method;

$f_p$ : the pair (or triplet) frequency is a complex function of the bubble formation and coalescence process, and is influenced by the diameter of the channel, its surface roughness, the nucleation process, the bubble departure dynamics, the coalescence dynamics, etc.

A search for the optimum values of the parameters  $f_p$ ,  $C_{\delta_0}$  and  $\delta_{\min}$  was performed in part two of their study, in Dupont, Thome and Jacobi (2004). This was done by applying the above three-zone model to each individual series of local boiling data points of their entire database to find the optimum values of  $f_p$ ,  $C_{\delta_0}$  and  $\delta_{\min}$  for each individual set of data. Once the set of optimum values for all the series were determined, they were then used as the databases for  $f_p$ ,  $C_{\delta_0}$  and  $\delta_{\min}$  to develop the general methods for their prediction, which are presented below.

The optimum values of the identified pair frequency  $f_p$  were found to be strongly dependent on the heat flux while no clear dependency on any other parameter was identified. In fact, plotting the identified pair frequencies versus the heat fluxes for each series in the database (such a graph is presented in part 2 of that study), nearly parallel lines for each fluid in each study were found on a log-log basis. Thus, the following power law expression was found to give the best fit to these experimentally extracted values:

$$f_p = \frac{1}{\tau} = \left( \frac{q}{q_0} \right)^{1.74} \quad [20.6.50]$$

This empirical dimensional expression has the units of Hz while the values of  $q$  and  $q_0$  are input in  $W/m^2$ . The pair frequency was surmised to be a function of the fluid physical properties since the log-log plots of  $f_p$  vs.  $q$  gave nearly parallel lines for the seven test fluids as noted above. A reduced pressure relation brought the effect of the physical properties of the fluid into the expression via the reference heat flux,  $q_0$  as:

$$q_0 = 3328 \left( \frac{p_{\text{sat}}}{p_{\text{crit}}} \right)^{-0.5} = 3328 p_r^{-0.5} \quad [20.6.51]$$

Thus, these equations permit the pair (or triplet) frequency to be calculated from the local heat flux and the local saturation conditions of the particular fluid in a general manner. Notably, even though the model has been developed for a uniform heat flux  $q$  along the channel and around its circumference, since the model is local and based on local energy balances, it is possible implement the model for non-uniform axial heat fluxes.

The individual extracted values of the correction factor  $C_{\delta_0}$  from all the series of experimental tests in the database ranged from 0.34 to 1.23 with the mean correction factor equal to 0.84 with a standard deviation of 0.28. This mean value of the correction factor near unity gave an encouraging sign of the validity of the expression for  $\delta_0$ . However, the best value for  $C_{\delta_0}$  is 0.29 when statistically evaluating all of the database, rather than the individual series, and this is the value to use when applying the three-zone model.

The identification of the minimum film thickness  $\delta_{\min}$  from the database using the logarithmic expression above for  $\alpha_{\text{film}}(z)$  was very difficult due to the very sensitive impact of  $\delta_{\min}$  when its value tends to zero and thus that of  $\alpha_{\text{film}}(z)$  tends to infinity. In order to reduce the sensitivity of the model to  $\delta_{\min}$ , the mean

heat transfer coefficient in the film is calculated instead by using the average value of the film thickness as follows:

$$\alpha_{\text{film}}(z) = \frac{2k_L}{\delta_o(z) - \delta_{\text{min}}(z)} \quad [20.6.52]$$

This expression is thus used in place of the logarithmic expression presented above when implementing the three-zone model. Considering all the studies, the specific values of  $\delta_{\text{min}}$  backed out of the individual experimental series ranged from about 0.01 to 3.0  $\mu\text{m}$ , while overall statistically the best value was  $\delta_{\text{min}}$  equal to 0.0000003 m (0.3  $\mu\text{m}$ ) and this is the value to use in the model. However, one can use the surface roughness of the channel in place of this value when known.

The three-zone model, using these empirical values, predicted 67% of their total database to within  $\pm 30\%$  while capturing 83% of the single-channel database within that range. Their elongated bubble (slug flow) model was developed using the entire heat transfer database, thus inevitably including bubbly flow and annular flow heat transfer data within their analysis, as no proven method was available at that time to select only slug flow heat transfer data points. In particular, and perhaps most importantly at this point, the three-zone model illustrates the importance of the strong cyclic variation in the heat transfer coefficient in the elongated bubble flow regime and the strong influence of heat transfer on: (i) the bubble frequency, (ii) the minimum liquid film thickness at dryout and (iii) the initial liquid film formation thickness. It thus, in a sense, provides a physically based guideline for what parameters should be measured in future flow boiling experiments, in addition to the time-averaged local heat transfer coefficients, in order to better understand the fundamentals of the elongated bubble heat transfer process.

**Independent comparisons to the three-zone model.** The three-zone model has been compared in some publications to new experimental data sets since its development. For instance, Shiferaw, Karayiannis and Kenning (2006) measured local flow boiling data for R-134a in a 2.01 mm stainless steel tube at 8 bar. The three-zone model predicted most of their data within  $\pm 20\%$ , irrespective of flow regime, while their other data at 12.0 bar were less well predicted, yielding a spread of  $\pm 30\%$  while showing a tendency to under predict with increasing pressure.

Agostini et al. (2008b) compared their multi-microchannel database obtained in collaboration with IBM to selected methods. Their test section was a silicon heat sink made with 67 parallel, high aspect ratio, rectangular channels that were 0.223 mm wide, 0.680 mm high and 20.0 mm long with 0.080 mm fins between the channels. Utilizing only the data at vapor qualities above 5% to eliminate the inlet effects of the 90° turn in the flow and the orifice at the entrance to the channels, their database used for the comparison consisted of 1438 data points for R-245fa and R-236fa and accounted for the fin efficiency effects. The three-zone model using the measured surface roughness (0.17  $\mu\text{m}$  for their silicon channels) in place of the original value of 0.3  $\mu\text{m}$  predicted 90% of these data within  $\pm 30\%$  (only 31% were predicted within  $\pm 30\%$  using the original value, just to indicate the sensitivity of the surface roughness in the model and on the heat transfer process). The Kandlikar and Balasubramanian (2004) correlation captured 58% and the Zhang, Hibiki and Mishima (2004) correlation yielded 19% of the data within  $\pm 30\%$ .

In contrast, the measured local flow boiling heat transfer coefficients of Agostini et al. (2008d) for R-236fa in a silicon test section with 134 parallel, rectangular channels that were 0.067 mm wide and 0.680 mm high with fins 0.092 mm thick with one central inlet and two outlets to each side were not predicted well by the three-zone model, even using the measured surface roughness of 0.160  $\mu\text{m}$  in place of the original value of 0.3  $\mu\text{m}$ . This was apparently because of the significant influences of the jet created by the inlet orifice at the center of each channel and the recirculation created on these short channels (10 mm



to each side of the inlet) with 90° bends in the flow at the inlet and outlet, effects which are not accounted for in the three-zone model.

Consolini (2008) compared his extensive database for R-134a, R-236fa and R-245fa for stable flow conditions for 0.510 and 0.790 mm stainless steel test sections at near ambient saturation temperatures to five of the methods presented in this chapter. Using the Revellin and Thome (2007a) diabatic flow pattern map described earlier in this chapter to eliminate the annular flow data from the comparison (that is keeping only the data identified to be in the IB and CB regimes), he found that 77% of these data were predicted within  $\pm 30\%$  by the three-zone model (but still including the bubble flow data). Excluding the bubble flow data at low vapor qualities, the accuracy would have improved. In comparison, the Lazarek and Black (1982) correlation surprisingly captured 88% of the entire database within  $\pm 30\%$  while the Tran, Wambsganss and France (1996) correlation captured only 4% within this range, Kandlikar and Balasubramanian (2004) correlation captured 21% and the Zhang, Hibiki and Mishima (2004) correlation yielded 58%.

The three-zone model has so far been successfully compared to about a dozen fluids (not all in published comparisons) for data taken by nearly as many independent laboratories. Even so, it is clear that the three-zone model sometimes gives reasonably accurate predictions of independent data while sometimes it does not. Not surprisingly, it seems to significantly under predict data at very low vapor qualities where the flow regime is bubbly flow and apparently nucleate boiling is the controlling heat transfer mechanism. Furthermore, it does not apparently capture the effect of microchannel tube diameter correctly. On the other hand, this is a first generation mechanistic model for boiling in microchannels and hence one that requires further refinement. Using the [Databook III Calculator](#) within this book, the reader can simulate predictions of the three-zone model for specific applications or compare the model to new experimental test data. To improve its prediction for a specific fluid for a specific application when such data is available, the user can also play with one or all of the values of the three empirical factors within the Excel code itself or, for instance, set the minimum film thickness to the surface roughness when known.

## 20.7 Two-Phase Pressure Drops in Microchannels

The two principle approaches to predict frictional pressure gradients in microscale two-phase flow are the homogeneous and the separated flow models. The homogenous model assumes that the two-phase fluid behaves as a single-phase fluid but pseudo-properties are used for the density and viscosity that are weighted relative to the vapor and liquid flow fractions. Instead, the separated flow model considers that the phases are artificially segregated into two separate streams, one liquid and one vapor, and interact through their common interface. Refer to Chapter 13 for the basic equations governing two-phase pressure drops and for a detailed discussion of two-phase friction factor prediction methods for macroscale flows.

### 20.7.1 Homogeneous Model Applied to Microchannels

The two-phase frictional pressure drop assuming homogeneous flow is calculated from the single-phase pressure drop correlation using a two-phase friction factor determined using the properties of the vapor-liquid mixture. For adiabatic flows ( $x = \text{constant}$ ), the homogeneous flow model begins from the following expression:

$$\Delta p_{\text{frict}} = \frac{2f_{\text{tp}} L \dot{m}^2}{d_i \rho_{\text{tp}}} \quad [20.7.1]$$

In this expression,  $f_{tp}$  is the two-phase friction factor. The total mass velocity is used in the calculation while also  $\rho_{tp}$  is the homogeneous density of the fluid,  $L$  is the length of the channel and  $d_i$  is its internal diameter. For diabatic flows, the homogeneous model is applied using the change of vapor quality  $\Delta x$  in the calculation as follows:

$$\Delta p_{frict} = \frac{2f_{tp} L \dot{m}^2}{d_i \rho_{tp}} \left[ 1 + \frac{\Delta x}{2} \frac{\rho_G}{\rho_L - \rho_G} \right] \quad [20.7.2]$$

The turbulent friction factor may be expressed in terms of the Reynolds number by the Blasius equation when  $Re \geq 2000$ :

$$f_{tp} = \frac{0.079}{Re^{0.25}} \quad [20.7.3]$$

When the flow is laminar for  $Re < 2000$ , then the laminar friction factor expression is used:

$$f_{tp} = \frac{16}{Re} \quad [20.7.4]$$

The Reynolds number is defined as:

$$Re = \frac{\dot{m} d_i}{\mu_{tp}}$$

[20.7.5]

Different ways to define these pseudo-properties (density and viscosity) have been proposed in the literature and are well detailed in Collier and Thome (1994). The homogeneous density is normally calculated using the following mixing law:

$$\rho_{tp} = \left( \frac{x}{\rho_G} + \frac{1-x}{\rho_L} \right)^{-1} \quad [20.7.6]$$

Then, one of the following three mixing laws is used to obtain the homogeneous dynamic viscosity  $\mu_{tp}$ :

$$\text{McAdams, Woods and Bryan (1942):} \quad \mu_{tp} = \left( \frac{x}{\mu_G} + \frac{1-x}{\mu_L} \right)^{-1} \quad [20.7.7]$$

$$\text{Cicchitti et al. (1960):} \quad \mu_{tp} = x\mu_G + (1-x)\mu_L \quad [20.7.8]$$

$$\text{Dukler, Wicks and Cleveland (1964):} \quad \mu_{tp} = \rho_{tp} \left[ x \frac{\mu_G}{\rho_g} + (1-x) \frac{\mu_L}{\rho_L} \right] \quad [20.7.9]$$

The last expression uses the expression above to calculate  $\rho_{tp}$ .

Various studies have shown that the homogeneous model is a relatively good first choice for calculating two-phase pressure drops in microchannels. Based on their database of 913 data points from 9 independent studies, Ribatski, Wojtan and Thome (2006) found that the homogeneous model, using the above definition of the homogeneous density and the homogeneous viscosity expression of Cicchitti et al. (1960), predicted 54.3% of the data to within  $\pm 30\%$  with a mean absolute error of 61.6%. This was the highest success rate within  $\pm 30\%$  of all the twelve macroscale and microscale methods compared to their database. The macroscale method of Müller-Steinhagen and Heck (1986) came in second with 53.1% of the data points within  $\pm 30\%$  with a mean absolute error of 31.3%, and was regarded as the better method. Meanwhile, the Mishima and Hibiki (1996) small channel correlation, to be presented below, had the second best mean absolute error in that study (37.4%) with 47.7% of the database within  $\pm 30\%$ . The Müller-Steinhagen and Heck (1986) prediction method is described in Chapter 13 of this book and the interested reader is referred there.

Revellin and Thome (2007b) obtained 2210 two-phase pressure drop data points for 0.790 and 0.509 mm glass channels at the exit of a micro-evaporator for R-134a and R-245fa, deducing the fall in pressure drop from the fall in the saturation temperature measured using thermocouples, so as to not disturb the flow with pressure taps. Only a few data were obtained in the laminar regime ( $Re < 2000$ ) whilst no method in the literature was able to predict their large database located in the intermediate range ( $2000 < Re < 8000$ ). For their data in the turbulent regime (1200 points for  $Re > 8000$ ), the McAdams, Woods and Bryan (1942) homogeneous model was not accurate whereas the homogeneous model using the viscosity expression of Cicchitti et al. (1960) worked better (predicting 52% of the database within  $\pm 20\%$  while the McAdams expression only achieved 6%), although the Cicchitti et al. expression still tended to systematically under predict the turbulent flow data. On the other hand, the separated flow correlation of Müller-Steinhagen and Heck (1986) worked best, considering again only the turbulent database, and predicted 62% of the database within  $\pm 20\%$ .

In summary, the prediction of two-phase pressure drops of air-water and refrigerants using the homogeneous model is only approximately reliable, and then apparently only for turbulent flows. Of these methods, the Cicchitti et al. (1960) viscosity expression works best. At least one macroscale method, that of Müller-Steinhagen and Heck (1986), gives better results, although the desired level of accuracy and reliability for engineering design is still quite elusive.

## 20.7.2 Separated Flow Models Applied to Microchannels

In the separated flow model's simplest form, each stream is assumed to travel at its own mean velocity. The separated flow model has been continuously developed since 1949 when Lockhart and Martinelli (1949) published their classic paper on two-phase, gas-liquid flow. The main goal in this approach is to find an empirical correlation or simplified concept to relate the two-phase friction multiplier,  $\Phi^2$ , to the independent variables of the flow, where the two-phase friction multiplier is then applied to the single-phase pressure drop to find the two-phase value. The Lockhart and Martinelli approach, as generalized by Chisholm (1967), gives an expression for  $\Phi^2$  as follows:

$$\Phi^2 = 1 + \frac{C}{X} + \frac{1}{X^2} \quad [20.7.10]$$

where  $C$  depends on the flow regime of each phase (laminar or turbulent), see Table 20.1. The Martinelli parameter  $X$  is given by the square root of the single-phase ratio of the liquid phase to gas or vapor phase frictional pressure drops:

$$X = \left[ \frac{(dp/dz)_L}{(dp/dz)_G} \right]^{1/2} \quad [20.7.11]$$

The frictional pressure drop of the two-phase flow is calculated as:

$$\Delta p_{\text{frict}} = \Delta p_L \Phi^2 \quad [20.7.12]$$

The pressure drop  $\Delta p_L$  is calculated for an all liquid-phase flow, assuming the total flow of liquid and vapor is liquid, so that:

$$\Delta p_L = 4f_L (L/d_i) \dot{m}^2 (1/2\rho_L) \quad [20.7.13]$$

The friction factor equations cited above are used to obtain the friction factor  $f_L$  using the total mass velocity in calculating the liquid Reynolds number.

**Table 20.1. Conventional values of C given by Chisholm (1967).**

Liquid	Gas	C
Turbulent	Turbulent	20
Laminar	Turbulent	12
Turbulent	Laminar	10
Laminar	Laminar	5

Many of the microchannel frictional pressure drop methods have modified this approach by determining a new value of C fit to their data or by implementing an additional correlation for the prediction of the value of C. Applying this first approach, Lazarek and Black (1982) obtained good predictions of their data by using a value of  $C = 30$  in the generalized Chisholm/Lockhart-Martinelli correlation.

Mishima and Hibiki (1996) obtained pressure drop data for small channels ranging in size from about 1.05 to 3.90 mm for air/water flows and fit their data by correlating the Chisholm C parameter in the Lockhart-Martinelli correlation as a function of the tube diameter as follows

$$C = 21 \left( 1 - e^{-0.319d_i} \right) \quad [20.7.14]$$

where the diameter  $d_i$  is input in millimeters. They showed that this method worked for different fluids and for channel diameters from about 0.2 to 25.0 mm. As noted earlier, this method came in within the top 2 to 3 methods in comparisons to an independent database by Ribatski, Wojtan and Thome (2006). This method, however, performed poorly when compared to the Revellin and Thome (2007b) refrigerant database for R-134a and R-245fa for turbulent microchannel flows.

Lee and Lee (2001) have proposed the following empirical approach for calculating C:

$$C = A \lambda^q \phi^R \text{Re}_L^S \quad [20.7.15]$$

The liquid and Reynolds numbers used in this method are defined as:

$$Re_L = \frac{\dot{m}d_i}{\mu_L} \quad [20.7.16]$$

$$Re_G = \frac{\dot{m}d_i}{\mu_G} \quad [20.7.17]$$

The other two parameters in this expression are calculated as follows:

$$\lambda = \frac{\mu_L^2}{\rho_L \sigma d_i} \quad [20.7.18]$$

$$\phi = \frac{\mu_L U}{\sigma} \quad [20.7.19]$$

The superficial velocity  $U$  is given by:

$$U = U_G + U_L \quad [20.7.20]$$

The superficial velocity of the vapor  $U_G$  and the superficial velocity of the liquid  $U_L$  are defined as:

$$U_G = \frac{\dot{Q}_G}{A} = \frac{\dot{m}x}{\rho_G} \quad [20.7.21]$$

and

$$U_L = \frac{\dot{Q}_L}{A} = \frac{\dot{m}(1-x)}{\rho_L} \quad [20.7.22]$$

The empirical constants  $A$ ,  $q$ ,  $R$  and  $S$  are given in Table 20.2 for their method together with the ranges of  $X$  and  $Re_L$  covered in their database. For the choice of the flow regime, it is taken as laminar when  $Re_L$  or  $Re_G < 2000$  and turbulent when  $Re_L$  or  $Re_G > 2000$ .

**Table 20.2. Empirical constants of Lee and Lee (2001) method.**

Flow Regime Liquid	Flow Regime Gas	A	q	R	S	Range of X	Range of $Re_L$
Laminar	Laminar	$6.833 \times 10^{-8}$	-1.317	0.719	0.557	0.776-14.176	175-1480
Laminar	Turbulent	$6.185 \times 10^{-2}$	0	0	0.726	0.303-1.426	293-1506
Turbulent	Laminar	3.627	0	0	0.174	3.276-79.415	2606-17642
Turbulent	Turbulent	0.408	0	0	0.451	1.309-14.781	2675-17757

Lee and Mudawar (2005) measured two-phase pressure drops for a multi-microchannel heat sink under evaporation conditions. Their microchannels were 0.231 mm wide and 0.713 mm deep. Tests were done for R-134a and for water in a prior study. They proposed two expressions for obtaining the value of  $C$  for the generalized Chisholm/Lockhart-Martinelli correlation:

$$C_{\text{lam, lam}} = 2.16 \text{Re}_L^{0.047} \text{We}_{d_i}^{0.6} \quad [20.7.23]$$

$$C_{\text{lam, turb}} = 1.45 \text{Re}_L^{0.25} \text{We}_{d_i}^{0.23} \quad [20.7.24]$$

The value of  $\text{Re}_L$  is the same definition used above in Lee and Lee (2001) method and the value of liquid Weber number based on the tube diameter is obtained from:

$$\text{We}_{d_i} = \frac{\dot{m}^2 d_i}{\rho_L \sigma} \quad [20.7.25]$$

Several other empirical methods not based on the Chisholm/Lockhart-Martinelli correlation have been proposed. Using their experimental database, Yan and Lin (1998) proposed an empirical correlation to predict the two-phase friction factor. This correlation was corrected by Yan and Lin (2003) after Webb and Paek (2003) showed in a letter to the editors that the data and the correlation did not match in their paper. The corrected version for calculating the two-phase friction factor is:

$$f_{tp} = 0.127 \text{Re}_{\text{eq}}^{-0.1923} \quad [20.7.26]$$

This value is applied to [20.7.1] to calculate the pressure drop.  $\text{Re}_{\text{eq}}$  is the same equivalent Reynolds number proposed by Akers, Deans and Crosser (1959) in their convective condensation correlation:

$$\text{Re}_{\text{eq}} = \frac{\dot{m} d_i}{\mu_L} \left[ (1-x) + x \left( \frac{\rho_L}{\rho_G} \right)^{0.5} \right] \quad [20.7.27]$$

Tran et al. (2000) proposed the following correlation for the two-phase multiplier:

$$\Phi^2 = 1 + (4.3Y^2 - 1) \left[ \text{Co} (x^{0.875}) (1-x)^{0.875} + x^{1.75} \right] \quad [20.7.28]$$

The Confinement number  $\text{Co}$ , given by Kew and Cornwell (1997), and the parameter  $Y$  are:

$$\text{Co} = \left( \frac{\sigma}{g(\rho_L - \rho_G) d_i^2} \right)^{1/2} \quad [20.7.29]$$

$$Y^2 = \frac{(dp/dz)_G}{(dp/dz)_L} \quad [20.7.30]$$

The Chisholm/Lockhart-Martinelli methods above are used to obtain the vapor and liquid pressure gradients. The experimental pressure drop data were obtained for R-134a, R-12 and R-113 during evaporation tests at saturation pressures from 1.38 to 8.56 bar, two sizes of circular tubes (2.46 and 2.92 mm) and one rectangular channel (4.06 x 1.7 mm).

Zhang and Webb (2001) measured adiabatic two-phase pressure drops for R-134a, R-22 and R-404A in one multi-port aluminum tube with channels of a hydraulic diameter of 2.13 mm and also in two small



diameter tubes of 3.25 and 6.25 mm. Thus, the database of this method tends to fall in between macrochannels and microchannels. They proposed the following reduced pressure two-phase multiplier correlation:

$$\Phi^2 = (1 - x)^2 + 2.87 x^2 \left( \frac{p_{\text{sat}}}{p_{\text{crit}}} \right)^{-1} + 1.68 x^{0.8} (1 - x)^{0.25} \left( \frac{p_{\text{sat}}}{p_{\text{crit}}} \right)^{-1.64} \quad [20.7.31]$$

Summarizing, from an overall point of view, none of the present separated flow methods seems to be able to be classified as a general design method since even the better ones are only able to capture about one-half the data consistently to within  $\pm 30\%$ . Based on comparisons of these methods to the multi-study database put together by Revellin, Wojtan and Thome (2006), the microscale method of Mishima and Hibiki (1996) appears to be the best of these separated flow models. In contrast, in a comparison by Revellin and Thome (2007b), the Zhang and Webb (2001) microscale method came in first and all the others performed poorly. Once again, the *macroscale* method of Müller-Steinhagen and Heck (1986) gave the best results. For a description of their method, refer to Chapter 13 in this book.

### 20.7.3 Theoretically Based Flow Models Applied to Microchannels

Apparently there is only one microchannel two-phase pressure drop model currently available that attempts to model the physics of the flow. Garimella, Killion and Coleman (2002) have proposed such a model for slug (elongated bubble or intermittent) flows, based on the work with air-water and condensation of refrigerants. Basically, they divided the flow into two zones, one for the elongated bubbles and one for the liquid slugs, similar to the microchannel elongated bubble flow boiling model of Jacobi and Thome (2002) described above. They then developed frictional pressure gradient expressions for the two types of flow and methods to predict the relative fraction of time and length that each occupied in a cycle, thus coming up with a frictional pressure drop model based on the frequency of the bubbles. Readers are referred to their paper for complete details. While their method worked well for their own database, Revellin and Thome (2007b) found that this method only predicted about 20% of their database to within  $\pm 20\%$  for R-134a and R-245fa in 0.5 and 0.8 mm channels. On the other hand, their model should only specifically be applied to slug flow data and such methods will become more useful as two-phase flow pattern maps for microchannels become more accurate and reliable, thus making possible comprehensive flow regime based methods.